

Electromagnetic properties of single-walled carbon nanotubes investigated by microwave absorption

Vom Fachbereich Chemie
der Technischen Universität Darmstadt

zur Erlangung des akademischen Grades eines

Doktor-Ingenieurs (Dr.-Ing.)

genehmigte

Dissertation

vorgelegt von

Dipl.-Ing. Björn Corzilius

aus Dieburg

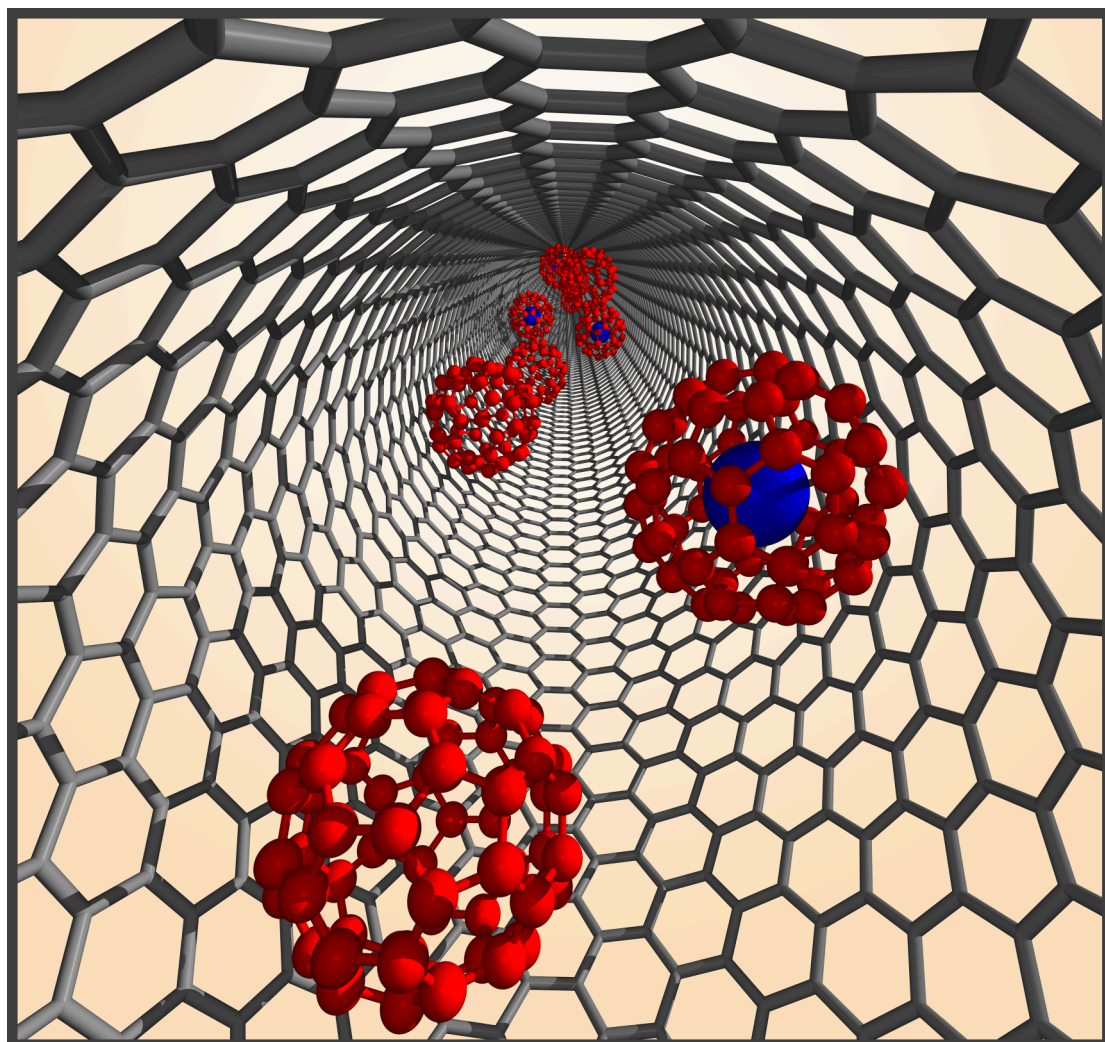
Referent:	Prof. Dr. rer. nat. Klaus-Peter Dinse
Korreferenten:	Prof. Dr. rer. nat. Michael Reggelin Prof. Dr. rer. nat. Michael Mehring
Tag der Einreichung:	17. April 2008
Tag der mündlichen Prüfung:	23. Juni 2008

Darmstadt 2008

D 17

Björn Corzilius

**ELECTROMAGNETIC PROPERTIES OF
SINGLE-WALLED CARBON NANOTUBES
INVESTIGATED BY
MICROWAVE ABSORPTION**



Darmstadt, 2008

Cover image:

Spin active N@C₆₀ in a carbon nanotube

Image reproduced by permission

of Professor K.-P. Dinse et al

and the PCCP Owner Societies

from B. Corzilius, K.-P. Dinse and K. Hata,

Phys. Chem. Chem. Phys., 2007, **9**, 6063, DOI: 10.1039/b707936m

This study is a result of the work carried out from March 2005 to April 2008 at the Eduard-Zintl-Institut für Anorganische und Physikalische Chemie, Technische Universität Darmstadt, under the supervision of Prof. Dr. Klaus-Peter Dinse.

Dedicated to my parents

In loving memory of Kai

*“ Whence come I and wither go I?
That is the great unfathomable question,
the same for every one of us.
Science has no answer to it. ”*

Max Planck, 1858–1947

Acknowledgments

In this section I would like to acknowledge all the people who contributed to this work.

My special thanks go to my supervisor *Prof. Dr. Klaus-Peter Dinse* for his unlimited support throughout my scientific career. I appreciate the countless discussions on a very high level and the inspirations I got therein. I am deeply grateful for the trust and confidence I was shown.

I thank *Prof. Dr. Michael Reggelin* and *Prof. Dr. Michael Mehring* for agreeing to act as reviewers of this thesis.

I greatly thank *Dr. Kenji Hata* for the gracious supply of many superb samples of single-walled carbon nanotubes. Without his outstanding achievement in the “Super-Growth” technique, this work would not have been possible.

Many thanks belong to *Dr. habil. Joris van Slageren* for performing the magnetization measurements at the University of Stuttgart.

I would like to thank *Dr. habil. Michael Böhm* for many helpful discussions and for proof-reading of the manuscript.

I thank *Dr.-Ing. Peter Jakes* for hundreds of fruitful discussions, especially about fullerenes, nanotubes, EPR, but also about non-science-related topics. I will never forget our trip to Berlin-Kreuzberg, the visit to “Zum Elefanten”, and all the way back to the “Harnack-Haus”.

I greatly appreciate the help of *Dr. Norbert Weiden* in apparative and scientific problems.

I also thank *Viktor Tissen* for all practical help.

I would like to thank my former colleagues *Dr.-Ing. Elvir Ramić*, *Dr. habil. Rüdiger-A. Eichel*, *Dr. Hrvoje Meštrić*, and *Dr. Emre Erdem* for many helpful discussions. My special thanks go to *Dr.-Ing. Armin Gembus* for the introduction to EPR.

ACKNOWLEDGMENTS

I also appreciate the contributions of master student *M. Tech. Suman Agarwal* and undergraduate student *Markus Müller*.

My special thanks go to *Miriam Hauf* for help in various bibliographic needs and for inspiring discussions about music.

I appreciate the help of *Dipl.-Geol. Ursula Henkes* in all administrative matters.

Funding and financial contributions to this work, especially from the Land Hessen, Technische Universität Darmstadt, and from the Deutsche Forschungsgemeinschaft, are gratefully acknowledged.

Further I would like to thank my parents *Birgitt* and *Helmut E. Corzilius* for their full support during my studies.

Special acknowledgment belongs to my girlfriend *Christiane Busse* for the understanding and patience for my work. Thanks for giving me the required time and for being there when I needed you.

Many thanks belong to my best friends *Dipl.-Wirtsch.-Ing. Alexander A. Kunz*, *Andreas R. Schmid*, and *Volker Krause*. Our meetings always reminded me that there is a world outside of science. When this work is finished, I will buy a beer (or two)!

I thank *Dipl.-Ing. Anna Karina Möller* and *Dipl.-Ing. Jeannine Heller* for a nice time during the whole studies. I appreciate our learning sessions and the discussions during lunch.

Last but not least I would like to thank all people, who contributed to this study but have not been mentioned by name.

Björn Corzilius

Darmstadt, April 2008

Abstract

Due to their unique properties, single-walled carbon nanotubes (SWNT) are very interesting candidates for the development of new electronic devices. Some of these properties, *e. g.*, a possible transition to a superconducting phase or the existence of ordered magnetic states, are still under investigation and intensively discussed.

Macroscopic amounts of SWNT can hitherto only be obtained as mixtures of tubes of different electronic properties. Therefore researchers have always been interested in a simple, fast, and reliable screening method to detect the signatures of metallic or semiconducting SWNT. It is assumed quite generally that these “standard” electronic properties can be identified rather easily. In contrast to this, the above mentioned “unconventional” properties, *i. e.*, superconductivity and magnetism, are anticipated to arise only in a small fraction of the nanotubes. Furthermore these features might be influenced by impurities, topological defects, or intertube interactions. Due to this fact, the sought-after screening method should be able to resolve the correlated signatures selectively, even if they are masked by other constituents in the sample.

This study invokes microwave absorption, both in its resonant (electron paramagnetic resonance) and in its non-resonant variant (cavity perturbation). This method represents a versatile and selective tool to characterize magnetic and electronic phases and occurrent transitions. Whereas metallic SWNT are intrinsically paramagnetic due to Pauli paramagnetism, ideal semiconducting tubes are diamagnetic and therefore not accessible to electron paramagnetic resonance (EPR). Nevertheless extrinsic and intrinsic temperature-activated defects can introduce paramagnetic states observable by EPR. In additional experiments, nitrogen encapsulated in C₆₀ has been incorporated inside SWNT as a paramagnetic probe, forming so called peapods. The synthesis of these N@C₆₀ peapods allows the examination of the electromagnetic properties of the SWNT “from the inside” by EPR.

In early studies, the EPR signal of SWNT grown by the electric arc-discharge method was masked by spurious signals of the catalyst remaining in the sample. By using nano-

tubes grown by a special chemical vapor deposition (CVD) technique, samples could be investigated which were almost catalyst-free. Thus it was possible to study the electronic properties of different types of SWNT over a wide temperature range by EPR. The high-temperature signals are dominated by itinerant spins. They result from the temperature activated delocalization of shallow defect states. At low temperatures, these charge carriers get trapped at specific sites. This trapping leads to a strong magnetic resonance of localized electron spins. Furthermore, no indication of the existence of elements different than carbon can be detected in the sample. This was proven by continuous wave (c. w.) EPR and also by modern techniques of pulsed EPR.

Non-resonant microwave absorption is introduced as a powerful tool to study the electronic conductivity of bulk samples of SWNT. A custom microwave bridge was constructed therefore. By evoking this method, the temperature dependence of the complex resistivity at $T > 20$ K could be attributed to the existence of pseudo-metallic or small-band-gap semiconducting tubes. At $T \approx 12$ K the transition from a non-linear dissipative state at low temperature to a conventional Ohmic loss behavior is observed. This transition is taken as an indication for the formation of superconducting domains in small parts of the sample. Furthermore, the existence of a weak ferromagnetic signal is detected *via* alternating current (AC) magnetization measurements. The features of this ferromagnetism, *i. e.*, weak magnetization, low saturation field, and the absence of hysteresis effects, exclude remaining iron catalyst as source of this observation. Instead, the cooperative magnetism might arise from an intrinsic exchange interaction in SWNT.

Zusammenfassung

Dank ihrer einzigartigen Eigenschaften sind einwandige Kohlenstoffnanoröhren (SWNT) sehr interessante Kandidaten für die Anwendung in neuartiger Elektronik. Einige dieser Eigenschaften werden von der wissenschaftlichen Gemeinschaft noch immer untersucht und diskutiert, wie z. B. ein möglicher Übergang in eine supraleitende Phase oder das Auftreten geordneter magnetischer Zustände.

Makroskopische Mengen an SWNT sind bis heute ausschließlich als Gemisch von Röhren unterschiedlicher elektronischer Eigenschaften erhältlich. Aus diesem Grund sind Wissenschaftler an einer einfachen, schnellen und zuverlässigen Methode interessiert, um die Proben auf Merkmale von metallischen oder halbleitenden Nanoröhren zu testen. Während diese „Standard-Merkmale“ vergleichsweise einfach zu identifizieren sein sollten, ist es wahrscheinlich, dass die „unkonventionellen“ Eigenschaften, d. h. Supraleitung und Magnetismus, nur in einem sehr kleinen Anteil der Nanoröhren auftreten. Weiterhin könnten diese Zustände durch Verunreinigungen, topologische Defekte oder Wechselwirkungen zwischen den Röhren beeinflusst werden. Von daher sollte die gesuchte Testmethode in der Lage sein, die jeweiligen Signaturen gezielt zu erkennen, auch wenn sie von anderen Bestandteilen der Probe überdeckt werden.

In dieser Arbeit wird Mikrowellenabsorption, sowohl in der resonanten (Elektronen Paramagnetische Resonanz) als auch in der nicht-resonanten Variante (Störung einer resonanten Mikrowellenkavität), angewendet. Diese Technik stellt eine vielseitige und selektive Methode zur Identifikation von magnetischen und elektronischen Phasen sowie der auftretenden Phasenübergänge dar. Während metallische SWNT durch Pauli-Paramagnetismus intrinsisch paramagnetisch sind, sind ideal halbleitende Röhren diamagnetisch und dadurch unzugänglich für Elektronen Paramagnetische Resonanz (EPR). Extrinsische Defekte und temperaturaktivierte intrinsische Defekte können jedoch EPR-aktive paramagnetische Zustände erzeugen. In weiteren Experimenten wurde Stickstoff-dotiertes C_{60} als paramagnetische Sonde in das Innere der SWNT eingeführt. Dabei ent-

stehen so genannte „Peapods“. Die Synthese dieser $N@C_{60}$ -Peapods erlaubt die Untersuchung der elektronischen Eigenschaften der SWNT durch EPR „von innen“.

In früheren Arbeiten war das EPR-Signal von SWNT, welche durch elektrische Lichtbogenentladung hergestellt wurden, vom störenden Signal des verbleibenden Katalysators überdeckt. Durch die Verwendung von speziellen Nanoröhren, die durch chemische Gasphasenabscheidung (CVD) hergestellt wurden, konnten praktisch katalysatorfreie Proben untersucht werden. Dadurch war ein direkter Zugriff auf die elektronischen Eigenschaften von SWNT über einen breiten Temperaturbereich möglich. Der Hochtemperaturbereich ist hauptsächlich durch bewegliche Spins bestimmt, die von der temperaturaktivierten Delokalisation von Defekten stammen. Bei tiefen Temperaturen frieren die Ladungsträger an bestimmten Positionen aus und führen zu starker magnetischer Resonanz von lokalisierten Spins. Weiterhin konnte kein Hinweis auf andere Elemente als Kohlenstoff gefunden werden. Dies wurde durch continuous-wave (c. w.) EPR und moderne Methoden der gepulsten EPR bewiesen.

Nicht-resonante Mikrowellenabsorption wird als leistungsfähige Methode zur Untersuchung der elektronischen Leitfähigkeit von SWNT vorgestellt. Zu diesem Zweck wurde eine Mikrowellenbrücke speziell angefertigt. Mit deren Hilfe konnte die Temperaturabhängigkeit der komplexen Leitfähigkeit bei $T > 20$ K der Anwesenheit von pseudometallischen oder halbleitenden Nanoröhren mit sehr kleiner Bandlücke zugeordnet werden. Bei tieferen Temperaturen wird ein Übergang von einem nicht-linear dissipativen Zustand ($T < 12$ K) zu normalem Ohmschen Verlust ($T > 12$ K) beobachtet. Dieser Übergang wird als Hinweis zur Ausbildung von supraleitenden Domänen in kleinen Teilen der Probe gedeutet. Des Weiteren wurde die Existenz eines schwachen ferromagnetischen Signals mit Wechselstrommagnetisierung nachgewiesen. Die Eigenschaften dieses Ferromagnetismus, d. h. schwache Magnetisierung, niedriges Sättigungsfeld und die Abwesenheit von Hystereseeffekten, schließen den Katalysator Eisen als Quelle dieses Effektes aus. Stattdessen könnte der kooperative Magnetismus durch intrinsische Austauschwechselwirkung in SWNT entstehen.

Contents

1	Introduction	1
1.1	Approaching the “Nanoworld”	1
1.2	Modifications of carbon	2
1.2.1	Graphite	3
1.2.2	Diamond	3
1.2.3	Fullerenes	4
1.2.4	Endohedral fullerenes	5
1.2.5	Carbon nanotubes	6
1.3	Theory of microwave absorption	12
1.3.1	Samples inside a resonant microwave cavity	12
1.3.2	Non-resonant microwave absorption	19
1.3.3	Electron paramagnetic resonance	23
1.3.4	Magnetization	28
1.4	Motivation	29
2	Experimental part	35
2.1	Sample synthesis and preparation	35
2.1.1	Nanotubes	35
2.1.2	Endohedral fullerenes	36
2.1.3	Fullerene peapods	36
2.2	Instrumentation	37
2.2.1	EPR	37
2.2.2	Non-resonant microwave absorption	38
2.2.3	Magnetization	39
3	Results and discussion	41
3.1	c. w. EPR	41
3.1.1	Spectral analysis	41
3.1.2	Deconvolution of signal A	43
3.1.3	Sensitivity to molecular oxygen	47
3.1.4	Temperature variation	49
3.2	Pulsed EPR	59
3.2.1	Spin echo at $T = 10$ K	59
3.2.2	Echo modulation experiments	63
3.2.3	Transient nutation experiments	67

CONTENTS

3.3	Spin-doping using endohedral fullerene peapods	69
3.4	Non-resonant microwave absorption	72
3.4.1	High-temperature dissipation ($T > 15$ K)	72
3.4.2	Low-temperature dissipation ($T < 15$ K)	76
3.4.3	Microwave dispersion	86
3.5	Magnetization	91
3.5.1	DC magnetization at high fields	91
3.5.2	AC magnetization at low fields	93
4	Summary and conclusion	101
	Appendix	105
	References	107
	List of symbols and abbreviations	117
	Curriculum vitae	125
	List of publications	127

1 Introduction

Contents

1.1	Approaching the “Nanoworld”	1
1.2	Modifications of carbon	2
1.2.1	Graphite	3
1.2.2	Diamond	3
1.2.3	Fullerenes	4
1.2.4	Endohedral fullerenes	5
1.2.5	Carbon nanotubes	6
1.3	Theory of microwave absorption	12
1.3.1	Samples inside a resonant microwave cavity	12
1.3.2	Non-resonant microwave absorption	19
1.3.3	Electron paramagnetic resonance	23
1.3.4	Magnetization	28
1.4	Motivation	29

1.1 Approaching the “Nanoworld”

Today, even in common language, the prefix “nano” is used frequently. Almost everyone has heard of “nanotechnology” or “nanosciences”; “nanorobots” or – as they are sometimes called – “nanobots” often play an important role in science-fiction literature or movies. Other products “containing nanotechnology” are for instance car finish protection or sun lotion. With the widespread “iPod nano”¹, even Apple has introduced “nano” to the music community. Many people, however, are not familiar with the precise meaning of “nano”; and many products related to nanotechnology actually have nothing to do with it. On the other hand, as the long-term impact of nanoparticles on the human

¹Copyrighted symbols and (registered) trademarks are not labeled throughout this work. The fact that a trademark is not labeled does not imply that it is not protected.

health and on the environment is still being discussed controversially, there exists a mixed attitude with respect to nanotechnology.

“Nano” has its etymological roots in the Greek language and is derived from the word “nanos”, meaning “dwarf”. So it is used as a metaphor for everything which is smaller in size than usual dimensions. It was introduced at the 11th Conférence Générale des Poids et Mesures (CGPM) in 1960 as SI prefix for a billionth (10^{-9}) of a quantity, indicating very small dimensions in space (nanometer, nm, 10^{-9} m), time (nanosecond, ns, 10^{-9} s), and other quantities.

Nanotechnology is often considered as being a new topic of science. However, it is rather a multidisciplinary field including various conventional topics like chemistry, applied physics, material sciences, and also mechanical or electrical engineering. In a quite common definition, nanotechnology is related to the manipulation of matter on the atomic or molecular scale, *i. e.*, in the nanometer scale. These manipulations can be due to self organization of the material or due to extrinsic forces. The properties of these new nanoscale materials depend highly on the particles’ size. Often they differ considerably from the conventional macroscopic material property. Hence, traditional chemistry – which also manipulates molecules on the atomic scale – is not considered as nanotechnology.

1.2 Modifications of carbon

Though carbon is not the most abundant element in the universe, it is one of the most versatile. This versatility is due to some unique chemical properties. Carbon atoms show a high affinity to form covalent bonds to various elements including to other carbon atoms. As a result of their four valence electrons, carbon atoms can be sp^3 -, sp^2 - and sp -hybridized, thus forming tetragonal, trigonal and linear topological arrangements. These peculiarities allow for a very huge variety in carbon chemistry.

But even when considering only elemental compounds, carbon can exist in different structures, so called allotropes. Until the mid 1980s, pure carbon was known to exist only in two elemental modifications: graphite and diamond. Graphite is the stable modification at ambient conditions, whereas diamond is stable under high pressure. The Gibb’s free enthalpy difference for the conversion from graphite to diamond amounts to $\Delta_r G^\circ = 2.90 \text{ kJ mol}^{-1}$ under standard conditions [1]. Anyhow, as the conversion rate between diamond and graphite at room temperature is negligible, once diamond is formed

from carbon, it is practically stable even under normal conditions. Although both materials contain only carbon atoms, they differ entirely in their properties.

1.2.1 Graphite

In graphite, all carbon atoms are sp^2 -hybridized and form hexagonal layers of honeycomb structure with bond lengths of $d_{C-C}^{(intra)} = 142$ pm [2]. The p -orbitals containing the fourth valence electron, which is not being involved in σ -bonding, form π -orbitals with electrons delocalized over the whole layer surface. Adjacent layers are bound *via* van der Waals interaction with an interlayer distance of $d_{C-C}^{(inter)} = 335$ pm [2]. Stacking occurs usually in ABAB order, with half of the carbon atoms being located on top of the center of one hexagon in the next layer. This stacking lowers the sixfold symmetry of the honeycomb lattice to threefold, which has severe effects on the electronic properties. Due to the layered structure, the mechanical and electronic properties exhibit a large anisotropy. Hence, graphite shows metallic conductivity parallel to the layers, being responsible for the black color and metallic glance. Semiconducting properties occur simultaneously in perpendicular direction. The mechanical anisotropy is a consequence of the relatively low binding energy between the layers and results in a rather easy shearing of graphite particles along the layer plane. This leads to low friction properties, which allow for the application of graphite as a non-abrasive lubricant.

Recently graphite mono-layers, *i. e.*, so-called graphene, could be isolated [3]. In this material without interlayer interaction the valence- and conduction bands touch at each of the six K-points in the hexagonal first Brillouin zone (see figure 1.1) in a linear dispersion relation². Due to this linear energy dispersion, relativistic massless Dirac fermions act as charge carriers. This unique situation leads to very peculiar charge transport properties [4].

1.2.2 Diamond

In diamond, all carbon atoms are sp^3 -hybridized and fourfold coordinated with other carbons in a cubic lattice. This three-dimensional network of tetrahedrally connected σ -bonds of 154 pm length [2] causes an outstanding hardness and very high thermal conductivity. The latter can be even enhanced when the natural amount of ^{13}C phonon

²Anyhow, due to relativistic effects, the hexagonal lattice splits into two trigonal sublattices. This introduces the property of a pseudospin to the charge carriers, leading to chiral charge carriers.

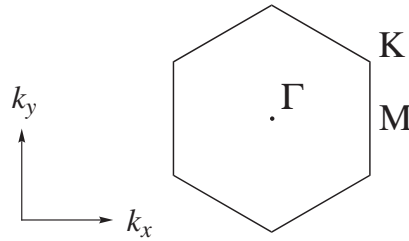


Figure 1.1: First Brillouin zone of the graphene honeycomb lattice. At the six corners of the hexagon, *i. e.*, the K-points, the valence and conduction band touch in a linear dispersion relation near the Fermi edge.

scattering centers is reduced in artificial diamond. The electrical conductivity of diamond is on the other hand very low, making it a good insulator. Furthermore this guarantees a high transparency over the whole visible spectral range.

1.2.3 Fullerenes

In 1985 Kroto *et al.* accidentally discovered a molecular class of elemental carbon, *i. e.*, fullerenes, with the most common representative being the buckminsterfullerene C_{60} [5]. For this observation, Sir Harold F. Kroto, Robert F. Curl Jr., and Richard E. Smalley were awarded the Nobel Prize in Chemistry 1996. Fullerenes in general are more or less spherical molecules consisting of sp^2 -hybridized carbon atoms arranged in five- or six-membered rings. In order to close the three-dimensional structure, each fullerene contains exactly twelve pentagons. In stable fullerenes, pentagons are separated by hexagons in such way that two pentagons never share one common edge. This rule is known as the “isolated pentagon rule”. Thus, C_{60} is the smallest possible fullerene containing 20 hexagons and has also proven to be the most stable. C_{60} exhibits a very high icosahedral symmetry (I_h) with a diameter of 0.7 nm.

Up to 1990, C_{60} could only be detected in traces in the helium exhaust gas during pulsed laser vaporization of a graphite target. Large quantities have been accessible, as Wolfgang Krätschmer, Konstantinos Fostiropoulos, and Donald R. Huffman developed a simple method for the production of C_{60} by electric-arc discharge between two graphite rods [6, 7]. This opened new possibilities of research on that peculiar material. ^{13}C nuclear magnetic resonance (NMR) experiments revealed the identity of all 60 carbon atoms [8]. Nonetheless, electrons are distributed in two different C–C bonds, *i. e.*, 6:6-bonds between two hexagons and 6:5-bonds between a hexagon and a pentagon. Despite the full conjugation of the π -orbitals, the electronic system of C_{60} shows no aromatic-

ity. Electron rich 6:6-bonds possess a length of 140 pm, whereas 6:5-bonds own higher single-bond-character with a length of 146 pm [9]. Thus chemical modification occurs preferably at 6:6-bonds. The electronic structure allows C_{60} to accept up to six additional electrons, making it a versatile building block of charge-transfer-compounds. Upon light irradiation, it is also capable of charge separation. This allows potentially for a highly-demanded application in photoelectronics and photovoltaics.

1.2.4 Endohedral fullerenes

Together with their discovery of C_{60} and C_{70} , Kroto, Curl, and Smalley proposed the possibility to implant small particles like single La atoms into the endohedral cavity of fullerenes [5]. Already in the same year $La@C_{60}$ could be synthesized and detected, but has proven to be unstable [10]. In 1991 $La@C_{82}$ was produced as the first stable metallo-endofullerene [11]. In this compound, the metal atom is located at an off-center position, bound to the inner carbon wall by ionic forces due to the transfer of all three valence electrons from La to the fullerene cage [12]. In the following time endohedral fullerenes with neutral atoms have been discovered, too. In $He@C_{60}$, the He atom is positioned around the center of the inner cavity after incorporation from the helium atmosphere during arc-discharge [13]. Saunders *et al.* have shown that the helium atoms can escape the cage at elevated temperatures and that the underlying mechanism of the incorporation of noble gas atoms in fullerenes is reversible [14]. They also succeeded in the synthesis of noble gas atoms (He, Ne, Ar, Kr, and Xe) incorporated in C_{60} and C_{70} under high pressure [15].

A remarkable investigation of the Hahn-Meitner-Institute (Berlin) has been the implantation of nitrogen atoms inside C_{60} in 1996 [16]. The resulting compound is stable both as solid and in solution. The nitrogen was found to exist in the atomic ground state $^4S_{3/2}$, oscillating in a harmonic field around the fullerene's center [17]. This observation is rather unexpected, as ground state nitrogen atoms tend to be highly reactive. Later calculations revealed a highly repulsive potential between the carbon cage and the incorporated nitrogen. This is explained by a severe distortion of the fullerene π -orbitals due to surface curvature and leads to significant contraction of nitrogen p -type wave functions [18].

1.2.5 Carbon nanotubes

Discovery and production

In 1991, Sumio Iijima described the production of “Helical microtubules of graphitic carbon” [19]. In the following time these structures were commonly denoted as multi-walled carbon nanotubes (MWNT). Although Iijima is acknowledged for this discovery in almost the whole literature, carbon nanotubes have been produced apparently by Radushkevich and Lukyanovich in the former USSR 40 years before the Iijima paper [20]. Due to the poor resolution of the applied transmission electron microscopy (TEM), however, the acknowledgment of that paper was limited. Additionally the Cold War and Russian language further impeded any high impact of the publication in the Western scientific community. In the following decades, several other reports on graphitic filament growth have been published, but none succeeded to achieve the tremendous impact of the Iijima paper [21].

In connection with Iijima’s report in 1991, the existence of carbon nanotubes formed by a single sheet of rolled-up graphene has been proposed. This arrangement leads to single-walled carbon nanotubes, which were anticipated to show mechanical and electric properties of dimensions unknown hitherto [22]. Already in 1992 Saito *et al.* predicted the existence of two electronically different types of SWNT, *i. e.*, metallic and semiconducting ones [23, 24].

In 1993 the observation of single-walled carbon nanotubes in the soot of a graphite arc-discharge was reported simultaneously by Iijima and Ichihashi as well as by Bethune *et al.* [25, 26]. Both groups utilized ferromagnetic transition metals, *i. e.*, iron and cobalt, as catalyst during the growth process to produce SWNT with diameters of 1 to 2 nm. In the same year Saito *et al.* used nickel as catalyst for the SWNT production [27]. In their study, they were able to resolve the status of the remaining catalyst after SWNT production. It revealed to exist in the form of metallic nanoparticles of a few nm in size, being covered by multiple layers of turbostratic carbon. In the following years, several other SWNT growth methods have been developed, including laser ablation [28–30] and chemical vapor deposition (CVD) [31, 32]. The need of a magnetic catalyst is the common disadvantage of the methods mentioned. Even after purification, it remains in the sample in significant amount.

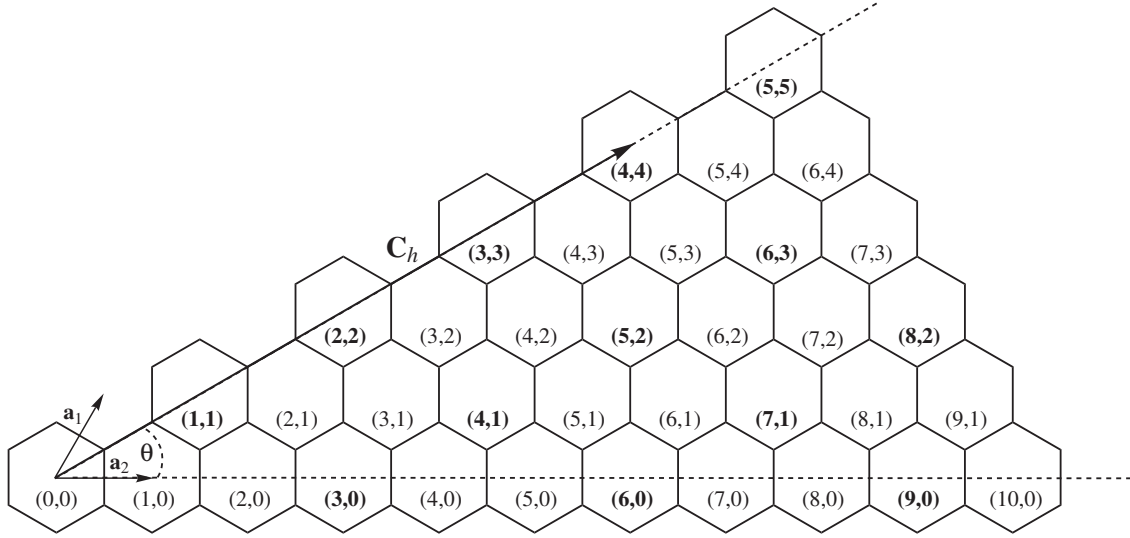


Figure 1.2: Generation of nanotubes by rolling up a sheet of graphene along the chiral vector \mathbf{C}_h , being defined by multiples of the hexagonal unit vectors \mathbf{a}_1 and \mathbf{a}_2 (shown only for right handed chirality with $m \geq n$). By bringing the hexagon of the origin $(0,0)$ into congruence with hexagon (m,n) (shown exemplarily for $(4,4)$) a nanotube with this chiral index (m,n) and chiral angle θ is formed. The translational vector (not shown) is orthogonal to \mathbf{C}_h . Indices printed in boldface lead to metallic tubes.

Structure

Carbon nanotubes can virtually be generated by rolling up a sheet of graphene. Because wrapping can be performed in various directions, *i. e.*, along the armchair direction, along the zigzag direction, and along every direction between these boundaries, an unlimited number of nanotubes of different structure can be formed. For an unambiguous identification of the structure, the chiral vector \mathbf{C}_h is introduced. It is formed by a linear combination of the hexagonal unit vectors \mathbf{a}_1 and \mathbf{a}_2 :

$$\mathbf{C}_h = m\mathbf{a}_1 + n\mathbf{a}_2. \quad (1.1)$$

n and m are combined to the so-called chiral index (n,m) . Although an infinite number of different tubes can be created, only integers are allowed for n and m and thus the possible chiral indices are quantized. If two graphene hexagons separated by \mathbf{C}_h are brought into

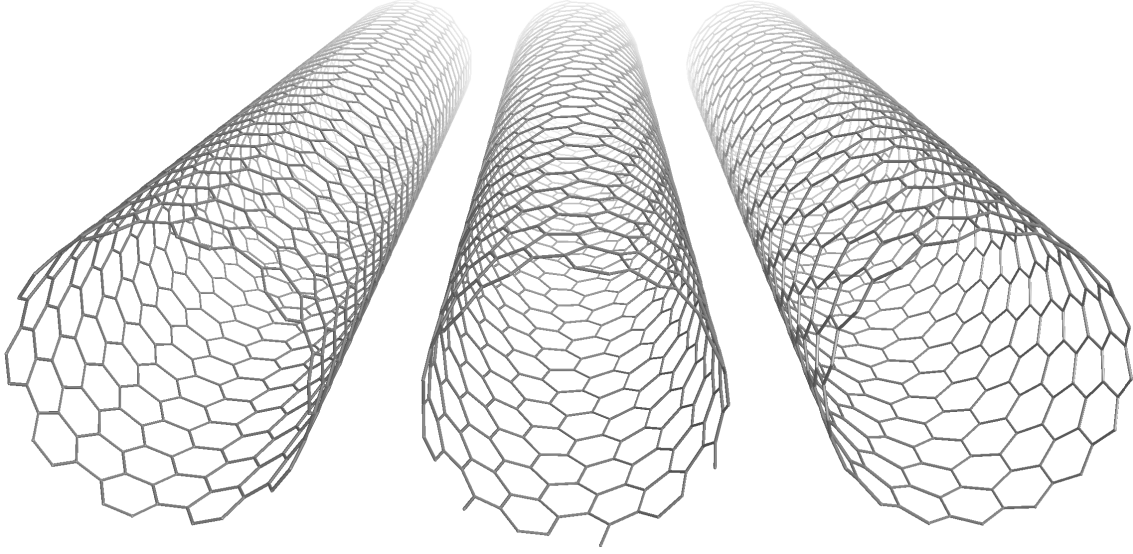


Figure 1.3: Nanotubes with several chiral vectors but similar diameter. *Left*: armchair tube (10,10), *middle*: chiral tube (13,6), *right*: zigzag tube (17,0). SWNT structures have been generated using the program TubeGen [33].

congruence by wrapping, a nanotube with diameter d is formed:

$$d = \frac{|\mathbf{C}_h|}{\pi} = \frac{a}{\pi} \sqrt{m^2 + mn + n^2}. \quad (1.2)$$

a denotes the magnitude of the unit vectors \mathbf{a}_i . For $d_{\text{C-C}} = 0.142$ nm (*i. e.*, the C–C bond length in graphite) it takes the value $a = \sqrt{3}d_{\text{C-C}} = 0.246$ nm.

In addition to the chiral vector, the chiral angle θ is defined to determine the chirality of the tube:

$$\theta = \arccos \frac{\mathbf{a}_1 \cdot \mathbf{C}_h}{a |\mathbf{C}_h|} = \arccos \frac{m + \frac{n}{2}}{\sqrt{m^2 + mn + n^2}}. \quad (1.3)$$

Based on this angle, topologically different types of nanotubes are defined. Zigzag nanotubes possess a chiral angle of $\theta = 0$, *i. e.*, they are formed by all nanotubes with $(m, 0)$. A chiral angle of $\theta = \frac{\pi}{6}$ leads to armchair nanotubes with chiral indices $m = n$, which is also expressed by (m, m) . All other tubes with $-\frac{\pi}{6} < \theta < \frac{\pi}{6}$ are chiral, with right handed helices for $\theta > 0$ and left handed helices for $\theta < 0$. Though zigzag tubes possess helical symmetry as well, they can be mapped into each other by a mirror transformation; thus they are not chiral. Armchair tubes do not show any helicity and therefore do not possess any chiral properties, too.

The nanotube generated will expand in the direction orthogonal to the chiral vector. This direction is defined by the translational vector \mathbf{T} :

$$\mathbf{T} = -\frac{m+2n}{D_{mn}R}\mathbf{a}_1 + \frac{2m+n}{D_{mn}R}\mathbf{a}_2, \quad (1.4)$$

where D_{mn} defines the largest common divisor of m and n . R can take the values 3 and 1, depending on the relation between m and n :

$$R = \begin{cases} 3 & \text{for } m \equiv n \pmod{3D_{mn}} \\ 1 & \text{for all other cases.} \end{cases} \quad (1.5)$$

The magnitude of \mathbf{T} represents the length of the unit cell of the nanotube in the tube direction:

$$t = |\mathbf{T}| = \frac{\sqrt{3(m^2 + mn + n^2)}}{D_{mn}R}. \quad (1.6)$$

The ends of the nanotubes have been shown to consist of half fullerene caps. Due to the very high aspect ratio of the tubes (typically in the range of 10^4 to 10^6) the influence of the capped ends on the mechanical or electronic properties of the tubes can in most cases be neglected. In contrast, the ends play an important role in nanotube growth. So in many cases the ends have been found to stick to catalyst particles. These particles with metallic and magnetic properties are assumed to have a more dramatic effect especially on the tube's electronic characteristics.

Furthermore, SWNT tend to form agglomerates of hexagonal structure, which are commonly referred to as ropes or bundles. Due to intertube interactions, these bundles can show properties differing significantly from the single tube's properties.

Electronic properties

To elucidate the electronic properties of SWNT, a description in reciprocal space is most appropriate. As an idealized sheet of graphene consists of an unbounded carbon honeycomb lattice of sixfold symmetry, the first Brillouin zone is represented by a hexagon around the Γ -point. For a simple depiction see figure 1.1 on page 4. The valence and the conduction band are supposed to touch in a linear dispersion relation at the K-points located at the six corners of the Brillouin zone. When the unbounded sheet of graphene

is rolled to an infinitely long nanotube, the boundary condition

$$M\lambda = |\mathbf{C}_h| = \pi d \quad (1.7)$$

with $M = \{-\frac{q}{2}, -\frac{q}{2} + 1, \dots, 0, \dots, \frac{q}{2}\}$ and q symbolizing the number of hexagons in the tube's unit cell, causes a quantization of the allowed wave vectors. This leads to standing waves of length λ around the tube's circumference. According to the chiral vector and the translational vector in real space, two vectors can be defined in k -space, *i. e.*, the wave vector \mathbf{k}_t along the tube axis and the wave vector \mathbf{k}_c along the tube circumference. Due to the infinite tube length, the former is continuous in the Brillouin zone, whereas the latter is being quantized within discrete values. The proper wave vectors can be obtained by orthogonality relations between vectors in real space and vectors in reciprocal space:

$$\mathbf{k}_c \cdot \mathbf{C}_h = 2\pi, \quad (1.8a)$$

$$\mathbf{k}_c \cdot \mathbf{T} = 0, \quad (1.8b)$$

$$\mathbf{k}_t \cdot \mathbf{C}_h = 0, \quad (1.8c)$$

$$\mathbf{k}_t \cdot \mathbf{T} = 2\pi. \quad (1.8d)$$

In the following the direction of the wave vectors is omitted for convenience. Only general formulae for the vectors' magnitudes are given.

Whereas the wave vector k_t along the tube axis is limited by the relation

$$-\frac{2\pi}{t} \leq k_t \leq \frac{2\pi}{t} \quad (1.9)$$

and is continuous for nanotube length $l \rightarrow \infty$, the wave vector k_c along the tube circumference is quantized to obey the constraint given in equation (1.7):

$$k_c = \frac{2\pi}{\lambda} = \frac{2M}{d}. \quad (1.10)$$

The resulting wave vector has $2M$ nodes along the circumference.

As a result of the above considerations, the wave vectors derived form $(q + 1)$ parallel lines of length $\frac{2\pi}{t}$ within the Brillouin zone. They are equally spaced by an amount of $\frac{2M}{d}$, while the orientation of the lines depends on the chiral angle θ . As the valence and the conduction band exclusively touch at the K-points, only SWNT with allowed k -states at the K-points can exhibit metallic conductivity. This condition is met for nanotubes with

$m \equiv n \pmod{3}$). Nanotubes not matching that condition are semiconductors with a band gap of around 0.3 to 1 eV. The value depends inversely on the tube's diameter [23, 24]. From a purely statistical analysis, one third of all possible chiral indices match the above condition and therefore lead to basically metallic nanotubes.

However, as the graphene curvature has not been taken into account for the relations derived above, the true metallicity holds only for armchair nanotubes with chiral indices (m, m) . In “pseudo-metallic” nanotubes, *i. e.*, for $m \equiv n \pmod{3}$ but $n \neq m$, the curvature induces a σ - π -interaction. This leads to the formation of a small electronic gap of ~ 0 to 50 meV, which scales as $\frac{1}{d^2}$ [34, 35]. The electronic structure of armchair tubes is not directly affected by curvature effects. However, once individual isolated nanotubes are brought to contact with each other or form bundles, the arising intertubular interaction as well as the lifting of the symmetry opens an energy gap at the Fermi level even for armchair nanotubes [36, 37].

Because metallic SWNT are an ideal model system of a quasi one-dimensional (1D) conductor, peculiar properties are anticipated which are absent in three-dimensional metals. One expected effect is the formation of a Tomonaga-Luttinger-Liquid (TLL) instead of a classical Fermi liquid. This peculiarity is induced by long-range Coulomb interactions and leads to an anomalous power-law dependence of the resistivity and power-law tunneling density of states [38, 39]. Furthermore, spin-charge separation is anticipated in that state [40]. Due to the very low efficiency of electron backscattering in the 1D system, the transport in individual nanotubes is ballistic [41, 42]. At very low temperatures, also weak localization effects can be observed [43]. Additionally, Kohn anomalies induced by electron-phonon coupling are anticipated, as well as Peierls distortions in the 1D system [44]. Due to the lifted degeneracy of left- and right-handed ring currents around the tube circumference, Aharonov-Bohm oscillations occur in an external magnetic field [45]. At very low temperatures, individual nanotubes can act as a quantum dot, giving rise to interesting phenomena, such as Coulomb blockade, Fabry-Pérot resonance, and Kondo effect [46].

Peapods

In 1997, Nikolaev *et al.* discussed the possibility to incorporate C_{60} inside a (10,10) nanotube [47]. Due to the perfect match of the radii of the van der Waals surfaces of C_{60} and the hollow core of the nanotube, this compound seemed to be energetically preferable. The structure was detected accidentally only one year later. Brian W. Smith,

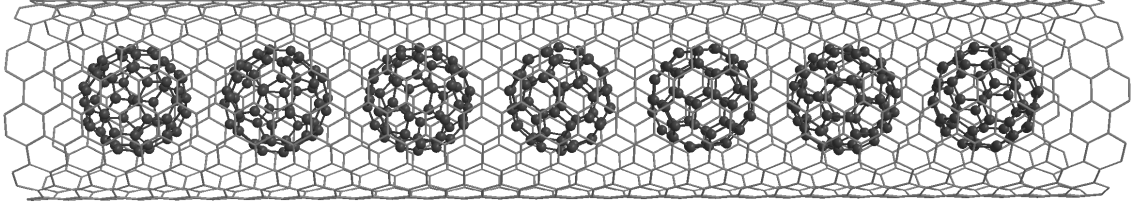


Figure 1.4: Peapod consisting of C_{60} molecules inside a (10,10) nanotube.

Marc Monthieux and David E. Luzzi discovered encapsulated C_{60} molecules in SWNT produced by pulsed laser vaporization of graphite [48]. Due to their morphological similarity, the corresponding structure was given the name “nanoscopic peapod”. Two years later, the same group presented a model for the formation mechanism of fullerene peapods together with a recipe to obtain fullerene-filled nanotubes in high yield [49]. In the following time, peapods of C_{70} and higher fullerenes as well as metallofullerenes have been produced and analyzed [50, 51]. Though encapsulated C_{60} have only a minor effect on the nanotube structure, the impact on the electronic properties are more striking [52].

1.3 Theory of microwave absorption

1.3.1 Samples inside a resonant microwave cavity

The resonant cavity

In a typical microwave absorption experiment, either based on electron paramagnetic resonance (EPR) or on non-resonant cavity perturbation, the sample is put inside a microwave cavity. The ratio of the microwave energy E_{stor} being stored and the energy E_{diss} being dissipated per cycle inside the cavity is defined as the cavity quality factor Q [53]:

$$Q = 2\pi \frac{E_{\text{stor}}}{E_{\text{diss}}}. \quad (1.11)$$

Another definition is based on an rf-tuned RLC circuit in series (see figure 1.5), which is a circuit analog of a microwave cavity:

$$Q = \frac{\omega_0 L}{R} = \frac{1}{R\omega_0 C}. \quad (1.12)$$

R , L , and C are the circuit’s resistance, inductance, and capacitance, respectively. ω_0

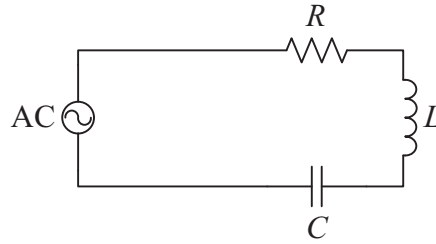


Figure 1.5: RLC tuned circuit in series as analog of a microwave cavity resonator.

denotes its angular frequency at resonance. Using this equation, the quality factor can be determined practically as the ratio of the resonance frequency of the cavity and the width of the resonance curve:

$$Q = \frac{\omega_0}{\Delta\omega}. \quad (1.13)$$

The half width $\frac{1}{2}\Delta\omega$ thereby indicates the value of $(\omega - \omega_0)$, where the dissipated power has fallen to one half of the value at resonance (for a clearer depiction see figure 1.7). In other words, $\Delta\omega$ denotes the full width at half maximum (FWHM) of the cavity resonance curve.

Coupling of the resonator

In a virtual cavity totally closed, a connection of the internal microwave field to the outside does not exist. Thus, the so-called unloaded quality factor Q_u only depends on Ohmic losses in the cavity walls³. Upon coupling of the resonator to a waveguide⁴, the internal microwave radiation can leave the cavity through the coupling unit, *e. g.*, the iris hole. This leads to additional losses and the introduction of the so-called radiation quality factor Q_r . Both entities add inversely to the loaded quality factor Q_l :

$$Q_l^{-1} = Q_u^{-1} + Q_r^{-1}. \quad (1.14)$$

The ratio between Q_u and Q_r is called the coupling parameter β :

$$\beta = \frac{Q_u}{Q_r}. \quad (1.15)$$

³Losses in dielectrics are omitted so far.

⁴All considerations refer to a cavity operating in reflective mode.

If the cavity is perfectly matched to the waveguide (which theoretically can be achieved by either adjusting Q_u or Q_r), β takes the value 1. In this case the cavity is called “critically coupled” and the voltage standing wave ratio (VSWR) is

$$\text{VSWR} = \beta = 1, \quad (1.16)$$

indicating that the cavity perfectly terminates the transmission line with its own impedance Z_0 . The result is a vanishing standing wave in the waveguide. For $\beta > 1$ the cavity is called “overcoupled” with $\text{VSWR} = \beta$, whereas in the opposite case ($\beta < 1$) the inverse $\text{VSWR} = \frac{1}{\beta}$ accounts for an “undercoupled” resonator.

In practice, coupling of the resonator is accomplished by a variation of Q_r via the coupling unit, *e. g.*, an iris screw in the case of an iris hole, and matching it to Q_u . The latter parameter is determined intrinsically by the cavity itself and the inserted sample. The case of critical coupling can be recognized by the absence of any standing wave in the transmission line, *i. e.*, when no microwave power is reflected from the cavity to the detector.

Filling factor and magnetic resonance condition

When a sample is inserted in a microwave cavity, it is sensing only a fraction of the total microwave field. The ratio between the effective microwave magnetic field at the sample’s volume V_s and the total microwave magnetic field inside the cavity of volume V_c is defined as the filling factor η :

$$\eta = \frac{\int_{V_s} |\mathbf{B}_{\text{rf}}|^2 dV}{\int_{V_c} |\mathbf{B}_{\text{rf}}|^2 dV} = \frac{V_s \langle B_{\text{rf}}^2 \rangle_s}{V_c \langle B_{\text{rf}}^2 \rangle_c}. \quad (1.17)$$

During magnetic resonance, the absorption of microwave power in a sample with the EPR susceptibility χ'' is proportional to $\chi''\eta$. This is expressed by an additional component Q_χ :

$$Q_\chi = \frac{1}{\chi''\eta}, \quad (1.18)$$

and leads to an effective Q reduction of the – initially – critically coupled cavity:

$$Q^{-1} = Q_u^{-1} + Q_\varepsilon^{-1} + Q_r^{-1} + Q_\chi^{-1}. \quad (1.19)$$

Q_ε^{-1} describes losses in dielectrics, which – so far – have been omitted for convenience. The subsequent change of the coupling parameter β upon Q reduction is responsible for the introduction of a VSWR $\neq 1$. The microwave power reflected thereupon can then be recorded easily by the detector unit.

The filling factor strongly depends on the electromagnetic properties of the inserted sample. As long as the sample dimension is negligible compared to the cavity volume, the microwave field distribution is not altered by the sample. Once, however, the sample takes a significant volume of the cavity, it severely affects the microwave field distribution both inside and outside of the sample volume. Thus the filling factor has to be regarded carefully when analyzing experimental EPR susceptibilities.

Conductive samples in a resonant microwave cavity

If a conductive sample is placed in a microwave cavity, the microwave field will induce oscillating ring currents (so-called eddy currents) which shield the sample's interior from the incident microwaves. By adopting a compact metal of macroscopic scale, the ring currents will be induced only at the metal surface. With increasing depth x from the surface, the effective microwave field amplitude B in that surface layer will drop exponentially with the characteristic dimension δ :

$$B(x) = B(x=0) \exp\left(-\frac{x}{\delta}\right). \quad (1.20)$$

The skin depth δ is a function of the conductivity σ and magnetic permeability μ of the material together with the incident microwave angular frequency ω :

$$\delta = \sqrt{\frac{2}{\sigma\mu\omega}}. \quad (1.21)$$

As the skin depth is directly related to the sample conductivity, a variation of the latter will also result in a change in cavity Q , cavity resonance frequency ω_0 , and filling factor η . The directions of the changes in Q and ω_0 , however, depend on the ratio between the skin depth δ and the sample thickness d . Peligrad *et al.* derived a Q and ω_0 shift for a

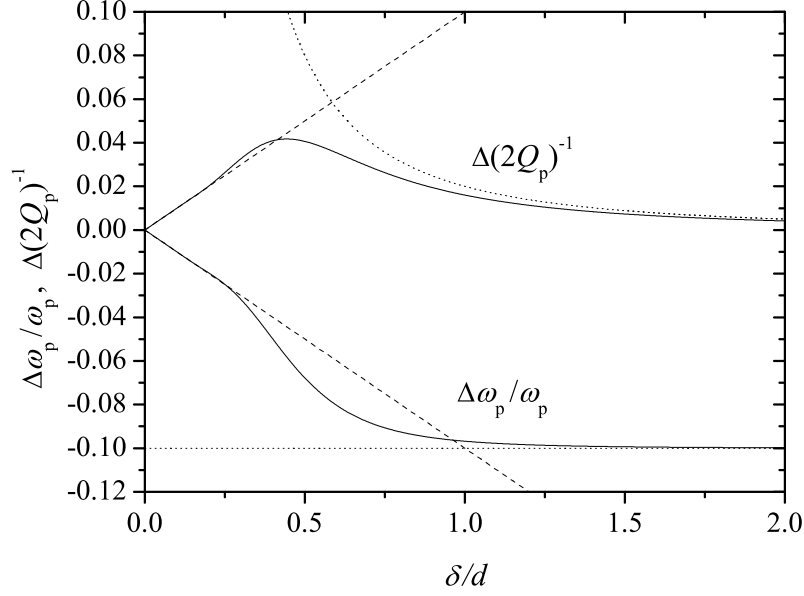


Figure 1.6: Dependence of the Q shift (upper traces) and frequency shift (lower traces) as a function of the skin depth δ of the sample according to equations (1.22) for a constant filling factor of $\eta = 0.1$. Dashed and dotted lines depict the linear behavior for electromagnetically thick samples as well as the asymptotic behavior for electromagnetically thin samples, respectively. Figure adapted from [54].

sample of slab geometry in the magnetic field maximum of a cavity operating in TE_{102} mode [54]:

$$\frac{\Delta\omega_p}{\omega_p} = -\eta \frac{\delta \sinh\left(\frac{d}{\delta}\right) + \sin\left(\frac{d}{\delta}\right)}{d \cosh\left(\frac{d}{\delta}\right) + \cos\left(\frac{d}{\delta}\right)} \quad (1.22a)$$

$$\Delta(2Q_p)^{-1} = \eta \frac{\delta \sinh\left(\frac{d}{\delta}\right) - \sin\left(\frac{d}{\delta}\right)}{d \cosh\left(\frac{d}{\delta}\right) + \cos\left(\frac{d}{\delta}\right)}. \quad (1.22b)$$

Index p denotes the difference between a perfect conductor, *i. e.*, $\delta = 0$, and the sample with finite conductivity as derived by perturbation theory. Equations (1.22) are depicted in figure 1.6. Although the equations have been derived for a specific sample geometry in a specific resonator mode, the general behavior is valid for all samples located in the magnetic field maximum of a cavity. The frequency and Q shifts are calculated for a constant filling factor. This assumption oversimplifies the model, as η itself is a function of the sample's conductivity in practice. Nevertheless, the above consideration is rather useful to understand the need to discriminate between two distinct cases at the extreme

limits, *i. e.*, the case of electromagnetically thick samples with $\delta \ll d$ and the case of electromagnetically thin samples with $\delta \gg d$. This situation is of decisive importance for the interpretation of experimental Q data. In the former case Q increases with increasing sample conductivity, in the latter this relation becomes inverse. This correlation might lack intuitive self-evidence but can be understood quite well by a simple description. When the initially highly conducting sample with $\delta \ll d$ becomes more and more resistive, the rf field can penetrate deeper into the material. Outcome of this behavior are higher Ohmic losses in the surface layer and thus a Q reduction. In the case of $\frac{\delta}{d} \approx 0.5$, the deviation between both electromagnetically thick and thin approximation is greatest. Because the skin depth of opposing sample surfaces meet at the center of the sample volume, the conduction losses are maximum. With a further δ increase, the overall rf field amplitude inside the sample volume grows due to an increasing overlapping of decay profiles from both sides of the sample. As the sample gets more and more transparent to microwaves, the Ohmic losses again decrease.

Dielectrics in the cavity

As soon as a sample with non-vanishing dielectric properties is introduced in the cavity, the microwave field distribution is altered as a function of the complex dielectric constant

$$\varepsilon = \varepsilon' - i\varepsilon'' \quad (1.23)$$

with i being the imaginary unit. The real part of ε , *i. e.*, ε' , represents the energy storage inside the sample, the imaginary component ε'' stands for the energy loss. The ratio $\frac{\varepsilon''}{\varepsilon'}$ is denoted as the dielectric loss tangent. In low-loss dielectrics, *i. e.*, when $\varepsilon'' \approx 0$, ε takes the real value ε' . In this case, the wavelength λ inside the dielectric is changed according to its dielectric constant

$$\frac{\lambda_s}{\lambda_c} = \sqrt{\frac{\varepsilon_s}{\varepsilon_c}}, \quad (1.24)$$

where the indices s and c refer to the sample and to the cavity's interior, respectively. For convenience, the cavity's inside volume is treated as vacuum in the following. This simplifies equation (1.24) to

$$\lambda_s = \lambda_c \sqrt{\varepsilon_s}. \quad (1.25)$$

The index s is omitted in the following. This shift in wavelength leads to a direct shift in the cavity's resonance frequency, while the rf field amplitude remains unaltered. According to the cavity perturbation method [55] the frequency shift can be expressed as

$$\frac{\omega_e - \omega_f}{\omega_f} = \frac{\Delta\omega}{\omega_f} = \frac{\eta_E}{2} (\epsilon' - 1). \quad (1.26)$$

The indices e and f denote the empty cavity and the cavity filled with the dielectric sample, respectively. It has to be noted that the electric filling factor

$$\eta_E = \frac{\int_{V_s} |\mathbf{E}_{\text{rf}}|^2 dV}{\int_{V_c} |\mathbf{E}_{\text{rf}}|^2 dV} = \frac{V_s \langle \mathbf{E}_{\text{rf}}^2 \rangle_s}{V_c \langle \mathbf{E}_{\text{rf}}^2 \rangle_c}. \quad (1.27)$$

has to be evoked, because the interaction between the microwave field and the dielectric is mediated by the electric field component. To avoid accidental misuse of the magnetic filling factor η introduced formerly, the electric filling factor is denoted as η_E . In magnetic resonance experiments the sample is normally placed in the magnetic field maximum of a microwave cavity. In most cases, this position corresponds to the electric field minimum represented by a nodal plane or axis. Due to finite sample dimensions, however, the electric filling factor is not zero though.

If the sample possesses a non-vanishing imaginary component of the dielectric constant, the microwave field experiences both a shift in wavelength and an attenuation due to the dielectric loss. The latter results in a decrease of Q :

$$Q_f^{-1} - Q_e^{-1} = \Delta Q^{-1} = \eta_E \epsilon''. \quad (1.28)$$

Both relations, *i. e.*, equations (1.26) and (1.28), only hold in first-order approximation. For higher orders, Q is also affected by ϵ' [56]:

$$\frac{\eta_E}{2} (\epsilon' - 1) = \frac{\Delta\omega}{\omega_f} + \frac{\Delta Q^{-1}}{4Q_f}. \quad (1.29)$$

This leads to an additional frequency shift caused by the dielectric loss, which is not related directly with ϵ' :

$$\left(\frac{\Delta\omega}{\omega_f} \right)_{\epsilon''} = \frac{\eta_E \epsilon''}{4Q_f}. \quad (1.30)$$

As neither η_E , ε'' nor Q_f can take negative values, it is obvious that the dielectric-loss always leads to a reduction in the cavity resonance frequency.

In practice, the dielectric loss cannot be distinguished experimentally from conduction loss [57]. Hence, both terms are often combined in the alternating current (AC) conductivity σ_{AC} [58]:

$$\sigma_{AC} = \sigma + \omega\varepsilon''\varepsilon_0, \quad (1.31)$$

where σ denotes the direct current (DC) conductivity and ε_0 is the electric permittivity of free space. Thus, an effective ε''_{eff} can be introduced, containing all influence parameters mentioned above:

$$\varepsilon''_{eff} = \frac{\sigma_{AC}}{\omega\varepsilon_0} = \varepsilon'' + \frac{\sigma}{\omega\varepsilon_0}. \quad (1.32)$$

This ε''_{eff} accounts for the total power loss in the sample, either induced by conduction loss, or by dielectric loss, or a combination of both.

1.3.2 Non-resonant microwave absorption

General

In the mid 20th century, microwave absorption was used to study surface impedance and related properties on type-I superconductors [59–64]. With the discovery of high- T_c superconductivity by Bednorz and Müller [65] in 1986, a new class of type-II superconductors led to a renaissance of this technique, because the strong dependence of microwave absorption on the magnetic field facilitated measurements using magnetic-field-modulation [66–71]. This strong magnetic-field dependence only exists in the superconducting phase [72]; hence an unambiguous identification of superconducting phases was possible, even if the overall sample mass was small or the superconducting phases were embedded in a normal state configuration [70]. Besides magnetic-field-modulated microwave absorption, direct microwave absorption was also evoked [73, 74]. This technique is performed generally *via* the cavity perturbation method. As it also senses microwave dissipation mechanisms which do not depend on the magnetic field, it is less selective than its modulated variant. This can be the case for metal-insulator transitions, for instance.

In order to unambiguously identify the onset of superconductivity by measurements of the DC conductivity, compact samples are required. The great advantage of microwave absorption lies in the high sensitivity. So even small amounts of superconducting material embedded in an insulating or conventionally conducting host material can be identified [70, 75]. Additionally, an electrical connection to the sample is not necessary. Thus there is no influence by contact resistance or proximity effect. Furthermore even very sparse samples can be investigated without need to compact the sample mechanically.

Microwave resonance in a cavity

As the theoretical description of a microwave cavity has already been given in the preceding section 1.3.1, this section will focus on practical aspects of microwave resonance. As the build-up of a standing wave in the microwave cavity is a typical resonance phenomenon, all standard relations also hold in this case. For instance, the stored microwave power P in the critically coupled cavity as a function of the incident frequency ω follows a typical Lorentz resonance line:

$$P(\omega) = P_0 \frac{\left(\frac{\Delta\omega}{2}\right)^2}{(\omega - \omega_0)^2 + \left(\frac{\Delta\omega}{2}\right)^2}, \quad (1.33)$$

where ω_0 is the resonance frequency and $\Delta\omega$ is the full width between the two frequency values, at which P takes one half of its maximum value, *i. e.*, it describes the FWHM value. Thus it is also often denoted as the 3 dB width. Using equation (1.13), the stored power can be expressed directly as a function of the parameter Q :

$$P(\omega) = P_0 \frac{\left(\frac{\omega}{2Q}\right)^2}{(\omega - \omega_0)^2 + \left(\frac{\omega}{2Q}\right)^2}. \quad (1.34)$$

As derived in section 1.3.1, the elucidation of Q can yield direct information on the effective dielectric loss due to ϵ''_{eff} . For convenience, all sample related loss is combined in the following in Q_s^{-1} , which together with the intrinsic loss Q_e^{-1} of the empty cavity results in the total loss Q_f^{-1} of the cavity filled with the sample:

$$Q_f^{-1} = Q_e^{-1} + Q_s^{-1} \quad (1.35)$$

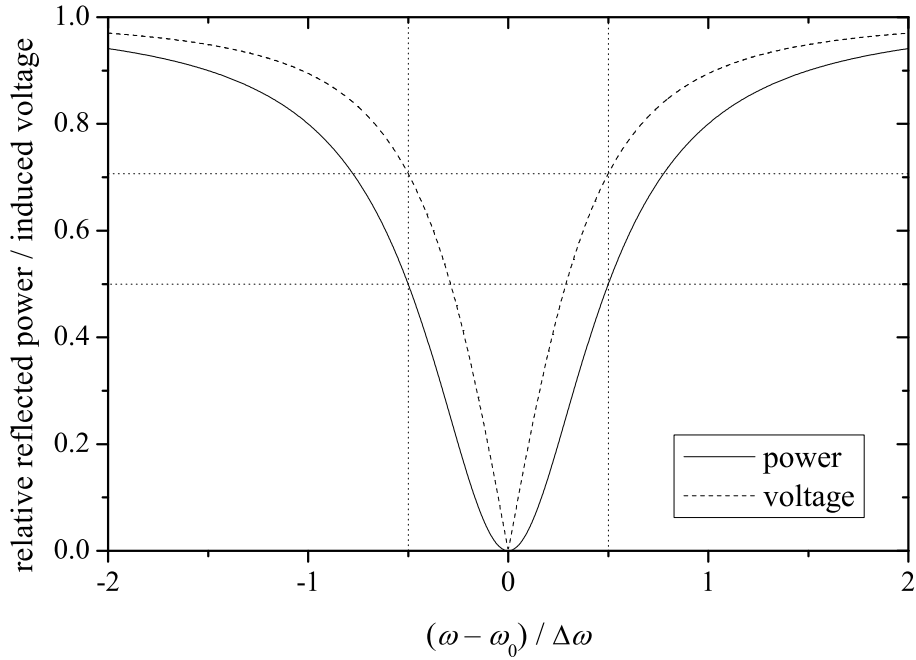


Figure 1.7: Reflected power (solid line) and detector voltage (dashed line) of a resonant cavity as a function of the incident microwave frequency. Power and voltage are given relative to full reflection. Dotted lines denote the frequencies at which the reflected power or the induced voltage amount to $\frac{1}{2}$ or $\frac{1}{\sqrt{2}}$ times the values off resonance, respectively. Q can be determined from the difference between these frequencies.

For high- Q -cavities or – more generally – for $Q_e \gg Q_s$, the sample related loss is dominating and $Q_s \approx Q_f$ is valid in good approximation.

In practice, there exist numerous methods to determine Q [76]. The most simple one which allows the reading of Q with a simple setup, requires a microwave ramp generator, a crystal detector, and an oscilloscope. It generates a rapidly swept frequency ramp. The reflected microwave power induces a current in the crystal diode which is then displayed as voltage equivalent on the scope screen. For the critically coupled resonator the reflected power is zero at resonance frequency ω_0 . It takes the value of the incident power P_0 for a frequency differing substantially from the resonance frequency. As the detector line is typically terminated by a 50Ω resistance, the obtained signal is proportional to the square root of the reflected power. Thus $\Delta\omega$ has to be taken between frequency values, at which the induced voltage amounts to $\frac{1}{\sqrt{2}}$ times the voltage induced off resonance. For a depiction of the situation see figure 1.7.

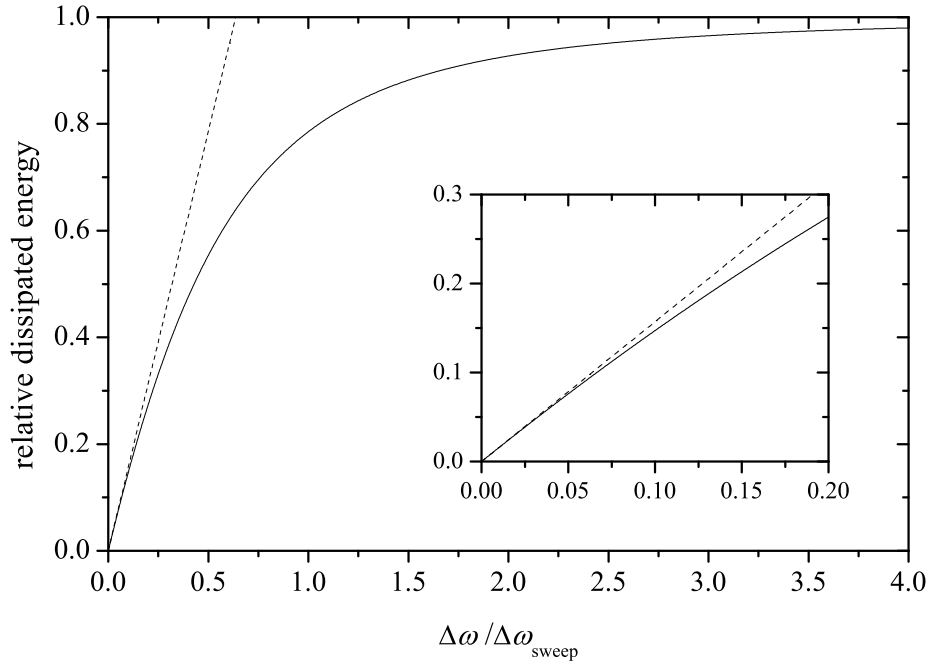


Figure 1.8: Dissipated energy in the cavity during a frequency sweep experiment as a function of the ratio between the resonance width and the sweep width. The energy is given relative to the stationary resonance condition with $\omega = \omega_0$. The dashed line corresponds to a linear relation for $\Delta\omega \ll \Delta\omega_{\text{sweep}}$; this situation is better seen in the enlarged inset.

Another quantity connected with a rapidly swept frequency ramp is the overall dissipated energy in the cavity. During one sweep, energy is only stored in the cavity, when the varied frequency matches the cavity's resonance condition. Thus, the overall stored energy E can be obtained by integrating equation (1.33) over the scanned frequency interval:

$$E = E_0 \frac{\int_{\omega_0 - \frac{\Delta\omega_{\text{sweep}}}{2}}^{\omega_0 + \frac{\Delta\omega_{\text{sweep}}}{2}} \frac{\left(\frac{\Delta\omega}{2}\right)^2}{(\omega - \omega_0)^2 + \left(\frac{\Delta\omega}{2}\right)^2} d\omega}{\Delta\omega_{\text{sweep}}} = E_0 \frac{\Delta\omega}{\Delta\omega_{\text{sweep}}} \arctan \frac{\Delta\omega_{\text{sweep}}}{\Delta\omega}. \quad (1.36)$$

$\Delta\omega_{\text{sweep}}$ hereby denotes the width of the scanned frequency ramp, whereas E_0 is the energy that would be dissipated using a fixed frequency ω_0 . The relation between the overall dissipated energy and the ratio between the resonance width and the sweep width is depicted in figure 1.8. In the case of $\Delta\omega \ll \Delta\omega_{\text{sweep}}$, the arctangent takes the value of

$\frac{\pi}{2}$ and the dissipated energy depends linearly on the sweep width.

In most experiments this phenomenon has little or no effect on the determination of Q . If the sample shows a non-linear response in connection with a slow decay, however, Q might also be a function of the ratio between the resonance width and the sweep width. This could be the case for irradiation-induced sample heating and slow concurrent transfer of heat to a sink together with a sample-temperature-dependent loss factor, for instance.

1.3.3 Electron paramagnetic resonance

Historical digest

Magnetic resonance has been discovered in 1944 by Yevgeny K. Zavoisky in Kazan in the former USSR (nowadays Republic of Tatarstan, Russia) in the form of electron paramagnetic resonance (EPR) of transition metal salts [77, 78]. It even appears, that in 1941 he had observed sporadically the first nuclear magnetic resonance (NMR), but his experiments remained unreproducible [79].

Zavoisky's success was initiated by numerous discoveries. In the late 19th century, the spin as an intrinsic property of the electron or of magnetically active nuclei was unknown. Even the energy quantum – finally proposed by Max Planck in 1900 [80–83] – has not been known yet. In 1896, however, Pieter Zeeman observed the splitting of visible spectral lines when the atoms were brought into an external magnetic field [84, 85]. As a matter of fact he observed the first spin-related phenomenon, *i. e.*, the later-called Zeeman effect. It is induced by splitting of the spin levels in the presence of a magnetic field. The coupling of the non-degenerate spin levels to the electronic system of an atom leads to the so-called fine structure. In 1921 and 1922, Otto Stern and Walter Gerlach directly observed the spin properties by the spatial splitting of beams of silver atoms in a magnetic field gradient. This effect had been explained by the atomic magnetic moment. Furthermore it proved the existence of an orientation quantization of the atomic magnetic moment [86, 87]. In the following decades, experiments based on the same technique allowed the discovery of the nuclear spin of magnetically active nuclei, leading to the hyperfine structure splitting of atomic spectral lines [88]. The concept of the spin finally gained full acceptance in the quantum theory *via* the introduction of a fourth quantum number of the electron by Wolfgang Pauli in 1925 [89]. The model of an intrinsic rotation

of the electron by George E. Uhlenbeck and Samuel Goudsmit appeared in the same year [90, 91].

Based on earlier works by Planck [82] and Einstein [92], Albert Einstein and Paul Ehrenfest have shown the principles of transitions between two quantum states by absorption and stimulated emission of photons in 1923 [93]. Thirteen years later Isidor I. Rabi and coworkers were the first being able to induce spin transitions by the application of an oscillating magnetic field to an atomic beam of hydrogen [94]. Therefore the oscillations of the magnetic moments induced by these transitions are known as Rabi oscillations. Though a method was known to induce transitions between the non-degenerate spin manifolds, it almost took another decade until the first magnetic resonance spectrum has been recorded by Zavoisky at the peak of World War II.

Theory and application

Electron paramagnetic resonance is based on rf induced transitions between the electron spin states. The spin states of a free electron in vacuum are degenerate. Thus they do not allow for any resonance phenomenon. The electron spin is described by the spin operator \mathbf{S} with the eigenvalue $S\hbar$. The spin quantum number S takes the value $\frac{1}{2}$ in the case of a single electron. S quantizes the magnitude of \mathbf{S} :

$$|\mathbf{S}| = \sqrt{S(S+1)}\hbar. \quad (1.37)$$

However, if the spin is brought into an external magnetic field, a unique axis z is introduced in the field direction. The introduction of the unique axis requires the definition of the three spin operators \mathbf{S}_x , \mathbf{S}_y , and \mathbf{S}_z in the three spatial dimensions. Due to the orthogonality of the three operators, only one of them commutes with the Hamilton operator

$$[\mathbf{S}_z, \mathcal{H}]_- = 0, \quad (1.38)$$

while the two remaining components do not commute:

$$[\mathbf{S}_{x,y}, \mathcal{H}]_- \neq 0. \quad (1.39)$$

This leads to a further quantization of \mathbf{S} in the z direction, *i. e.*, the direction of the magnetic field. The quantum number m_S is found in the range $\{-S, -S+1, \dots, S\}$. So, for a single electron with $S = \frac{1}{2}$, m_S can take the values $\pm\frac{1}{2}$. The two m_S values describe

the orientation of the spin vector \mathbf{S} along the surface of a cone with a fixed height of the eigenvalue $m_S\hbar$. On this cone surface, the spin is precessing with the angular frequency ω_L , which is called the Larmor frequency. The splitting of spin states by the precession in an external magnetic field is called the Zeeman effect. It is the most fundamental interaction in conventional EPR. In this case

$$\omega_L = \frac{g\mu_B m_S}{\hbar} B_0 \quad (1.40)$$

follows for the Larmor frequency. B_0 represents the magnitude of the external magnetic field oriented in the z direction. μ_B denotes the Bohr magneton.

Absorption or induced emission of a photon of appropriate frequency ω_L can lead to a transition between the different spin states. During such a transition, quantum coherence is generated between the two eigenstates. Finally the polarization is changed by one unit of \hbar by raising or lowering of m_S by 1. This follows from the selection rule for EPR spectroscopy:

$$\Delta m_S = \pm 1. \quad (1.41)$$

The most general description of spin interactions is based on the spin Hamiltonian

$$\mathcal{H}_{\text{spin}} = \mathcal{H}_{\text{ez}} + \mathcal{H}_{\text{fs}} + \mathcal{H}_{\text{nz}} + \mathcal{H}_{\text{hf}} + \mathcal{H}_{\text{nq}}. \quad (1.42)$$

It contains all possible interactions of the electron spin under investigation with other electron spins, nuclear spins, with the external magnetic field, and with the electric field gradient. The indices employed refer to electron Zeeman (ez), fine structure (fs), nuclear Zeeman (nz), hyperfine (hf), and nuclear quadrupole interaction (nq).

The electron Zeeman interaction was already introduced as the fundamental interaction of EPR. The general form is:

$$\mathcal{H}_{\text{ez}} = \frac{\mu_B}{\hbar} \mathbf{B}_0 \mathbf{g} \mathbf{S}. \quad (1.43)$$

The g factor or Landé factor for the free electron amounts to $g_e = 2.0023$. As a result of orbital magnetism or spin-orbit coupling g can differ from the free electron value.

Second-rank tensors have to be used to describe the coupling between two vectors. The \mathbf{g} matrix⁵ in the principle axis system can be represented by a diagonal 3×3 matrix:

$$\mathbf{g} = \begin{pmatrix} g_{11} & 0 & 0 \\ 0 & g_{22} & 0 \\ 0 & 0 & g_{33} \end{pmatrix}. \quad (1.44)$$

Several cases of matrix symmetry can be deduced on the basis of the g_{ii} element pattern:

$$\begin{aligned} g_{11} = g_{22} = g_{33}: & \text{ isotropic or cubic,} \\ g_{11} = g_{22} \neq g_{33}: & \text{ axial,} \\ g_{11} \neq g_{22} \neq g_{33}: & \text{ orthorhombic.} \end{aligned}$$

If the matrix is of axial symmetry, the two identical elements are combined to one entity g_{\perp} . Per definition g_{\perp} is perpendicular to the unique axis of the \mathbf{g} matrix. The remaining element is oriented parallel to this axis and is denoted as g_{\parallel} .

Magnetically active nuclei, *i. e.*, nuclei with nuclear spin $I \neq 0$, underlie the same interaction as the electron spins. Thus similar relations also hold for the nuclear Zeeman interaction:

$$\mathcal{H}_{\text{nz}} = - \sum_i \frac{\mu_{\text{N}}}{\hbar} g_{\text{N},i} \mathbf{B}_0 \mathbf{I}. \quad (1.45)$$

μ_{N} is the nuclear magneton and g_{N} denotes the nuclear g value. Anisotropy in the nuclear spin manifold does not play a significant role in EPR. For the sake of convenience, $g_{\text{N},i}$ is thus given in scalar form.

If more than one interchangeable electron is present in one system, all electron spins are coupled to one total spin. Each electron contributes to S with an amount of $\frac{1}{2}$. As a consequence, the two level system of the single electron spin is converted to a $(2S + 1)$ manifold. In the case of a non-isotropic symmetry, a coupling between the single electron spins is introduced. This leads to the so-called fine structure interaction:

$$\mathcal{H}_{\text{fs}} = \mathbf{S} \mathbf{D} \mathbf{S} \quad (1.46)$$

The fine structure tensor \mathbf{D} contains both the exchange coupling and the zero field splitting, *i. e.*, the electron quadrupole interaction. It is represented by a scalar value and a

⁵As the magnetic field \mathbf{B}_0 and the spin \mathbf{S} are defined in different spaces, the \mathbf{g} matrix is not a tensor literally.

traceless matrix. In the case of non-interchangeable electrons, the traceless matrix also includes the dipolar interaction of the spins.

The related analog interaction between the electron spin and an arbitrary number i of nuclear spins is called the hyperfine interaction:

$$\mathcal{H}_{\text{hf}} = \sum_i \mathbf{S} \mathbf{A}_i \mathbf{I}_i. \quad (1.47)$$

The same concepts as derived for the fine structure interaction also hold for the hyperfine interaction. The latter is represented by the hyperfine tensor \mathbf{A} . The scalar component of this interaction is given by the Fermi contact interaction, which is a consequence of a finite amplitude of the electronic wave function at the nuclear center. The anisotropic component in terms of a traceless matrix is a result of the dipolar interaction. Therefore it is only present, if the symmetry of the system consisting of an electron and a nuclear spin is lower than cubic.

As last interaction, the nuclear quadrupole interaction is mentioned. It occurs in systems containing nuclei with $I \geq 1$, when an electric field gradient is present at the position of the nucleus. It is represented by

$$\mathcal{H}_{\text{nq}} = \sum_{i \forall I_i \geq 1} \mathbf{I}_i \mathbf{Q} \mathbf{I}_i. \quad (1.48)$$

Although quite often the nuclear quadrupole interaction has revealed to be an important source for spin relaxation, in most cases no first-order effects are detected by EPR.

In our case the magnitude of the electron Zeeman interaction determines the resonance field. From this, information on the spin-orbit coupling can be deduced. The fine structure and hyperfine interactions lead to a splitting of the resonance signal into a number of lines. The structure depends on the multiplicity of the corresponding spin manifold. An analysis of these splittings yields information on the symmetry of the spin center or on the spin density distribution. In the most general case the nuclear Zeeman and nuclear quadrupole interactions cannot be observed directly *via* EPR. Both occur only as a small second-order effect, which is often masked by the line width. Both interactions play a significant role, however, when performing electron nuclear double resonance (ENDOR) or other experiments which are based on the coherence transfer from the nuclear spin manifold to the observed electron spin.

In order to perform a conventional EPR experiment, the sample is placed in a resonant microwave cavity. This results in an enhancement of the amplitude of the local microwave field and dramatically enhances the sensitivity. The microwave frequency is determined by the microwave mode of the resonant cavity. Therefore the magnetic resonance condition is scanned by sweeping the external field. In a continuous wave (c. w.) experiment, the magnetic field is modulated with a low frequency allowing to use the lock-in detection technique. The signal detection is achieved by homodyne down-mixing of the reflected power from the – under non-resonance condition critically coupled – cavity. As a result of the field modulation and lock-in detection, the first derivative of the absorbance *vs.* magnetic field is recorded.

If pulsed EPR is performed, short high power pulses are applied to the overcoupled cavity. This attenuates the cavity ringing and therefore reduces the dead time after the pulses. When investigating inhomogeneously broadened spectra, the detection of the free induction decay (FID) is often not possible. The formation of an electron spin echo (ESE) when refocusing the spin-packets by an inversion pulse can still be possible, however. In the latter case the magnetic field is swept through resonance while integrating the ESE intensity.

1.3.4 Magnetization

The magnetization of a sample is the response of matter to a magnetic field. This response is normally induced by the spin or orbital magnetic momentum of the electrons. If no exchange coupling between spins is present, the magnetization vector \mathbf{M} depends linearly on the external magnetic field strength \mathbf{H} :

$$\mathbf{M} = \chi\mathbf{H}. \tag{1.49}$$

Vectors are omitted in the following and are replaced by scalar values. This is legitimate because magnetization and magnetic field strength are strictly collinear. The factor of proportionality χ is called the magnetic susceptibility. As a result of the linearity between M and H , χ can be described by the ratio between the two entities:

$$\chi = \frac{M}{H}. \tag{1.50}$$

This relation holds only, if the energetic splitting between the different magnetic moments is small relative to the thermal energy represented by $k_B T$. In most cases the splitting is induced by the external magnetic field. Therefore the linear relation breaks down under high field strengths or if the temperature is lowered. Non-linear magnetization also occurs for a strong coupling between the magnetic moments. In the general case, the magnetic susceptibility is represented by the slope of the magnetization curve:

$$\chi = \left(\frac{\partial M}{\partial H} \right). \quad (1.51)$$

In diamagnetic materials, the susceptibility takes negative values characterizing an effective reduction of the magnetic field strength inside the material. This weak effect is normally mediated by magnetic-field-induced ring currents of the electrons. These currents form magnetic moments antiparallel to the external field orientation. If the sample contains unpaired electrons, *i. e.*, non-singlet states, the magnetic moments will orient in parallel to the external field. This leads to an increase of the internal field strength. This behavior is called paramagnetism.

For a strong coupling between the magnetic moments in the sample, the exchange interaction will lead to ferro- or antiferromagnetism, depending on the sign of the exchange coupling. In the case of ferromagnetism, the strongly correlated spins will uniformly align in formed domains. In an external magnetic field, the magnetization of the domains will orient along the external magnetic field vector. This results in a high susceptibility as well as saturation effects at rather low fields. If the external magnetic field is removed, the sample's overall magnetism is partly conserved. As a consequence, remanent magnetization and hysteresis effects occur. In the case of antiferromagnetism, the antiparallel orientation of coupled spins severely reduces the overall magnetization. If $k_B T$ is reasonably low compared to the magnitude of the exchange coupling, an effectively diamagnetic system is formed.

1.4 Motivation

Since their discovery in 1993 [25, 26] single-walled carbon nanotubes (SWNT) have always been an interesting research topic. Theoretical studies proposed many peculiar properties, such as Tomonaga-Luttinger-Liquid (TLL) behavior in the 1D-correlated electron system or outstanding conduction properties. Also extraordinary mechanical proper-

ties have been predicted. Various properties of single tubes could be confirmed by experiment, whereas measurements on bulk samples have been more or less inconclusive. Due to non-ideality of the investigated samples, *e. g.*, variation with respect to chirality and diameter, bundling of the tubes, or because of defects, macroscopic properties such as tensile stress were far below the predicted values. Other remarkable properties observed by experiment had to be traced back to catalyst impurity. Furthermore, the investigation of electronic or magnetic properties of SWNT bulk samples was inhibited totally by catalyst impurity, which could not be removed completely during purification [95]. On the other hand, when applying harsher conditions to thoroughly remove the catalyst, SWNT are modified severely and partly lose their pristine properties.

The development of a method to obtain SWNT in practically pure form without further need to remove the catalyst opened new possibilities in the SWNT research [96]. As response to recent reports on possible superconductivity [97–101] and magnetism [102–111] in pure carbon based materials, investigations of the electronic properties of SWNT have been even intensified. Both superconductivity and magnetism are quite unusual properties for carbon nanotubes. Typically they are restricted to the existence of *d*-electrons, which are clearly absent in carbon systems. However, the discovery of nanoscale carbon materials, *e. g.*, fullerenes, nanotubes, carbon nanofoam, and graphene, established a new class of pure carbon systems with properties not existent in the classical carbon systems graphite and diamond.

In 1999, Kasumov *et al.* found that SWNT – as individual tubes or even in crystalline ropes – can undergo a transition to a superconducting state when being suspended between two superconducting electrodes [97]. Due to the proximity effect the characteristic descriptors of superconductivity, *i. e.*, critical temperature T_c and gap energy 2Δ , are determined mainly by the superconducting contact material and cannot be taken as proof of intrinsic superconductivity of SWNT. However, two years later Tang *et al.* discovered true intrinsic superconductivity in ultra-narrow SWNT without electrical contacting [98]. Reports about superconductivity in SWNT ropes [99] and also in MWNT [100] appeared subsequently. In both cases nanotubes were contacted between normal metal electrodes. Very recently superconductivity in MWNT also has been confirmed by a non-invasive measurement of the Meissner effect [112].

The investigation of magnetism or magnetic anomalies of nanoscale carbon shows a rather large variety of experimental findings and theoretical explanations. In the very early stages of nanotube science, Byszewski *et al.* reported an anomaly in the magnetic

susceptibility in MWNT suggesting a ring-current induced interaction between magnetic moments [102]. Little proposed that the interaction of these ring currents with the ferromagnetic catalyst during the growth of nanotubes would be important [113]. This model has been supported by experiments [114, 115]. Rode *et al.* have found experimental evidence for ferromagnetism in carbon nanofoam being explained by the existence of electrically conducting regions separated by regions of different electronic structure [104]. This observation has been confirmed by Blinc *et al.* [107].

Due to the high diversity of SWNT samples, experimental reports about magnetic anomalies are rather sparse. Theoretical studies, however, propose quite interesting properties. Moradian and Fathalian, for example, have predicted a coupling between semiconducting SWNT and doped magnetic impurities, leading to spin-dependent changes in the density of states (DOS) at the Fermi level and a possible semiconductor to semimetal transition [106]. On the other hand, intrinsic defects cause tremendous changes in the electronic and magnetic properties of SWNT. Ma *et al.* predicted changes both in the magnetic and the electronic properties of graphene and SWNT upon the introduction of vacancies. While defective metallic nanotubes exhibit ferro- or ferrimagnetism, some semiconducting tubes undergo antiferromagnetic ordering. The conversion from metallic to semiconducting tubes and vice versa depending on vacancy concentration has been predicted, too [105]. Orellana and Fuentealba have anticipated ferromagnetism in metallic SWNT under conservation of the electronic properties, when monovacancies are introduced [108]. In nanographene, it is assumed that localized spins of the edge states or topological defects give rise to unconventional magnetism such as carbon-only ferromagnetism, magnetic switching phenomena, or spin glass states [103, 110]. The properties of these states are closely connected to topological line defects in SWNT, which might induce ferromagnetic spin ordering [109]. The latter case is most interesting, as ferromagnetism is anticipated in an electronically saturated system, *i. e.*, without any network edges, dangling bonds, or carrier doping being present. On the basis of experimental findings, very recently an antiferromagnetic ground state due to the opening of a spin-gap in SWNT was proposed. [111].

To probe for indications of superconductivity or magnetic anomalies, the availability of a simple screening method would be most convenient. Of course, magnetic properties can easily be measured for bulk samples. With superconducting quantum interference device (SQUID) measurements, only the total response of the sample can be recorded. This can complicate the analysis of magnetization data if the sought-after effect is masked by

an unwanted signal of greater amplitude. Such spurious signals can arise from different types of nanotubes or from impurities in the bulk sample. Typical signs of superconductivity, *i. e.*, the Meissner effect and the sharp transition to zero resistivity, might be difficult to observe, too. The measurement of the resistive transition requires contacting of individual tubes [98]. This means a very sophisticated and time-consuming task if only certain kinds of nanotubes are supposed to undergo the transition to a superconducting state. A bulk sample of nanotubes with various chiralities which are arranged in bundles of varying diameter and orientation, seems to be no suitable candidate for the measurement of the resistance drop of single tubes or bundles. Note that the overall resistance would be dominated by intertube or interbundle resistance. Furthermore, contacting of SWNT with electrodes might introduce proximity effects [97]. The Meissner effect, *i. e.*, the occurrence of a perfectly diamagnetic phase inside a superconductor, could be masked by magnetic ordering in a different part of the sample. More likely, the Meissner effect might be very small or even suppressed completely. This may be caused by a London penetration depth significantly larger than the transverse dimension of the superconducting channels, *i. e.*, the SWNT diameter. As response to the large fluctuations expected in quasi-1D superconducting channels, the superconducting phase transition might be very broad [98]. In addition to the previously mentioned difficulties, this furthermore complicates an unambiguous identification of superconductivity.

Microwave absorption seems to be a perfect choice to analyze changes in the electronic and/or magnetic properties. This non-invasive method requires only small samples of approximately 1 mg of SWNT material. The resonant variant of microwave absorption, *i. e.*, EPR, has been considered only as a second-choice technique for the investigation of electronic properties of SWNT so far. It cannot be applied to individual tubes due to its inherently low sensitivity. However, as SWNT can exist in metallic and semiconducting forms, they are principally paramagnetic and therefore accessible by means of EPR. Unfortunately, remaining ferromagnetic catalysts – which are still present in significant amount even in purified SWNT samples – complicate the detection of conduction electrons by EPR. Ferromagnetic or superparamagnetic catalyst particles can act as effective spin scattering centers [116]. Except of an early experiment, in which extreme care was taken to completely remove the catalyst [29, 117], further attempts to resolve the Dysonian line shape of conduction electrons in SWNT have failed so far [118–120] or appeared to be inconclusive [111]. On the other hand, individual conducting SWNT, which are embedded in a semiconducting or effectively insulating matrix of tubes of different

electronic properties, are not expected to give rise to typical Dyson resonance lines. Note that this line shape has been derived for spherical metallic samples of vanishing surface-to-volume ratio [121, 122]. This criterion is definitely not met in quasi-1D SWNT. Due to the expected long spin coherence time of charge carriers in the 1D conducting system a rather narrow conduction electron spin signal is expected [42]. Additionally, the theory of spin-charge separation in the TLL state predicts a fine structure in the spin properties of individual metallic tubes [40]. As a consequence, the signature of conduction electrons in individual carbon nanotubes is not expected to be based on a Dyson line. With increasing intertube conductivity, however, the non-vanishing bulk-conductivity might lead to a significant admixture of a dispersive component in resonance. This might give rise to a typical Dyson-like asymmetry of the EPR signal however.

Besides intrinsic conduction electrons in SWNT, defects with an odd number of vacant carbon sites in the honeycomb configuration can introduce spins [105]. These spins are supposed to be localized around the defect center but can also be promoted to the conduction band by thermal activation. Other topological defects, such as pentagon-heptagon pairs or Stone-Wales defects do not introduce spins directly by unpaired electrons because of the even number of carbon atoms involved in this defect. However, these defects could act as efficient electron trapping sites [123], leading to the formation of localized spins.

An important advantage of EPR is its high versatility. It is not only capable to discriminate different magnetic species. Important information on these species are accessible as well. These information can be gained by the interpretation of the spectral shape, *e. g.*, apparent spectral anisotropy, homogeneous or inhomogeneous broadenings, or the occurrence of any fine or hyperfine structure. Even if no detailed information can be obtained directly from simple c. w. EPR measurements, it can often be revealed by pulsed EPR and related experiments. Furthermore, by combining c. w. and pulsed EPR, electron spins can be classified by their dynamics. Localized and itinerant spins, for example, can be discriminated unambiguously by the spin decoherence times. The behavior of EPR signals and the corresponding temperature behavior of the susceptibility can yield further valuable information on the origin and on the properties of the observed spin species.

A technique closely related to EPR is non-resonant microwave absorption, which has been described in detail in section 1.3.2. In EPR, microwave absorption occurs due to magnetic resonance of the electron spins. It is probed by the variation of the external magnetic field. The non-resonant counterpart, however, utilizes a cavity perturbation

technique to directly measure the complex dielectric properties of the sample being under investigation. The absorptive component manifests itself in a change of the cavity quality factor Q . The dispersive part can be detected as a shift in the cavity resonance frequency. Although it is rather sophisticated to obtain absolute values of the complex sample conductivity, relative changes in dielectric properties can be elucidated easily. Thus even electronic changes in a very small part of the bulk sample can be clearly noticed. This has been demonstrated for traces of a superconducting material inhomogeneously embedded in a normal state host in the early days of high- T_c superconductivity [75].

2 Experimental part

Contents

2.1	Sample synthesis and preparation	35
2.1.1	Nanotubes	35
2.1.2	Endohedral fullerenes	36
2.1.3	Fullerene peapods	36
2.2	Instrumentation	37
2.2.1	EPR	37
2.2.2	Non-resonant microwave absorption	38
2.2.3	Magnetization	39

2.1 Sample synthesis and preparation

2.1.1 Nanotubes

SWNT samples were provided graciously by Dr. Kenji Hata from the National Institute of Advanced Industrial Science and Technology (AIST), Tsukuba, Japan. Nanotubes were produced using the “Super-Growth” technique, which uses a controlled amount of water vapor to reduce the degradation of the catalyst during the CVD process. The catalyst lifetime is thereby prolonged [96]. Additionally, due to the significantly enhanced turnover number, the utilized amount of catalyst can be reduced. Ethylene diluted by H₂ in Ar or He, is used as feeding gas, while Fe sputtered on thin films of Al₂O₃ on a Si wafer serves as catalyst. During the CVD, nanotubes grow vertically aligned in a sparse forest which can reach heights of up to 2.5 mm in 10 min growth time. With a total carbon amount of 99.98 % the nanotube purity is very high [96]. Unfortunately, SWNT are obtained with a rather broad diameter distribution. In the first experiments large mean diameters of 3.0 nm have been observed, while recent improvements allowed to reduce the mean diameter to 2.5 nm and below. Simultaneously the nanotube purity could be enhanced. The great advantage of this method – besides the outstanding catalyst activity

– is the possibility for an easy mechanical removal of the SWNT forest, while the iron catalyst sticks to the support plate. This “recycled” support with catalyst can be used repeatedly without reduction in growth efficiency.

For the EPR and non-resonant microwave absorption experiments, approximately 1 mg of the provided SWNT material was transferred to a spin-free EPR quartz tube with 4 mm outer diameter. Sample tubes were sealed in high vacuum (10^{-5} mbar) if not otherwise stated. For magnetization experiments, 6 mg of SWNT material was placed – with the help of two swaps of cotton wool – in the middle of a 150 mm long EPR tube. The SWNT volume was 20 mm in height in this case. The sample tube was sealed in high vacuum.

2.1.2 Endohedral fullerenes

N@C₆₀ was prepared by ion implantation using commercial C₆₀/C₇₀ mixtures [124]. After ion implantation a mixture of nitrogen doped C₆₀ and C₇₀ is obtained with a relative doping concentration of 200 ppm [125]. After dissolution in toluene using Soxhlet extraction, C₇₀ components as well as traces of oxygen adducts and higher fullerenes are removed through column chromatography with a mixture of silica gel and activated charcoal as stationary phase. In order to increase the relative concentration of N@C₆₀ in C₆₀, high performance liquid chromatography (HPLC) has to be evoked. As the difference in the retention times of N@C₆₀ and C₆₀ is less than the C₆₀ peak width in the chromatogram, multiple enrichment steps have to be passed, until a satisfying N@C₆₀ concentration is reached [126]. After removal of the solvent, the powder is dissolved in CS₂. Then the solvent is slowly evaporated overnight in order to obtain the polycrystalline material.

2.1.3 Fullerene peapods

For the peapod synthesis, SWNT are prepared by oxidation in ambient air. This procedure has proven to improve the filling efficiency significantly. SWNT in an open quartz tube are put in an oven which is preheated to 520 °C. After 30 min, the quartz tube is removed and cooled in air. After this process, the SWNT weight loss is typically 20 to 25 %.

Peapods are prepared following a slightly modified procedure by Yudasaka *et al.* [127]. Typically 5 mg of N@C₆₀ are dispersed in an ultrasonic bath in 20 mL ethanol abs. (p. a.). After ultrasonication, 5 mg of SWNT are added which have been heat treated previously. The flask is closed and put in a dark place. After resting for one day, the SWNT flakes are

removed from the ethanol and washed thoroughly in toluene to remove outside fullerenes. The obtained peapod material is then dried at 60 °C and transferred to EPR tubes for further investigation.

2.2 Instrumentation

2.2.1 EPR

c. w. X-Band (9.4 GHz) EPR was performed either on a Bruker ESP 300E or on a Bruker ElexSys E680 spectrometer. The latter device was also used for X-Band pulsed EPR spectroscopy.

The Bruker ESP 300E console was equipped with a Bruker ER 047 MRH-M microwave bridge using a Gunn diode as rf source. Frequency stability was achieved by automatic frequency control (AFC). The frequency was measured by a Hewlett-Packard HP 5342A microwave frequency counter. The magnetic field was generated by a standard Varian electromagnet using a Varian V-7700 power supply. It was controlled by a Bruker ER 032 M field controller with an attached Hall probe. The field calibration was performed using a Bruker ER 035 M NMR Gaussmeter. The field modulated EPR signal was detected by the lock-in technique using a Bruker ER 023 M signal channel with an adjustable modulation frequency from 1.56 to 100 kHz. Field modulation could be applied up to 2 mT peak-to-peak amplitude. The sample was placed in rectangular microwave cavities (Bruker ER 4102 ST or ER 4104 OR) operating as resonators in TE₁₀₂ mode. Sample cooling was achieved within a dynamic continuous flow cryostat (Oxford Instruments ESR 900) using either liquid helium or liquid nitrogen as coolant. The ESR 900 cryostat has been modified with an additional heating wire for higher heating efficiency. The sample temperature was controlled by a PID (proportional-integral-derivative) unit (Oxford ITC 4).

The multi-frequency pulsed EPR spectrometer ElexSys E680 was equipped with a Bruker TeraSpec pulsed X-Band intermediate frequency (IF) bridge. Low power microwave pulses are produced by a Bruker PatternJet and amplified by an Applied Systems Engineering 1 kW traveling wave tube (TWT) amplifier (Model 117). The microwave frequency is controlled by a built-in AFC unit and measured by a built-in frequency counter. When working with an overcoupled cavity, the bridge was operated without frequency stabilization. This was possible due to the inherently high stability of the Gunn source.

In pulsed operation EPR signals were converted to video signals by a Bruker SpecJet. The magnetic field was generated by a Bruker B-E 25 electromagnet powered by a Bruker ER 083 (200/60) power supply and controlled by a built-in field controller and Hall probe. The magnet could be locked to the resonance field by a Bruker ER 033 M field-frequency-lock (FF-lock). A cylindrical dielectric resonator (Bruker ER 4118 X-MD5) operated in TE_{011} mode. Sample cooling was performed using a dynamic continuous flow cryostat (Oxford Instruments CF 935) using liquid He and liquid N_2 as coolant. The temperature control was achieved by an Oxford Instruments ITC 503 PID-controller.

2.2.2 Non-resonant microwave absorption

First measurements of non-resonant microwave absorption have been performed by recording the automatic quality factor reading of the Bruker ESP 300E spectrometer in “tune” mode. This tool is only reliable under certain very specific conditions such as the incident microwave power and the actual Q of the cavity, *i. e.*, a narrow microwave power band and a moderate Q is necessary in combination to allow for Q reading. In practice, Q reading was only possible for incident microwave powers of 0.05 to 0.5 mW. Additionally, Q had to be larger than approximately 1000 to allow for a reliable read-out.

To reproduce the data obtained by the above mentioned technique, the resonance curve width of the sample-loaded cavity in the “tune” mode of the ElexSys E680 spectrometer was recorded. This was performed by measuring the frequency-dependent microwave diode current while slowly sweeping through the cavity resonance. This method is applicable only in a very narrow range of measurement parameters, too, as the diode reading is only possible for currents above 20 μA and below 400 μA . This constricted the incident microwave power to values between 0.1 and 0.5 mW and limited the examination of a possible power dependence of the non-resonant microwave absorption.

As an additional drawback of both techniques, there is no control over sweep parameters such as the sweep rate or the width of the frequency ramp. Both parameters are fixed by the bridge control. In order to enhance the flexibility of all parameters, a simple microwave bridge was constructed [128]. This bridge consisted of an HP 8620A microwave sweeper with an HP 86290B rf plug in as the microwave source. A power amplifier (Miteq AFD3-0812-23P-ST) provided a maximal microwave power output of 23 dBm. Using a calibrated variable attenuator (HP X382A), the microwave power incident on the cavity could be varied by 50 dB. Microwaves reflected in the cavity were divided from the microwave source signal and were guided to the detection arm by a standard circula-

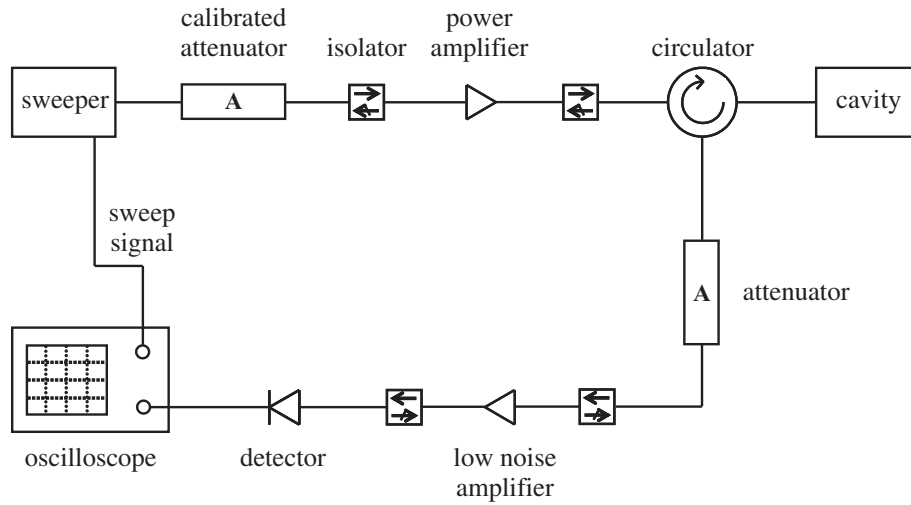


Figure 2.1: Schematic diagram of the bridge setup used for non-resonant microwave absorption experiments.

tor. Signal detection was carried out by a crystal detector (Texscan CD-51 or HP 8473B) and an attached oscilloscope. An additional non-calibrated variable attenuator and a low noise amplifier (Miteq AMF-4S-8010-25-20P) in the detection arm were used to keep the microwave diode response on a constant level. This was required in order to minimize any error by the non-linear voltage response of the diode. The diagram of this setup is shown in figure 2.1. Isolators were used as depicted to avoid damage to the components and to suppress interference due to reflected standing waves in the waveguides.

2.2.3 Magnetization

Magnetization measurements have been performed by Dr. Joris van Slageren at the University of Stuttgart. The setup used was a Quantum Design MPMS-XL7 superconducting quantum interference device (SQUID) magnetometer. Alternating current (AC) magnetization experiments could be performed by evoking field strength modulation with various frequencies from 100 Hz up to 1.5 kHz and amplitudes up to 5.5 Oe. An external magnetic field strength of up to 7 kOe could be applied. The direct current (dc) magnetization was measured by slowly moving the sample through the SQUID and recording the induced currents in the respective coils. The sample temperature could be varied between 1.8 and 300 K.

3 Results and discussion

Contents

3.1 c. w. EPR	41
3.1.1 Spectral analysis	41
3.1.2 Deconvolution of signal A	43
3.1.3 Sensitivity to molecular oxygen	47
3.1.4 Temperature variation	49
3.2 Pulsed EPR	59
3.2.1 Spin echo at $T = 10$ K	59
3.2.2 Echo modulation experiments	63
3.2.3 Transient nutation experiments	67
3.3 Spin-doping using endohedral fullerene peapods	69
3.4 Non-resonant microwave absorption	72
3.4.1 High-temperature dissipation ($T > 15$ K)	72
3.4.2 Low-temperature dissipation ($T < 15$ K)	76
3.4.3 Microwave dispersion	86
3.5 Magnetization	91
3.5.1 DC magnetization at high fields	91
3.5.2 AC magnetization at low fields	93

3.1 c. w. EPR

3.1.1 Spectral analysis

In contrast to electric-arc-produced SWNT (see section 1.4), one expects that CVD grown SWNT produced with the “Super-Growth” method show no or only a weak signal of the paramagnetic catalyst. The reason is the very low residing metal content of only 130 ppm Fe in the final product [96]. In fact, the recorded EPR spectra do not show an indication for any iron related paramagnetic resonance as can be seen in figure 3.1. The

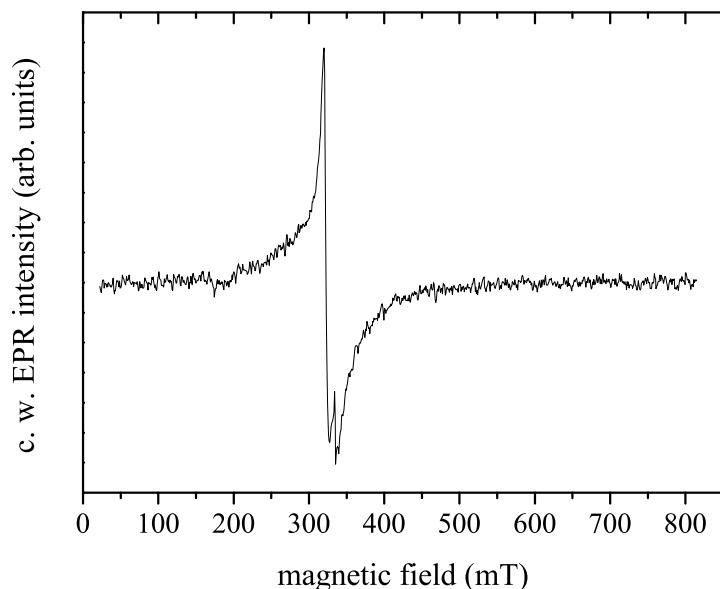


Figure 3.1: c. w. X-Band EPR spectrum of CVD SWNT with a mean diameter of 2.5 nm at room temperature. The sample was degassed under high vacuum (HV) of approximately 10^{-5} mbar pressure.

EPR spectrum recorded at X-Band frequency (9.4 GHz) is dominated by an asymmetrical signal of 12 mT width (peak-to-peak) at the resonance field of 322 mT, corresponding to a g value of approximately 2.07 (in the following denoted as signal **A**). Another resonance line of smaller amplitude (signal **B**) is found at 334 mT with $g = 2.00$, *i. e.*, nearly the free electron g value. Although this g value is typical for unpaired electrons in carbon systems, the signal probably does not arise from simple dangling bonds. The peak-to-peak line width of approximately 5 mT seems to be too large for such centers.

A closer look at the region around $g = 2.00$ in figure 3.2 allows for the discrimination of two different signals, *i. e.*, **B** and **C**. Signal **B** has been described already in the preceding paragraph. The second signal **C** has a much smaller width of only 0.5 mT (peak-to-peak). Considering typical values for carbon based radicals, the latter signal is tentatively attributed to dangling bonds.

It is worth mentioning that the relative intensities of all three signals vary from sample to sample. Because the amplitude of the broad, asymmetrical signal at 322 mT is apparently reduced by more than one order of magnitude from one batch to another, it seems that this signal is not originating from SWNT, but more probable from unwanted species. However, this signal shows an unconventional temperature behavior, which is further de-

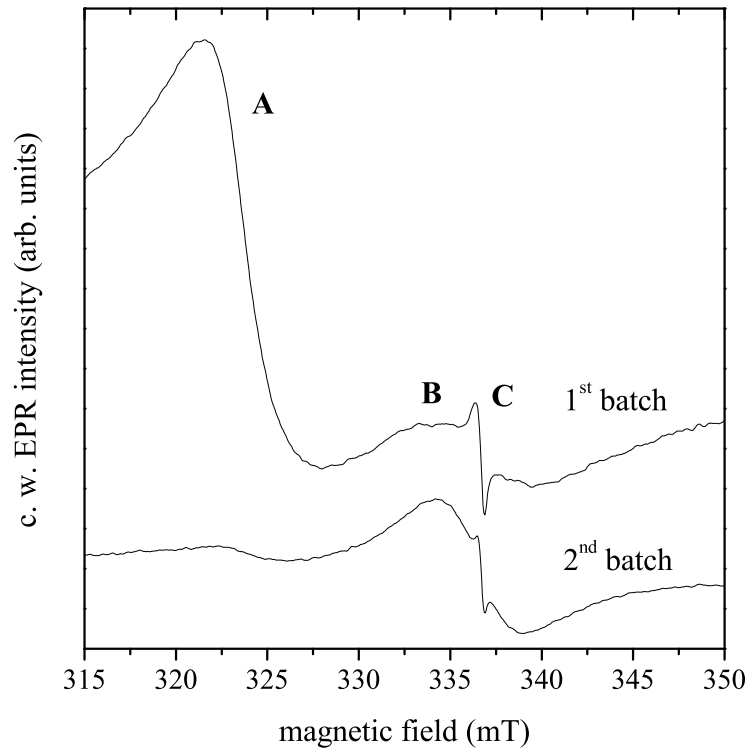


Figure 3.2: c. w. X-Band EPR spectra of two different CVD SWNT samples with a mean diameter of 2.5 nm at room temperature, recorded under HV conditions. Signals are denoted by bold characters in the order of the resonance field.

scribed in section 3.1.4. The determination of the concentration of the corresponding spin species on the basis of the measured EPR intensity is thus not possible.

Summary *EPR spectra of SWNT prepared by the “Super-Growth” method recorded at $\nu = 9.4$ GHz confirm the absence of any remaining catalyst. Furthermore, at least three different EPR signals are observed. Their intensities vary between different production batches.*

3.1.2 Deconvolution of signal A

To gain a better understanding of the origin of the broad asymmetric signal **A**, different approaches have been pursued. Because of the obvious similarity to the expected Dysonian line shape of conduction electrons, a qualitative comparison has been made.

In an early work of Feher and Kip [121], based on theoretical calculations of Dyson [122], the analytical EPR line shape of a thick conducting sample with surface area A and

conductivity σ was derived:

$$P_{\text{EPR}}^{(\text{abs})}(\omega) \propto -\delta A \omega R^2 T_2 \left(\frac{R^4 (x^2 - 1) + 1 - R^2 x}{((R^2 x - 1)^2 + R^4)^2} \left(\frac{2\xi}{R\sqrt{1+x^2}} + R^2 (x+1) - 3 \right) + \frac{2R^2 - 2xR^4}{((R^2 x - 1)^2 + R^4)^2} \left(\frac{2\eta}{R\sqrt{1+x^2}} + R^2 (x+1) - 3 \right) \right). \quad (3.1)$$

δ is the skin depth (see equation (1.21)), and R denotes the ratio between the transit time T_D of the charge carrier through the skin depth and the spin relaxation time T_2 :

$$R = \sqrt{\frac{T_D}{T_2}}. \quad (3.2)$$

Other functions used in equation (3.1) are defined as

$$x = (\omega - \omega_0) T_2, \quad (3.3)$$

$$\xi = \text{sign}(x) \sqrt{\sqrt{1+x^2} - 1}, \quad (3.4)$$

and

$$\eta = \sqrt{\sqrt{1+x^2} + 1}. \quad (3.5)$$

ω represents the angular frequency of the applied electromagnetic radiation and ω_0 is the resonance frequency due to the Zeeman effect in the external magnetic field B_0 with

$$\omega_0 = \frac{g\mu_B}{\hbar} B_0. \quad (3.6)$$

Due to the high complexity of equation (3.1), an analytical fit of the experimental spectrum was not attempted. Instead, several resonance lines of Dysonian shape with different parameters have been calculated in the field domain and have been compared with the experimental signal. A comparison with three different Dysonian resonance curves of best qualitative compliance is displayed in figure 3.3. It is quite obvious that the exact line shape cannot be reproduced sufficiently well with a single set of parameters. This is not totally surprising because the underlying model of Dyson is based on a thick compact conductor, a situation not perfectly met in SWNT. The sample is represented by

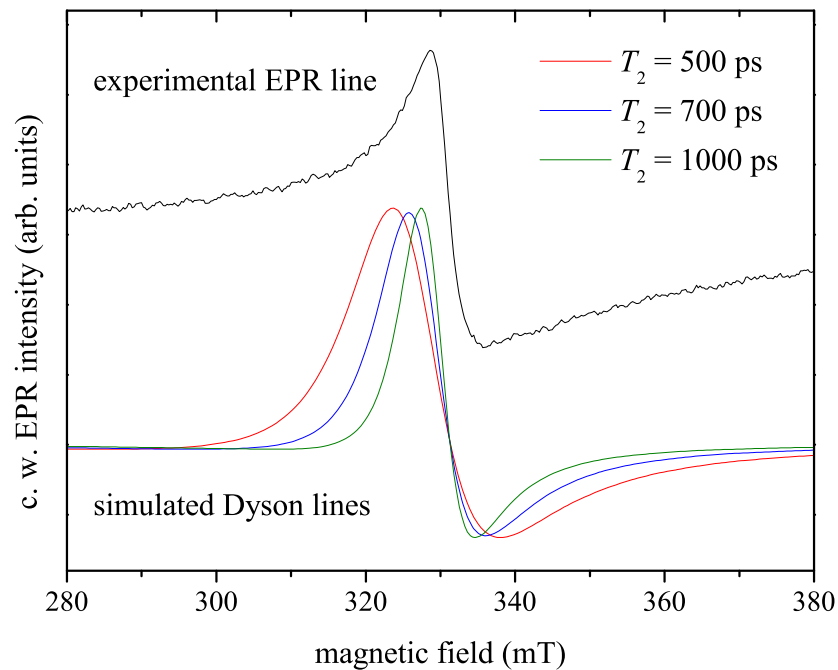


Figure 3.3: Comparison of c. w. X-Band EPR spectra of a CVD SWNT sample (upper signal trace) with analytically derived Dysonian resonance lines of different T_2 values (lower signal traces). For details see text.

a sparse network of one-dimensional conducting wires with a finite intertube resistance. The expected inhomogeneity of the spectral parameters has to be taken into account, too. As can be seen in figure 3.3 the spin relaxation time T_2 plays an important role in line shape. The parameter R – in particular – has to be chosen as large as 300, establishing a practically infinite transit time compared to the spin dephasing. A further increase of R beyond this value did not significantly alter the line shape. In the best fitting results, spin dephasing times of 500 to 1000 ps were used. These short values comply with the experimentally observed very low saturation behavior. Also it was not possible to detect an FID or spin echoes.

Alternatively, the observed signal can be described by multiple Lorentz lines of varying widths with slightly different resonance fields thus reproducing the asymmetrical line shape. Whereas a satisfactory fit with only two components was not possible, the experimental spectrum could be fitted quite well with a set of three Lorentzians. Nevertheless it has to be mentioned that three independent Lorentz curves map nine degrees of freedom, *i. e.*, resonance field, line width and intensity for each of the three curves. Thus the significance of the fit should not be overrated although the agreement between the ex-

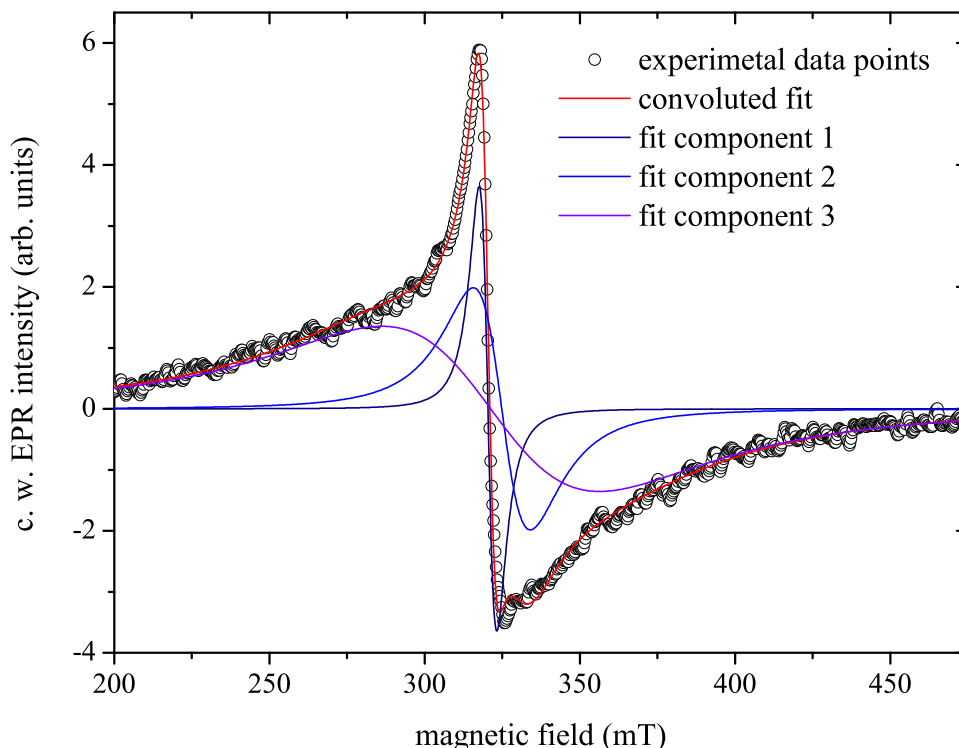


Figure 3.4: Deconvolution of the experimental c. w. X-Band EPR spectra of the CVD SWNT sample (open circles) by three Lorentz lines (blue lines). The resulting convoluted trace is displayed as red line. For details see text.

perimental spectrum and the analytical fit is astonishing. This can be seen in figure 3.4. The fit parameters were chosen as indicated in table 3.1. Due to the strong inverse dependence of the c. w. EPR amplitude on the line width, the most prominent component is formed by only 1.6 % of the total susceptibility. It is noteworthy that the g values of all components show a large deviation from $g = 2.00$, resulting in a significant shift to smaller resonance fields than expected for free electron spins. This shift in the g factor can be explained only by a significant spin-orbit coupling. Assuming a pure carbon material, the orbital momentum can be generated only by highly mobile and thus delocalized spins [129]. A similar explanation was also given by Byszewski and Nabisiałek

Table 3.1: Spectral parameters used for signal deconvolution in figure 3.4.

Component	g value	width (HWHM)	rel. intensity
1	2.074(1)	4.9(1) mT	0.016(1)
2	2.046(2)	16.0(3) mT	0.090(5)
3	2.069(3)	60.8(9) mT	0.894(13)

when investigating highly conducting MWNT samples [130]. In their study, an EPR line with a temperature dependent g factor of up to $g = 2.044$ and a line width of 4.5 mT (peak-to-peak) was observed. In a very early fundamental work of Wagoner and Singer the EPR properties of the charge carriers in graphite have been examined, also revealing a maximum g value of 2.05 [131, 132]. Very recently Kuemmeth *et al.* measured a significant spin-orbit coupling in SWNT by tunneling spectroscopy on individual tubes [133]. This is surprising, as normally the orbital momentum in carbon systems is quenched. However, due to a full circular rotation of the π -orbitals along the tube circumference, a significant orbital momentum is preserved.

All these observations support the conclusion, that this EPR signal arises from itinerant spins, either in residing graphitic carbon clusters or intrinsically in carbon nanotubes which naively can be considered as rolled-up graphene sheets. To further elucidate these findings, the temperature dependence of all EPR signals has to be clarified.

Summary *The low-field asymmetrical signal was compared semi-quantitatively with a model line shape for the conduction electrons in compact metals by Dyson. The comparison yields ultra-short spin-dephasing times of $T_2 = 500 - 1000$ ps. The travel time of charge carriers through the skin-depth is practically infinite to that value. Although a comparison can be legitimated and shows a rather good qualitative agreement, the model cannot be evoked one-to-one to SWNT as a result of the sparseness of the examined material. The asymmetrical signal can be reproduced successfully by the convolution of three Lorentz lines of different resonance field, width, and intensity, showing certain similarities to EPR data of graphite. All observations suggest that these signals have to be traced back to itinerant spins.*

3.1.3 Sensitivity to molecular oxygen

Signal **B** is sensitive to the surrounding atmosphere, *i. e.*, it can be quenched by atmospheric oxygen. The presence of the resonance line can be suppressed in a fully reversible way by exposing the sample to an oxygen containing atmosphere of 200 mbar partial pressure. When the the sample tube is degassed again, the signal will reappear in full intensity. Figure 3.5 shows two EPR spectra of SWNT under high vacuum (HV) condition (10^{-5} mbar) and in a pure oxygen atmosphere of 200 mbar pressure. Because of the perfect reversibility of the effect, any chemical bonding or saturation of dangling bonds with oxygen can be excluded. Recently Bermudez and Ericson examined the in-

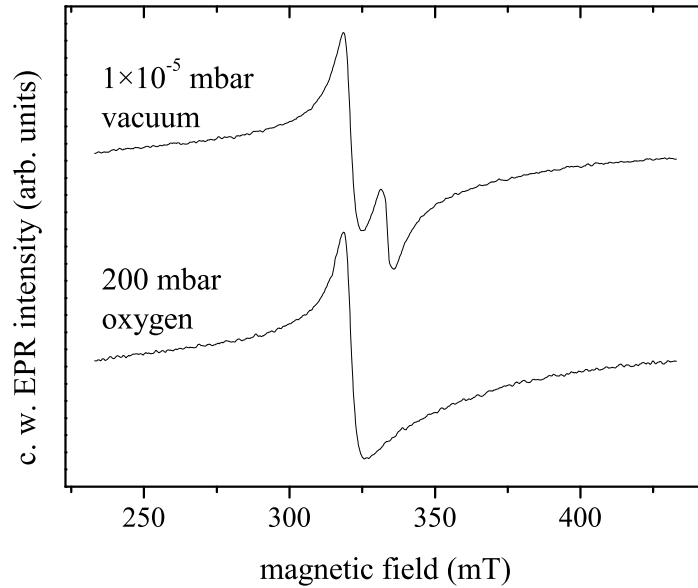


Figure 3.5: c. w. X-Band EPR spectra of one CVD SWNT sample at room temperature, recorded under HV conditions (upper spectrum) and in an oxygen atmosphere of ambient partial pressure (lower spectrum).

teraction between SWNT and oxygen by infrared (IR) spectroscopy [134]. In their report an irreversible modification of SWNT – most probably due to chemical saturation of defects – was observed. Additionally molecular oxygen interacts only weakly and fully reversibly with pristine nanotube walls. Nevertheless, the active center for the electron spin localization has to be accessible easily by molecular oxygen. First indications of this accessibility have been reported by Tang *et al.* [135]. The accessibility of carbon atoms of nanotube walls was further investigated by Kleinhammes *et al.* using ^{13}C NMR and saturation recovery [136]. In comparison with methane and ethane molecules, the weak interaction of O_2 with nanotube walls was confirmed. The full accessibility of ^{13}C by paramagnetic triplet oxygen, however, led to enhanced nuclear spin relaxation.

Instead of permanent chemical modification, paramagnetic exchange coupling between the nanotube spins and the triplet oxygen could lead to severe broadening of the signal. This exchange coupling can be established either by a direct overlap of the spin-carrying orbitals or by another species present in the sample which can interact with both triplet oxygen and the nanotube spin center. In SWNT, the conduction electrons can act as a mediator. They allow for a significant exchange coupling between spins too far apart for direct coupling. It has been discovered theoretically that spin-polarization of the conduction electrons might be responsible for ordered magnetism of low-density defects

in SWNT [108]. Topological line defects in armchair nanotubes can undergo the same ordering transition, too [109]. The latter effect is comparable to graphene edge-state ferromagnetism. An experimental indication on this behavior was also reported by Rode *et al.* when investigating carbon-only ferromagnetism of carbon nanofoam [104]. Another very interesting report by Dag *et al.* predicts a spin-dependent change in the electronic structure of SWNT upon O₂ physisorption [137]. According to the authors, semiconducting zig-zag tubes do not show a significant change in the conduction properties. The metallicity of armchair tubes, however, is lifted only for spin-down states. For spin-up bands it is conserved. Such a behavior would result in a variety of unexpected EPR characteristics.

Summary *Only one signal (B) is sensitive to the presence of an oxygen-containing atmosphere. The total disappearance of this signals upon exposure to molecular oxygen in arbitrary form is fully reversible. This has been demonstrated by sealing the SWNT again in high vacuum. Spins giving rise to the observed EPR signal are intended to be easily accessible by triplet dioxygen. Any chemical interaction can be ruled out. The interaction of O₂ with the nanotube wall is only weak.*

3.1.4 Temperature variation

For a further elucidation of these signals, temperature dependent spectra have been recorded. In figure 3.6 c. w. spectra between 360 and 5 K are shown as a waterfall diagram. At first glance it is quite surprising, that the high-temperature spectra differ fundamentally from the low-temperature ones. In particular, the spectra recorded above 150 K are dominated by the asymmetrical signal **A** centered at $g = 2.07$, whereas at temperatures below 100 K a strong signal at $g = 2.002$ arises. The intensities of both signals follow a non-trivial behavior. The amplitude of the broad signal decreases at lower temperatures. At 150 K it vanishes completely. The rather narrow low-temperature signal shows a totally different temperature dependence. It is hard to detect this signal at higher temperatures as a result of its very small amplitude. However, it shows a remarkably strong build-up starting at 160 K.¹ The further increase in intensity with decreasing temperature is much stronger than the one expected by a simple Curie paramagnetism; details will be treated subsequently. A very unexpected behavior was observed at temperatures below 20 K,

¹It has to be noted that an additional signal in the region of $g = 2.00$ can be identified in figure 3.6 at high temperatures. It has been attributed to a background signal in the probehead. The background signal and the sought-after signal can be separated unambiguously by spectral analysis.

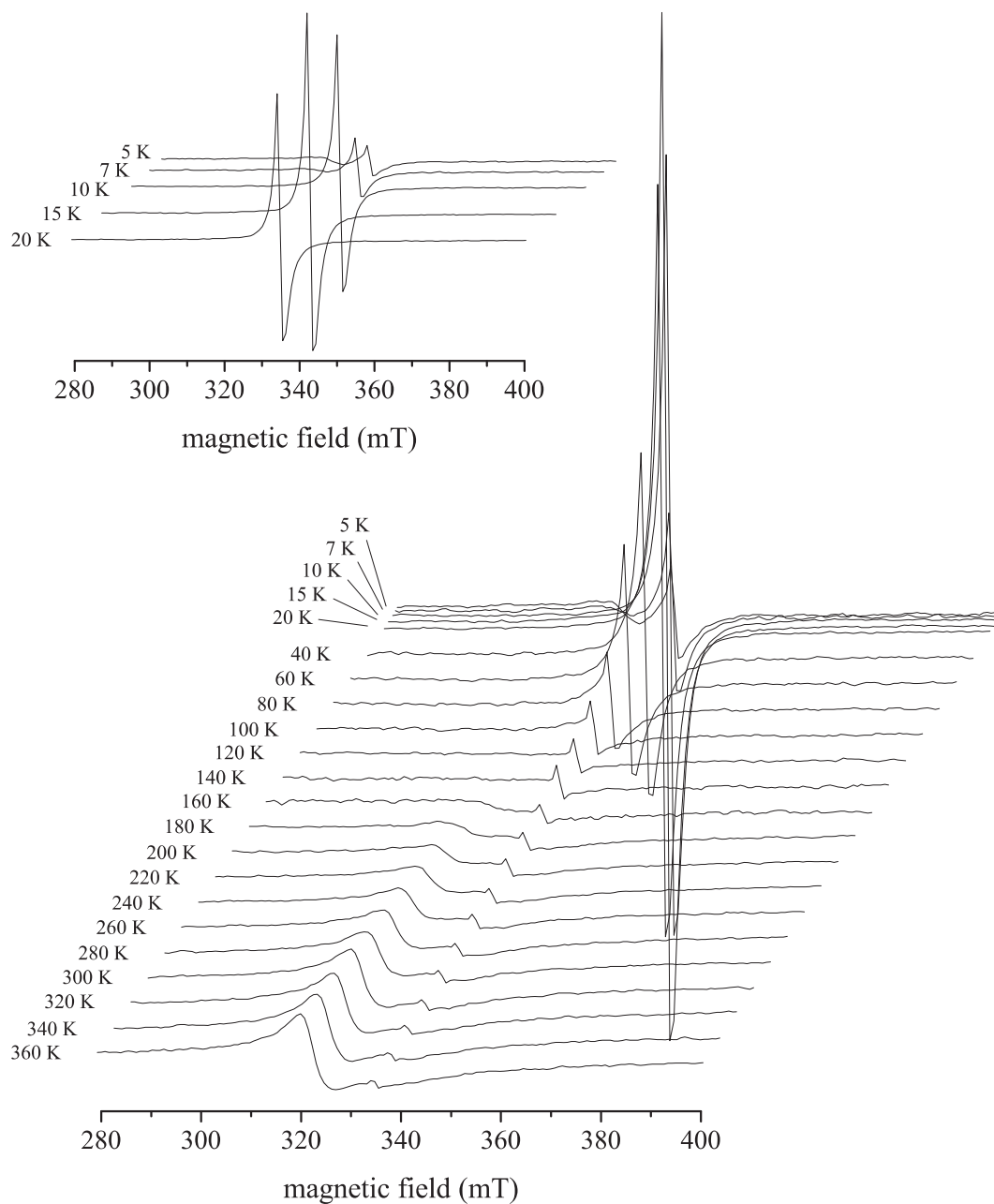


Figure 3.6: c. w. X-Band EPR spectra of a CVD SWNT sample at different temperatures. The data have been recorded under HV conditions. The inset shows the region between 20 and 5 K in more detail.

at which the signal intensity dropped markedly. This decrease was accompanied by a significant reduction in the cavity quality factor, which was recorded simultaneously (see section 3.4.2). This drop in the quality factor will be explained in the following by the onset of a non-linear microwave absorption at these low temperatures (see section 3.4.2). To allow for a better comparison, representative spectra are shown in figure 3.7.

As was already mentioned in section 3.1.2, the high-temperature signal can be deconvoluted into separate curves. To track the intensity of the asymmetrical high-temperature signature a set of three Lorentzian resonance signals is used. To limit the degrees of freedom to a reasonable number, the relative resonance shifts, *i. e.*, the g values, are kept fixed. Whereas the fit showed a good agreement at higher temperatures, the low-temperature spectra could be reproduced with lower accuracy only. Down to a temperature of 200 K the fit yielded reliable results which are plotted in figure 3.8. The indices of the components (referring to table 3.1) are sorted by increasing line width. The narrowest component 1 loses more than one order of magnitude when cooling to 200 K. The amplitude of component 2 is completely invariant. This invariance can be taken as a strong indication of metallic charge carriers. The component with the highest line width (component 3) increases slightly in intensity with decreasing temperature. Due to the high line width however, this value is highly error-prone, indicated by larger error bars at low temperature. As a result, the small intensity variation totally falls into the error-margin and cannot be taken as significant. The line widths of all signals do not show a strong temperature dependence. Whereas the line width of the narrowest component 1 decreases monotonously from 4.7 mT at 360 K to 3.9 mT at 200 K, the two other components increase monotonously in width from 14.9 to 18.8 mT and from 45.8 to 65.8 mT, respectively, when reducing the temperature from 360 K to 200 K.

Furthermore, the temperature dependence of the two most interesting signals – the narrowest component of the broad asymmetrical signal at $g = 2.07$ and the low-temperature signal at $g = 2.002$ – has been examined. The corresponding data for the low-field signal have been shown already in figure 3.8. In order to verify these results, the intensity of the signal was cross-checked by peak-to-peak intensity measurements, which show roughly identical data. For the low-temperature signal, simple peak-to-peak intensity measurements yielded very good and well reproducible results. This uncomplicated technique also minimizes the risks of an error. A misinterpretation might occur when deconvoluting the spectrum into separate species. As a result of the much narrower width of the

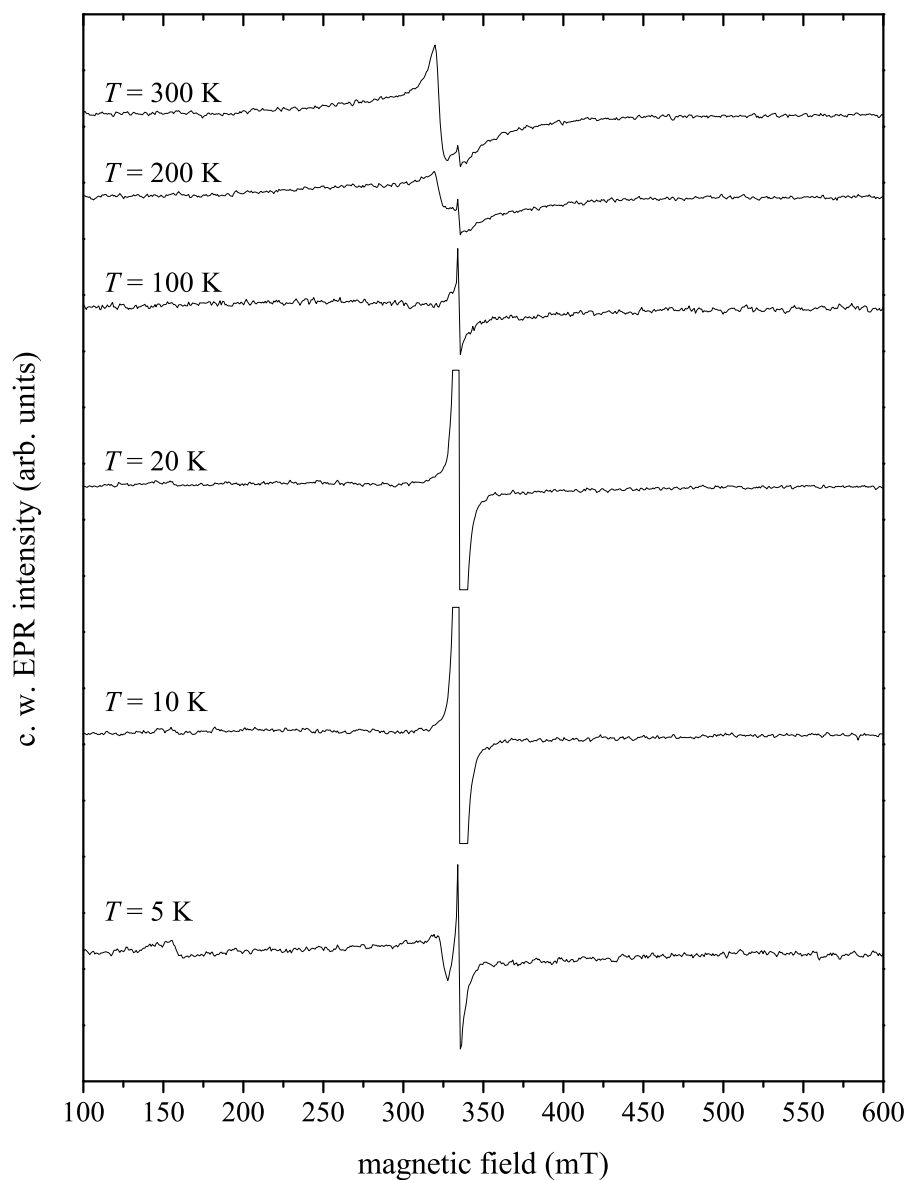


Figure 3.7: c. w. X-Band EPR spectra of a CVD SWNT sample at different temperatures, recorded under HV conditions. To allow for true scale representation of all spectra, the display was limited at temperatures of 10 and 20 K.

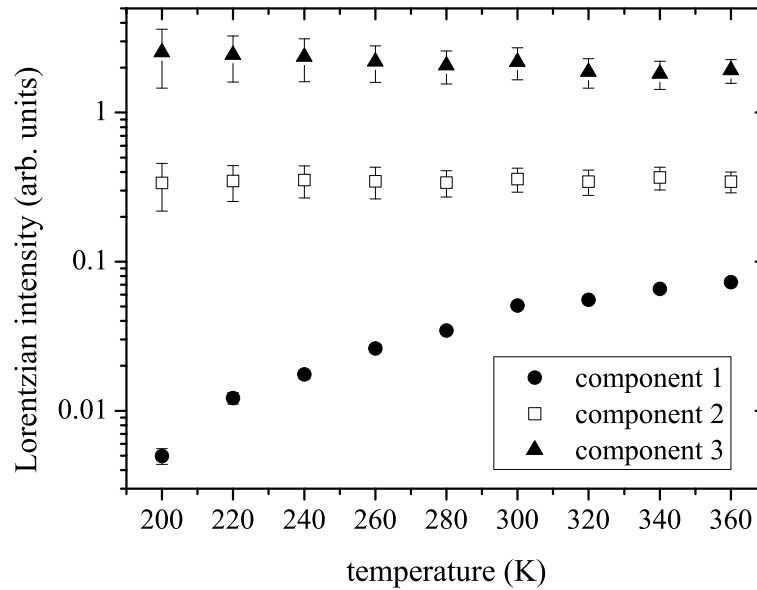


Figure 3.8: c. w. EPR intensity of the high-temperature signal in a CVD SWNT sample obtained *via* spectral deconvolution into three Lorentzian components. Their indices match the numbering in table 3.1. For details of the fit see text. All data were obtained by analyzing the spectra of figure 3.6.

sought-after signal relative to other spectral components, a simple separation by peak-to-peak analysis is possible and the least error-prone technique.

The peak-to-peak width has a large influence on the effective EPR susceptibility when analyzing the c. w. amplitude. A constant peak-to-peak width has been observed in the temperature range studied, however. Therefore the amplitudes in figure 3.9 are displayed without correction due to the line width. This implies that the values can be considered only in arbitrary units. A cross-correlation of all data sets is therefore not possible.

On the left side in figure 3.9 the intensity of the low-temperature dominant narrow signal multiplied by the temperature is plotted versus the temperature. Under the assumption that the population of the spin states follow the Boltzmann law, the values obtained can be treated as “Curie constant” analogs. In this case it can be assumed that the Curie constant is proportional to the effective spin concentration, *i. e.*, to the number of observed spins in the sample. This quantity shows a strong temperature dependence, starting with a near zero value at 160 K and a significant increase with decreasing temperature. This observation has been described already by Salvetat *et al.* It has been explained by a temperature deactivation [138]. Below 15 K however, a dramatic drop in this value occurs. In a recent report, Náfrádi *et al.* observed similar behavior when investigating EPR spectra

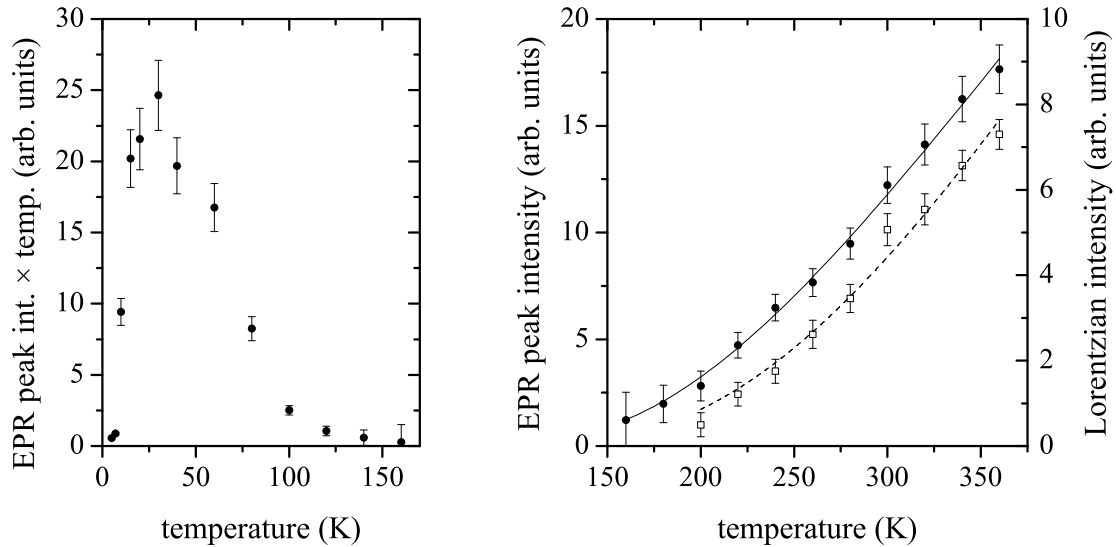


Figure 3.9: Left: c. w. EPR intensity (peak-to-peak) in a CVD SWNT sample. Shown is the intensity of the narrow signal dominant at low temperatures multiplied with temperature. Right: c. w. EPR intensity of the signal dominant at high temperatures (component 1) obtained *via* peak-to-peak analysis (filled circles, left ordinate), and *via* spectral deconvolution (open squares, right ordinate). Solid and dashed lines represent corresponding exponential fits. For details of the fits see text. All data were obtained by analyzing the spectra shown in figure 3.6.

of SWNT, C_{60} peapods, and double-walled carbon nanotubes (DWNT) [139]. The abrupt signal loss at low temperatures, however, was explained by microwave saturation. This picture was supported by power dependent measurements. Admittedly, the experimental observations might suggest this conclusion. In the present work, however, saturation effects as a trivial reason for the observed intensity drop can be excluded. This will be proven by pulsed EPR measurements in section 3.2. Therefore a true reduction of the signal intensity is observed. When interpreting these data, the overall number of spins in the sample does not necessarily have to change. EPR is a microscopic tool to separately investigate spin species with certain spectral properties. Hence, it is more likely that a significant amount of spins of the species under investigation change their spectral properties, resulting in a reduced number of detectable spins.

On the right side of figure 3.9 the corresponding peak-to-peak intensities are found for the broad signal dominant at higher temperatures. It has to be noted that the peak-to-peak amplitudes are displayed, not the temperature multiplied values. In the same graph corresponding data obtained by spectral deconvolution as was explained earlier are dis-

played. Values obtained by peak-to-peak measurements seem to be shifted by a constant value, a behavior that can be explained by a temperature independent component in the convolution. A clear monotonous variation with the temperature is observed, showing increasing intensity with higher temperature. The data were fitted with an Arrhenius-like exponential function:

$$I_{\text{EPR}} \propto \exp\left(-\frac{E_a}{k_B T}\right). \quad (3.7)$$

I_{EPR} denotes the measured EPR intensity as displayed in the right side of figure 3.9 and k_B is the Boltzmann constant. The fit shows a good agreement with the experimental data and yields activation energies of $E_a = 67(2)$ meV for the peak-to-peak intensity data and $85(6)$ meV for the data obtained by the spectral deconvolution. The difference of these values is negligible when considering possible error sources mentioned. The magnitude of this activation energy leads to the conclusion that temperature activated charge carriers can be detected above a threshold temperature of 160 K. As it is expected that intrinsically semiconducting nanotubes show band gaps in the order of 1 eV, the rather small activation energy can be explained only by small-band-gap semiconducting properties or by charge carrier doping. Dopants could be of either p- or n-type, which cannot be distinguished here. Carbon vacancies or foreign atoms like nitrogen or boron could act as doping sites, for instance. In the case of hole doping they form empty local states slightly above the valence band. For electron doping, occupied states would be localized below the conduction band. The former might additionally act as shallow traps, at which charge carriers could condensate at low temperatures. This would result in the formation of localized paramagnetic centers and Curie-like paramagnetism. At high temperatures the localized spins can be promoted to delocalized bands resulting in paramagnetic charge carriers. This state corresponds to a Pauli paramagnetism with a temperature invariant spin susceptibility, which depends only on the density of states at the Fermi surface. The change from the first state, showing a rather diluted spin system with localized states, to the latter can be observed continuously when increasing the temperature from liquid helium temperature to 298 K. Although the significance of the interpretations should be checked carefully, the observation of temperature independent components in figure 3.8 can be taken as an indication for metallic charge carriers. Earlier EPR investigations revealed a temperature dependent g value of charge carrier spins in MWNT [130] between 120 K and the temperature of liquid helium. This dependence could not be reproduced in

this work. The relevant signals could not be observed below 160 K. Insufficient signal-to-noise ratios at lower temperature did not allow for a full spectral analysis. Thus small deviations of the g value could not be resolved in the investigated temperature range.

To allow for a better assignment of the dominant (narrow) EPR signal at low temperatures, the absolute number of spins is determined *via* spin counting. For this purpose, the intensity of the EPR signal of unknown spin concentration is determined by double integration of the c. w. signal. The obtained value is compared with a reference of known spin concentration. This allows for a more or less accurate estimation of the spin concentration in the sample examined. Several factors bearing on measurement practice limit the accuracy of this method. Some of these factors can be: varying conversion factors due to different sample dielectric properties, microwave field inhomogeneity, microwave frequency deviations, or detector sensitivity. However, the accuracy is sufficient enough to determine the order of magnitude of the spin concentration. In particular, an uncertainty factor of three is assumed throughout this work. Due to the very low EPR intensity of the sought-after signal at room temperature, the intensity measurement was performed at 20 K, which refers to the temperature of maximum intensity. Without further knowledge, the spin system is tentatively treated as $S = \frac{1}{2}$. Although no Curie dependence was observed for the signal intensity, it is assumed that the non-degenerate spin level populations follow a Boltzmann distribution. A sample of the stable organic radical galvinoxyl served as reference. Taking into account the above stated assumptions, a spin concentration of $6 \times 10^{18} \text{ g}^{-1}$ or 1.2×10^{-4} per carbon atom is derived. This result confirms the high quality of the SWNT sample and the assumption of a highly diluted spin system.

As mentioned earlier and shown in figure 3.5, an additional signal is only detectable in the absence of molecular oxygen. Hence, the observability of this signal depends strongly on the quality of the EPR sample preparation. In a recent work by Agarwal on the same samples as described in this work, the temperature dependence of this signal was investigated [140]. EPR spectra have been recorded at temperatures between 4 and 300 K and the obtained spectra have been fitted with Lorentz curves. As the already discussed signal of approximately 0.5 mT width emerges at low temperatures, a fitting with a second component was necessary. Intensities of both signals and the associated line widths are depicted in figure 3.6.

On the left side of this graph, the product of the temperature dependent intensities of both signals, *i. e.*, the “narrow” one (0.5 mT line width) and the “broad” one (approx. 5 mT width and oxygen-sensitive), and the temperature is displayed as a function of T .

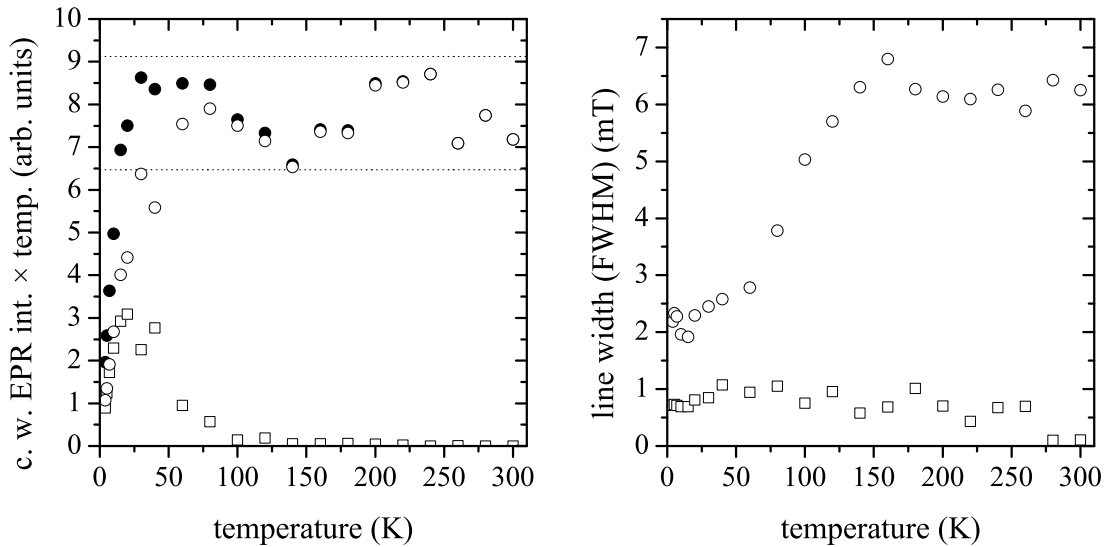


Figure 3.10: Left: c. w. EPR intensity multiplied with temperature in a CVD SWNT sample. The narrow signal dominant at low temperatures is represented by open squares. Open circles show the oxygen-sensitive broad signal. The sum value of both signals is depicted by filled circles. The region within the dotted lines marks the double standard deviation of the sum value data above 10 K. Right: EPR line width of the signals. All data were obtained by spectral deconvolution. For details see text.

As can be seen, the narrow component reproduces the behavior shown in figure 3.9. The broad component, however, shows no variance down to the temperature, at which the intensity of the narrow line starts to increase. While the intensity of the narrow component is enhanced at lower temperatures, the intensity of the broad line is reduced. At temperatures below 15 K both signals decrease. The signal variation observed suggests a one-to-one interconversion of the two signals as a function of the temperature. This assumption is supported by the invariance of the sum value of both intensities above 10 K. Due to the low signal-to-noise ratio in the investigated spectra, the uncertainty – especially at elevated temperatures – is quite high. To take account of this uncertainty, the values within the double standard deviation of the data points above 10 K are marked within dotted lines. It can be clearly seen that the combined intensity at lower temperatures falls significantly below these values.

On the right side of figure 3.6 the line widths of both signals are shown as a function of the temperature. At the same temperature, at which the narrow component starts to grow, the line width of the broad signal shows a dramatic decrease. It is reduced from approximately 6 mT (FWHM) at higher temperatures to around 2 mT at low temperatures. The

width of the narrow component is 0.7 mT (FWHM). It is surprising that apparently no change in the line width of both signals is observed at the temperatures, where the overall signal reduction proceeds. Further pulsed experiments revealed that the broad component could not be refocused by a spin echo. Together with the perfectly Lorentzian line shape, this accounts for a totally homogeneous spin system with a line width determined only by the spin decoherence time. Hence a reduction of the spin volume density in this pool of homogeneous spins, which is observed by an intensity decrease, leads to reduced dipolar coupling and thus to a less effective spin diffusion mechanism. The latter phenomenon causes an enhanced decoherence time and results in a smaller line width. As was also confirmed by pulsed EPR (see section 3.2), the narrow resonance signal could be refocused to form a spin echo with remarkably long phase memory times. The observed line width is more than three orders of magnitude larger than the homogeneous width of one spin packet. Therefore it is practically independent of the spin volume density.

Summary *EPR signals of SWNT show a very interesting temperature dependence. The asymmetrical signal A decreases when lowering the temperature and vanishes below 150 K. The decrease can be tracked down quantitatively by a peak-to-peak amplitude analysis or by signal deconvolution by three Lorentz lines. Both methods yield identical results, i. e., one spectral component shows a sizable temperature variation. An intensity fit with an Arrhenius function results in activation energies between 67 and 85 meV, leading to the conclusion of activated charge carriers as source of the observed EPR signal. The existence of temperature invariant components indicate Pauli paramagnetism due to metallic entities. The intensity examination of the prominent signal at low temperatures resulted in a complicated temperature dependence. The intensity is strongly enhanced when lowering the temperature down to 20 K. Spin susceptibility measurements suggest a spin concentration of approximately 1.2×10^{-4} spins per carbon atom. The highly diluted spin system confirms the high quality of the SWNT. When cooling even further, the signal intensity dropped drastically. The former observation, i. e., the intensity increase at $T = 20$ K, could be correlated with the intensity drop of an additional spectral component visible only in the complete absence of oxygen in the sample. This correlation indicates a partial interconversion of one species into the other between 160 and 20 K. The severe intensity drop below 20 K was accompanied by a non-linear microwave absorption.*

3.2 Pulsed EPR

3.2.1 Spin echo at $T = 10$ K

Pulsed EPR is a reliable method to distinguish between localized and delocalized spins. If the coherence decay is caused by inhomogeneity, the spin coherence that is generated with a single $\frac{\pi}{2}$ -pulse can be refocused by the subsequent application of a π -pulse. It is not possible to form an echo from delocalized spins due to their homogeneous surrounding. Localized spins, however, “see” different environments as a result of dipolar spin-spin interaction or unequal spin centers. In the case of SWNT, defect spins are expected to show varying spectral properties depending on the properties of the SWNT and on the defect type. In addition, due to the natural abundance of magnetically active ^{13}C nuclei, each electron spin is located in a random pattern of statistically distributed nuclear spins. This should result in a pronounced hyperfine interaction inhomogeneity.

At ambient temperature none of the present signals could be refocused by a two-pulse-(Hahn-echo-)sequence to form an echo. Probable origin of this behavior is an ultra-short spin dephasing time of the spins. This results in entirely homogeneously broadened spectra. This assumption is furthermore supported by the fact, that no signal saturation could be observed in c. w. experiments, even when using microwave powers as high as 10 mW. Unfortunately it was not possible to use higher microwave power levels. Here the samples showed signs of heating. This supports the earlier assignment of the broad asymmetrical signal to derive from delocalized spins. At low temperatures, however, a rather strong spin echo of 0.46 mT width (FWHM) emerges at $g = 2.00$. The field swept echo intensity measured at $T = 10$ K is depicted in figure 3.11.

The phase memory time T_m was measured based on a Hahn echo sequence. The pulse separation time τ was gradually increased. The measured echo intensity decay revealed a time constant of $T_m = 32(2)$ μs at $T = 10$ K. By using the expression

$$\delta\nu_{\frac{1}{2}} = \frac{1}{2\pi T_m}, \quad (3.8)$$

this remarkably long time could be translated into a homogeneous (Lorentzian) width (HWHM) of one spin packet of $\delta\nu_{\frac{1}{2}} = 5.0(3)$ kHz. The spectrum was simulated by using the EasySpin package [141]. As can be seen in figure 3.11 the simulation yielded good results when assuming a small \mathbf{g} anisotropy of axial symmetry with $\Delta g = g_{\parallel} - g_{\perp} = -1.1 \times 10^{-3}$ and $g_{\perp} = 2.0021$. The latter value is close to the free electron g . The ho-

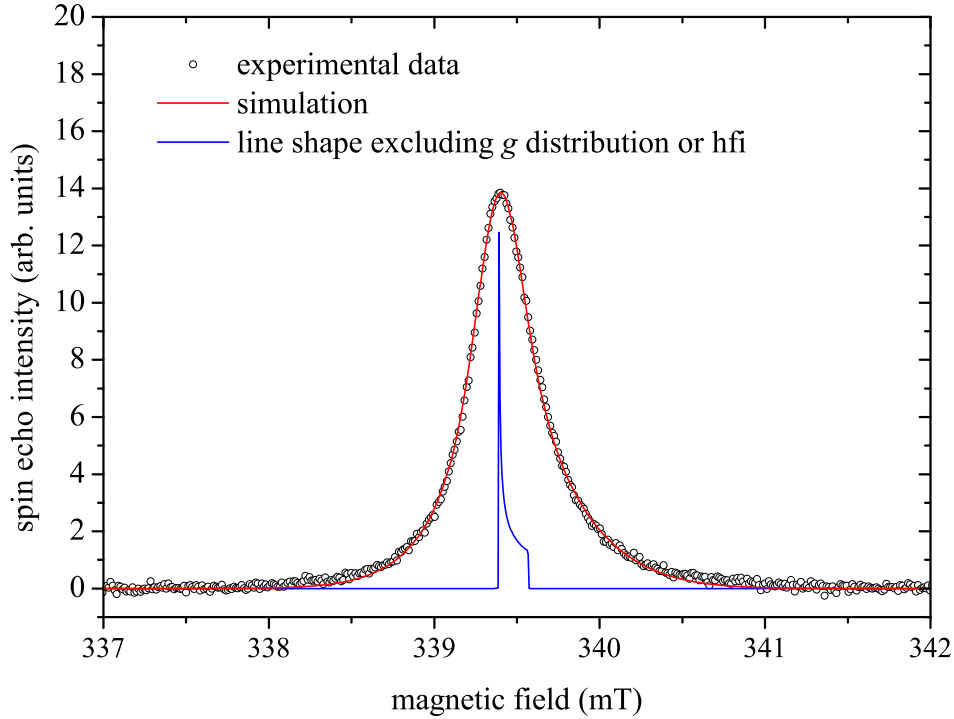


Figure 3.11: Field swept echo intensity at $T = 10$ K of CVD SWNT sample (open circles) at X-Band frequency (9.7 GHz). The pulse sequence (in ns) was $8 - 400 - 16 (\frac{\pi}{2} - \tau - \pi)$. The red line represents a spectral simulation obtained with the EasySpin package. Additionally, one spectral line excluding ^{13}C hyperfine interaction (hfi) or g distribution is displayed (blue line) to demonstrate the extraordinary low homogeneous line width as well as the apparent g anisotropy.

homogeneous line width measured *via* coherence decay was employed in the simulation to determine the amount of inhomogeneous broadening. Gaussian broadenings of 7.1 and 38 MHz (FWHM) in principle axis directions perpendicular and parallel to unique axis have been used in the simulation. On the one hand these broadenings can be caused from deviations in the g value due to differences in local structure². On the other hand, unresolved hyperfine interaction can play a significant role in inhomogeneous broadenings.

Considering these observations, a consistent model is proposed. At $T \leq 10$ K, the observed electron spins are located on surface defects on the SWNT wall. When the tube is oriented parallel to the external magnetic field, a shielding of the magnetic field occurs under the influence of ring currents around the nanotube circumference. Thereby the resonance is shifted to higher external fields. This results in a lower effective g value

²The corresponding Gaussian distributions (FWHM) in g amount to 1.5×10^{-3} and 8×10^{-3} , respectively.

and leads to the observed \mathbf{g} anisotropy. Due to the random orientation of the tubes, the anisotropy is detected as a powder pattern. Additionally the inhomogeneity in tube radii and electronic properties can lead to a broad variation of effective g values in the parallel orientation. In contrast to this behavior, nanotubes oriented perpendicular to the magnetic field show only small g variation.

Because the decoherence is caused by spin diffusion in a pool of isochronous spins, the $\delta v_{\frac{1}{2}}$ value can be in turn converted into a spin volume density n [142]:

$$n \approx \frac{\delta v_{\frac{1}{2}}}{\sqrt{3.8}\gamma^2 h}. \quad (3.9)$$

γ denotes the gyromagnetic ratio and h the Planck constant. This equation yields a value of $n \approx 5 \times 10^{16} \text{ cm}^{-3}$. It should be mentioned that spin diffusion in a pool of magnetically active nuclei which are coupling to the electron spin can also act as an effective pathway for relaxation. In the present case, however, only ^{13}C is present as a magnetic nucleus³. Due to the low natural abundance of ^{13}C , these nuclei form only a diluted nuclear spin matrix. Thus they do not allow for an effective spin diffusion. As already mentioned, the above estimate is only valid for isochronous spin packets. Hence the ratio between the homogeneous width (FWHM) of 10.0 kHz and the mean inhomogeneous width of 7.1 MHz has to be taken into account to derive a total spin volume density. A value of $3.6 \times 10^{19} \text{ cm}^{-3}$ is obtained. Assuming a specific mass of 0.8 g cm^{-3} , an upper limit of 3.4×10^{-4} spins per carbon atom is estimated⁴. Spin counting leads to a value of 1.2×10^{-4} spins per carbon atom (see section 3.1.4). When considering the totally different approaches to obtain the spin concentration, the two procedures are in remarkable agreement.

In order to confirm the temperature behavior as measured by c. w. EPR (see figure 3.9) and also to exclude saturation as trivial reason for the signal loss at low temperature, the echo intensity is recorded as a function of the sample temperature. Pulsed EPR is certainly not the most reliable method to measure intensities. Parameters like relaxation and non-ideality of the pulses might affect the observed intensities. In the present case, however, care was taken to generate ideal pulse angles of $\frac{\pi}{2}$ and π at all temperatures. Furthermore the shot repetition rate was low enough to allow for a complete return to

³For an experimental verification see the following section 3.2.2.

⁴Although the overall volume density of the very sparse sample is only $0.037(2) \text{ g cm}^{-3}$ [143], the close-packed density is taken. This choice can be justified by the fact that spin-diffusion is a short-range interaction and thus the local density in microscopic scale has to be considered.

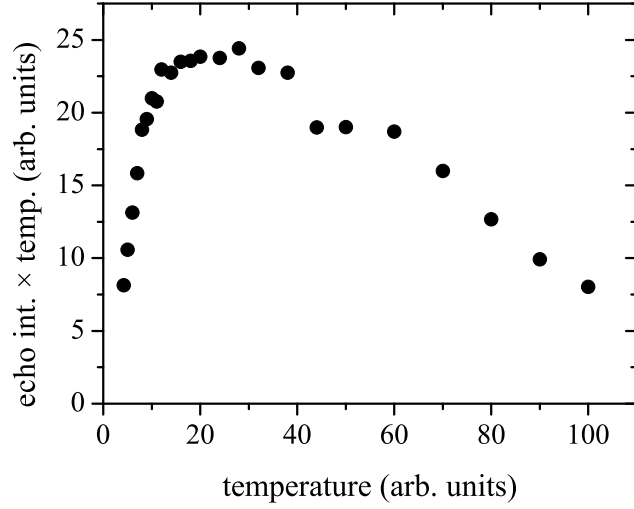


Figure 3.12: Temperature dependence of the spin echo intensity of a CVD SWNT sample at X-Band frequency. The signal intensity was obtained *via* integration over the field-swept spectrum. The pulse sequence (in ns) was $8 - 400 - 16 (\frac{\pi}{2} - \tau - \pi)$.

thermodynamic equilibrium prior to the subsequent pulse sequence. The spin-lattice relaxation time T_1 was determined *via* inversion recovery. In this experiment a π -pulse inverts the spin polarization. After a variable recovery time T the residual polarization is projected by a Hahn echo. This experiment yielded $T_1 \approx 1$ ms at 10 K. Coherence loss due to this relaxation mechanism thus can be neglected during an echo experiment with $\tau = 400$ ns. As the spin-spin relaxation is much more effective in solid state systems, the phase memory time T_m was recorded in addition at each acquisition temperature. These measurements approved that there is no significant change in the spin dephasing rate at all temperatures examined. Hence risks in a possible misinterpretation of echo intensities due to these effects were minimized.

The total echo intensity determined by integrating the field swept echo is shown in figure 3.12. Above 100 K it was practically impossible to detect the spin echo due to the very low intensity. The data show that the intensity anomaly observed by c. w. EPR below 15 K is also reproduced by spin echo acquisition. Due to the fact that saturation effects do not play any role in pulsed experiments, a saturation of the c. w. signal in the performed experiments finally can be excluded.

Summary *At liquid helium temperature an electron spin echo is detected close to the g value of a free electron showing a resonance width (FWHM) of 0.46 mT. This signal is*

identified as the low-temperature prominent line observed by c. w. EPR in section 3.1.4. The phase memory time of the spins is as long as $T_m = 32 \mu\text{s}$. Spectral simulation revealed a small g anisotropy with $g_{\perp} = 2.0021$ and $g_{\parallel} = 2.0010$, which is explained by an anisotropy of a magnetic shielding due to ring currents along the tube's circumference. Furthermore, the resonance line is strongly inhomogeneously broadened, most probably by an unresolved hyperfine interaction with statistically distributed ^{13}C nuclei. By evoking spin diffusion theory, a spin concentration of 3.4×10^{-4} spins per carbon atom is derived. This value confirms – within the characteristic error bars – the concentration which was obtained by a spin susceptibility measurement. The temperature dependence of the echo intensity is also in agreement with c. w. measurements, excluding saturation as a trivial explanation for the signal loss at low temperatures.

3.2.2 Echo modulation experiments

An advanced method to detect the nuclear spins coupled to an electron spin is the electron spin echo envelope modulation (ESEEM) experiment. It can be performed in a two- or three-pulse version, based on the Hahn echo and stimulated echo pulse sequence, respectively. As the stimulated echo intensity decay is only triggered by the spin-lattice relaxation, the echo modulation can be – in principle – recorded much longer than the fast spin-spin relaxation controlled decay of the Hahn echo. Due to long phase memory time of $32 \mu\text{s}$ for the present sample, however, the frequency resolution in the two-pulse ESEEM was not restricted by the coherence decay. Additionally the two-pulse experiment does not suffer from blind-spots as does three-pulse ESEEM. Also the modulation depth was observed to be experimentally larger for the two-pulse ESEEM than for the three-pulse variant. The absolute value Fourier-transformed two-pulse ESEEM spectrum is depicted in figure 3.13. The experiment was performed at the field position of the echo maximum. The pulse sequence covering 1024 data points was $8 \text{ ns} - \tau - 16 \text{ ns}$ with τ increasing in steps of 8 ns. The signal post-processing consisted of an exponential baseline subtraction, apodization with a Hamming-type window function and zero-filling to 8192 points. After Fourier-transformation the absolute value spectrum was created.

As shown in figure 3.13 only one signal can be detected at an rf frequency of 3.6 MHz. This frequency can be identified unambiguously as the nuclear Larmor frequency of ^{13}C ($\nu_{\text{L}} = 3.61 \text{ MHz}$ at an external field of 337.4 mT). A signal arising from the coupling to other magnetically active nuclei, e. g., to the ubiquitous protons with the expected

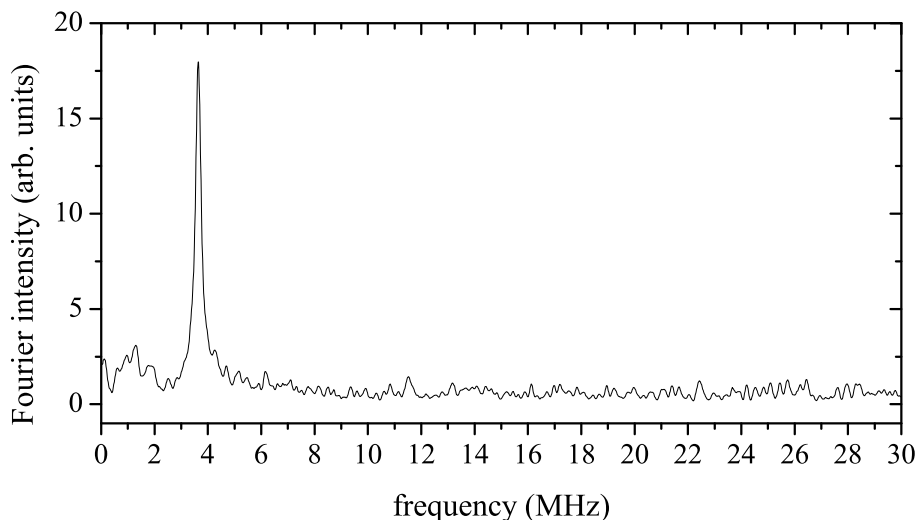


Figure 3.13: X-Band Fourier transformed absolute value of the two-pulse ESEEM spectrum of a CVD SWNT sample recorded at an external field of 337.4 mT, being the field value of maximum echo intensity. For experimental details see text.

Larmor frequency of 14.3 MHz, is missing completely. The absence of protons once more confirms the exceptional chemical quality of the nanotube samples studied.

Unfortunately, no hyperfine structure can be revealed in the measured two-pulse ESEEM. Generally, it is quite difficult to analyze the line shape or signal intensity in ESEEM spectra. This experiment is based on forbidden transitions of nuclear spins between different electron spin manifolds. Thus, very complicated intensity patterns can emerge [144].

For the further investigation of any structure so far hidden, two-dimensional EPR spectroscopy was invoked. In the hyperfine sublevel correlation experiment (HYSCORE) these nuclear spin transitions are attributed from the correlated electron spin manifolds and thus can be separated two-dimensionally on different frequency axes. In detail, a three-pulse stimulated echo sequence is extended by a fourth pulse to transfer coherence from the nuclear spin manifolds to the electron spin. A preparation sequence consisting of two $\frac{\pi}{2}$ -pulses separated by the time τ is followed by a mixing π pulse after the first evolution period t_1 . After a second evolution period t_2 the detection is performed by a final $\frac{\pi}{2}$ -pulse with the echo formation after time τ . In order to generate a maximum coherence transfer, the mixing pulse should be as hard and as unselective as possible. Thus, maximum microwave power with minimum pulse length is employed. A four-step phase cycle has to be used in order to remove all unwanted echoes. In the experiment, all four pulses

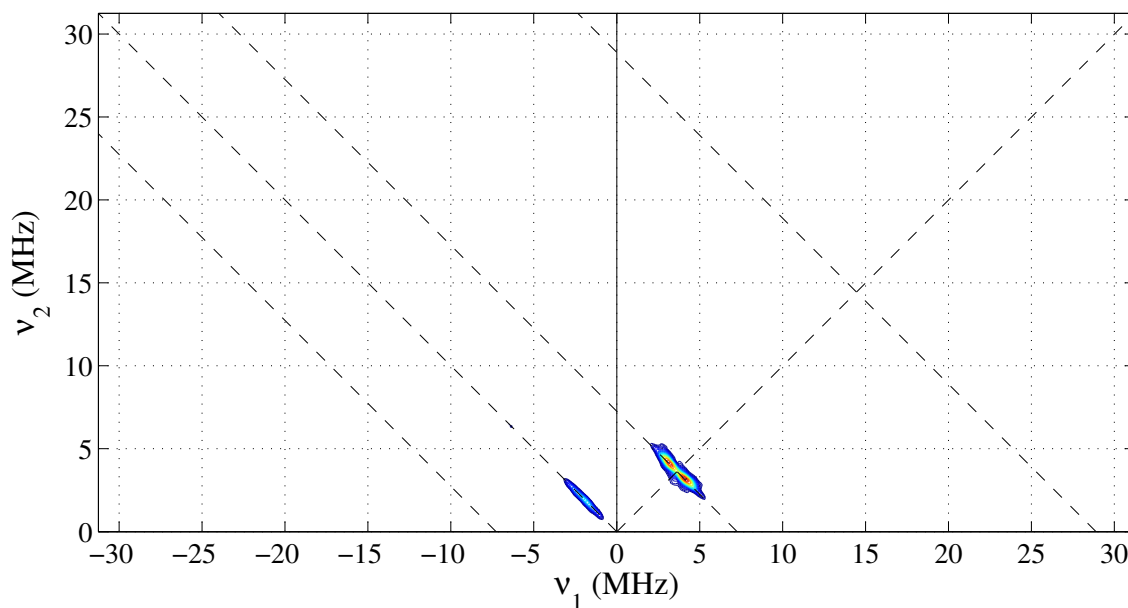


Figure 3.14: Fourier transformed absolute value HYSORE spectrum of a CVD SWNT sample recorded at an external field of 337.4 mT. In addition to the main diagonal and the anti-diagonal, the nuclear Larmor frequencies of ^{13}C and ^1H (corresponding to 3.6 and 14.3 MHz, respectively) are depicted as dashed lines. For experimental details see text.

were of 16 ns length with a third pulse of double microwave field amplitude and thus double nutation frequency ω_1 . The pulse-separation time was chosen as 340 ns. Evolution times t_1 and t_2 have been incrementally increased in steps of 16 ns for 256 points each. The common starting value of t_1 and t_2 was 200 ns. The signal post-processing consisted of a diagonal baseline correction with a second-order polynomial and apodization by a Hamming window function. After zero-filling to 1024×1024 points, two-dimensional fast Fourier transformation was performed. All experiments were performed at the magnetic field corresponding to the maximum echo intensity.

The preliminary observation of only one spectral component is confirmed by the HYSORE spectrum shown in figure 3.14. In contrast to the relatively sharp transition found in two-pulse ESEEM at the nuclear Larmor frequency of ^{13}C (see figure 3.13), a much broader structure is now observed in HYSORE which – additionally – shows a splitting pattern. The splitting reveals two peak maxima, centered exactly at the ^{13}C Larmor frequency. In the depicted HYSORE spectrum this frequency is indicated as a dashed anti-diagonal line.

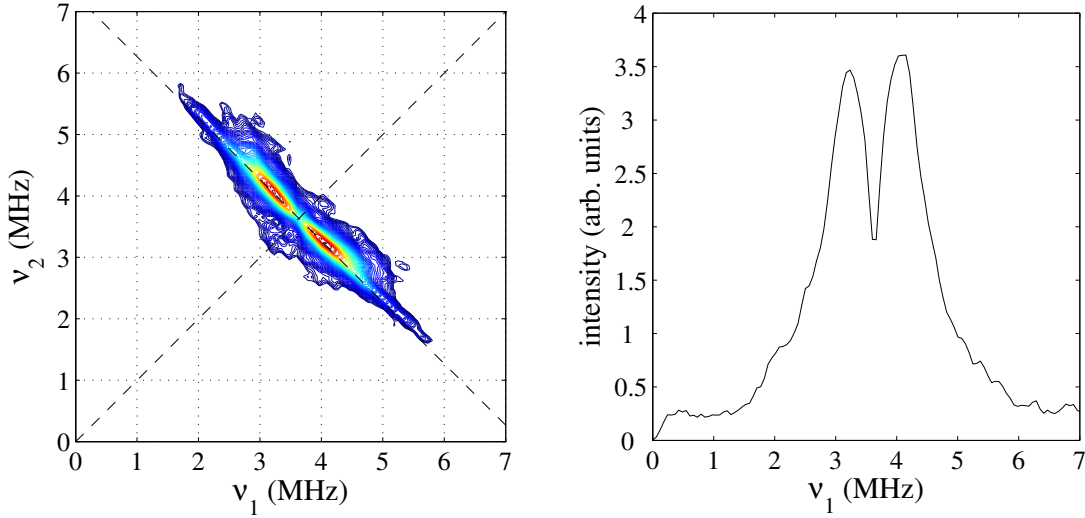


Figure 3.15: Left: Fourier transformed absolute value HYSORE spectrum of a CVD SWNT sample recorded at an external field of 337.4 mT. Only the first quadrant is shown. Right: Projection of the data shown in the left graph on one frequency axis.

The observed structure is typical for hyperfine interaction patterns in the weak coupling regime, *i. e.*, for $a < 2\nu_L$, where a describes the hyperfine coupling constant. It shows two correlation peaks located on the anti-diagonal through the nuclear Larmor frequency which are symmetrically aligned around the main diagonal. For a better spectral resolution another experiment was performed with evolution time increments of 64 ns, resulting in an inherent frequency resolution of 61 kHz. Only the significant first quadrant of the correlation spectrum is shown on the left side in figure 3.15. On the right side a projection of the HYSORE data on the horizontal frequency axis is shown to demonstrate the intensity variation. A quantitative analysis of the line shape is not easily possible. Extreme care is necessary to avoid any over-interpretation of the results. The discrepancy in the line shape between two-pulse ESEEM and HYSORE has been expected. It is caused by experimental boundaries. Both techniques are characterized by non-trivial line-shape and intensity patterns, *e. g.*, due to forbidden transition probabilities, coherence transfer efficiency, or blind spots. The latter are a peculiarity of three-pulse ESEEM and HYSORE spectroscopy.

In the left graph in figure 3.15 the ridges do not show the typical bending expected for a dominant anisotropy of the hyperfine interaction. As a matter of fact it is most likely that a high amount of distribution in the hyperfine interaction leads to the broad ridges. Hyperfine components range between $|a| = 0$ and 4 MHz with a splitting of 850 kHz be-

tween the maxima of the peaks. This fits with the former observation to find no resolved hyperfine interaction in the c. w. and echo detected spectra with an inhomogeneous line width of 7 MHz. The large inhomogeneity in the hyperfine components represents the statistical distribution of electron spins in a random pattern of ^{13}C in their natural abundance of 1.1 %.

Summary *Multi-pulse echo modulation techniques have been used in order to resolve the hidden hyperfine interaction. Two-pulse ESEEM revealed only one nuclear Larmor frequency of 3.6 MHz, which can be unambiguously attributed to ^{13}C . The absence of any other coupling to magnetically active nuclei, especially protons, confirms the high quality of the SWNT sample. Two-dimensional HYSCORE spectra show a broad distribution of hyperfine coupling constants between 0 and 4 MHz. This result is in total agreement both with the measured EPR line width and a theoretical model defined by a pool of statistically distributed ^{13}C nuclei in natural abundance around the probed spin on the nanotube surface.*

3.2.3 Transient nutation experiments

Transient nutation can be performed to distinguish between different spin states. In the simplest nutation experiment one microwave pulse of varying length is applied. If echo detection is preferred, the refocusing pulse in a Hahn echo sequence can be varied in length. During this pulse, the macroscopic magnetization is rotated along an axis perpendicular to the pulse direction. The angle of rotation therefore depends on the pulse length and on the rotation frequency. The latter is a function of the transition probably which is different for individual transitions between the different m_S states. Additionally it depends on the oscillating magnetic field amplitude B_1 . Thus it is directly influenced by the incident microwave pulse power. For $S = \frac{1}{2}$, the nutation frequency ω_1 can be described as follows:

$$\omega_1 \propto \frac{g\mu_B B_1}{\hbar}. \quad (3.10)$$

In the present case the spin nutation experiment was carried out to search for a change in the microwave field amplitude at temperatures above and below the critical temperature of 15 K. Here the significant loss of EPR intensity occurs which might be caused by a reduction of the microwave amplitude at the site of the spins. At this temperature a

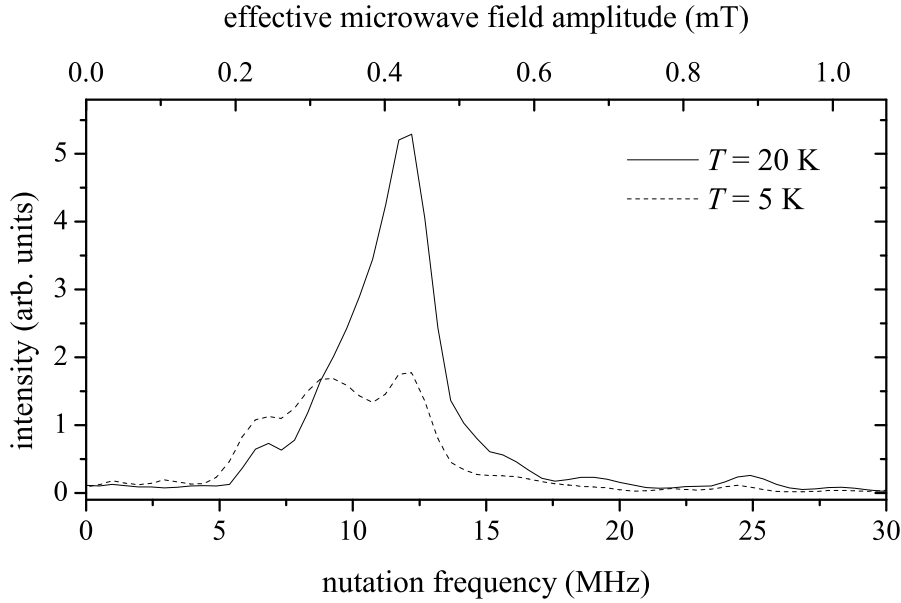


Figure 3.16: Fourier transformed absolute value PEANUT spectrum of a CVD SWNT sample recorded at temperatures of 20 (solid line) and 5 K (dashed line). The upper abscissa represents the effective microwave field strength (under the assumption of $S = \frac{1}{2}$), derived *via* equation (3.10). For experimental details see text.

change in the spin state S is most unlikely. Therefore the observation of different nutation frequencies can be related directly to a change in the local microwave field strength.

The application of only one microwave pulse of increasing length (either as a single pulse or as part of a Hahn echo formation) has several disadvantages. First, the excitation bandwidth, which is a direct function of the pulse length, changes during the experiment. The resulting intensity variation can cause artifacts in the Fourier-transformed (FT) spectrum. Second, the relaxation proceeds during a microwave pulse of varying length. This is again a source of artifact formation. To overcome both deficiencies, one microwave pulse of constant length $T = 2 \mu\text{s}$ is applied in a so-called PEANUT experiment [145]. During that pulse, the microwave phase is switched by π at time t_1 . The switching time is enhanced in steps of 4 ns from $t_1 = 0$ to $t_1 = T$. To avoid any further artifacts, an oscillating echo intensity was recorded with a varying length of the first pulse. After baseline correction, apodization by Hamming window, zero-filling to 2048 points, and Fourier-transformation, the acquired spectra were added in the final step.

The frequency spectra obtained at 5 and 20 K, are depicted in figure 3.16. For ideal microwave pulses, *i. e.*, pulses of perfect rectangular shape and phase, together with a

totally homogeneous microwave field distribution at the sample volume, only one single peak at the Rabi frequency ν_1 would be expected for $S = \frac{1}{2}$. At $T = 20$ K one dominant peak can be found at a Rabi frequency of $\nu_1 = 12$ MHz. The associated microwave field amplitude amounts to $B_1 = 0.43$ mT. Weak shoulders down to 7 MHz are also present. At 5 K however, the relative intensity of these lower frequency components is strongly enhanced. So it is most likely that a considerable amount of the localized centers are no longer experiencing the full microwave field amplitude. This finding indicates that the EPR signal loss below $T = 15$ K is caused by a partial shielding of the microwave field at the location of the spins. It can be assumed that this shielding occurs only in domains. This implies that a significant amount of spatial areas remain unaffected.

Summary *Echo detected transient nutation experiments have been performed on the spin echo which was already examined in section 3.2. Nutation spectra have been recorded at 20 and 5 K. The temperatures have been chosen well above and below the transition to the signal-loss state. The results indicate a partial shift of the nutation frequency at $T = 5$ K, which is absent at 20 K. This shift is interpreted as a shielding of the microwave field amplitude at the spin position. The fact that only a part of the observed spins shows this shielding suggests the formation of certain regions or domains upon crossing the transition temperature in the direction of the low-temperature signal-loss state. The signal-loss occurs only in these domains, whereas the rest of the sample stays in a normal state.*

3.3 Spin-doping using endohedral fullerene peapods

As EPR is a very sensitive tool to discriminate between different paramagnetic species, paramagnetic probes can be used as extrinsic spin markers. Fullerenes are a suitable class of compounds for the investigation of SWNT. Both structures are based on a similar building topology, *i. e.*, fullerenes as well as SWNT are constructed solely of sp^2 -carbon. Thus they mutually exhibit a strong attractive potential. When compared with other probe molecules, fullerenes have another important advantage, *i. e.*, they form so-called peapod structures [48, 51, 52]., This means that fullerenes can enter the hollow core of SWNT, allowing the study of SWNT “from the inside”. As fullerenes normally exist in a diamagnetic ground state, they have to be doped paramagnetically in order to become EPR active.

Endohedral doping of fullerenes with transition metals or rare earth atoms leads to metalloendofullerenes. In these compounds, a charge separation takes place between the encapsulated metal and the fullerene cage, leading to a negatively charged carbon cage and a positively charged metal ion located at the inside wall of the cage [12]. If metalloendofullerenes are incorporated in SWNT, a charge transfer from the fullerene cage to the SWNT wall is possible. Thus a modification of charge transport properties of SWNT was discussed [52]. Experimental indications seem to support that assumption [146,147]. The singly occupied molecular orbitals (SOMO) show a rather large distribution of spin density on the outside wall of these molecules. Thus it is most probable that also a spin transfer to the SWNT wall can occur. This offers the possibility of an exchange coupling between fullerene and SWNT or other fullerenes, leading to a significant change in the EPR characteristics of the spin system. First experiments show promising results [148].

A different approach of paramagnetic doping of fullerenes is the substitution of individual carbon atoms of the cage, *e. g.*, with nitrogen atoms, forming paramagnetic C₅₉N. If diluted in diamagnetic C₆₀, the probe molecules can be incorporated in SWNT⁵. The formation of the C₅₉N-C₆₀ heterodimer at low temperatures and a charge transfer to the nanotube at higher temperatures [149] prevent a reasonable use as an inert spin probe.

In contrast to the metalloendofullerene charge-transfer compounds, nitrogen encapsulated in C₆₀ does not shift a significant amount of spin density to the fullerene cage [150], *i. e.*, the exchange coupling to other spins is negligible. Furthermore, the nitrogen atom is found in its atomic $^4S_{\frac{3}{2}}$ quartet ground state [16]. As a matter of fact N@C₆₀ is an inert probe ideal for the electromagnetic properties of SWNT or peapods [125].

As N@C₆₀ lacks any exchange coupling or spin state transition, very accurate spin-counting experiments can be performed. If saturation effects are avoided, the EPR intensity perfectly follows Curie's law down to lowest temperatures at X-Band frequency. This gives the possibility to track down the EPR intensity of N@C₆₀ and to use it as an internal microwave field strength probe inside the nanotubes. A decrease in the EPR intensity then could be ascribed directly to a shielding of the microwave field at the site of the nitrogen spin by the surrounding carbon nanotubes.

In figure 3.17 the product of the EPR intensity of the N@C₆₀ signal in SWNT with the temperature is plotted. To obtain the EPR intensity data, an analytical fitting of the experimental spectrum with a set of three Lorentz functions was used. This experiment should show no temperature variation due to the perfect Curie behavior of the N@C₆₀

⁵In concentrated C₅₉N samples diamagnetic dimers are formed.

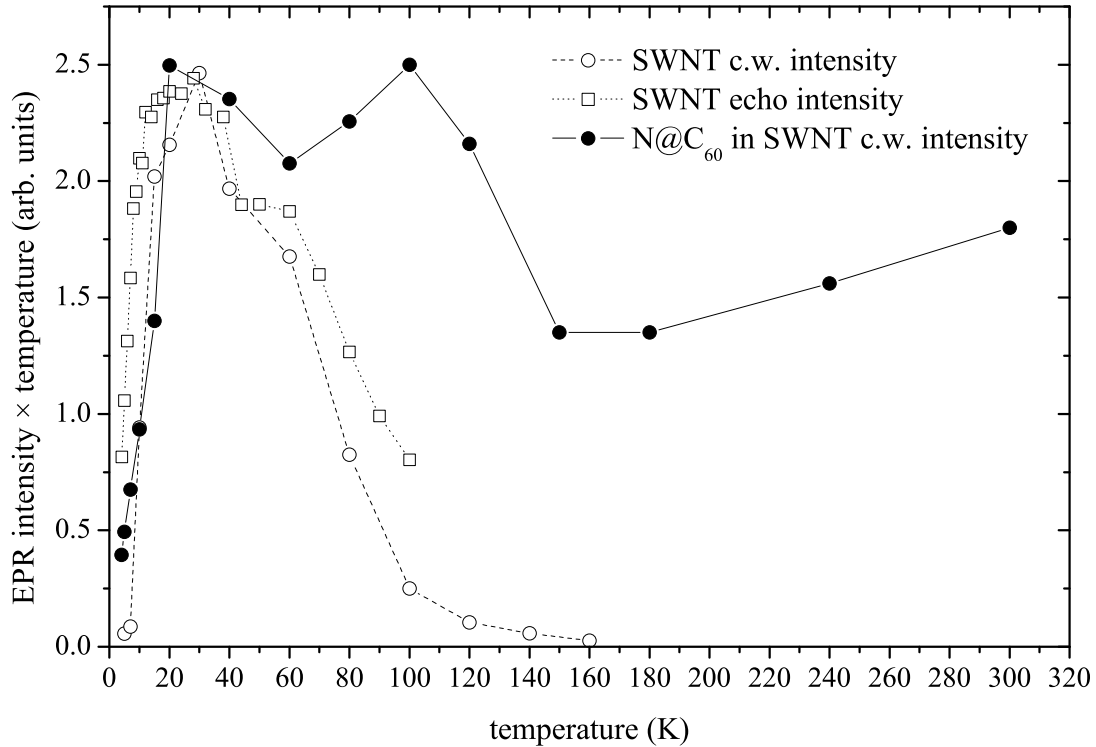


Figure 3.17: Temperature dependence of different EPR signals in samples of CVD SWNT samples: signal of N@C₆₀ recorded by c. w. EPR (filled circles) and 0.5 mT broad signal at $g = 2.00$ of SWNT recorded by c. w. EPR (open circles) as well as echo detection (open squares). Data from the SWNT signals were taken from figures 3.9 and 3.12. Data are plotted as the product of intensity and temperature to visualize deviations from the Curie law. Connection lines between data points should serve only as guides to the eyes.

spin. This criterion is met at temperatures above 20 K. The uncertainty in this temperature range is due to the rather small signal amplitude. At temperatures below 20 K a significant decrease in the signal intensity occurs. It has also been observed for the signal intensity of the low-temperature prominent intrinsic signal of SWNT. In the case of the pristine SWNT signal, a clear distinction between two possible scenarios responsible for this apparent signal loss could not be made. First, the signal loss could be caused by a change of the properties of the observed spin. Second, a change of the electromagnetic field inside the sample could be a reason of the signal reduction. We can now discriminate between both possibilities and therefore the first model can be discarded. A transition in the electromagnetic properties of SWNT either causes a change in the microwave field distribution inside the cavity or introduces local static fields inside the sample volume

which are strongly inhomogeneous. The latter possibility would lead to a large variety of effective resonance fields for spins at different spatial positions, thus resulting in a broad resonance line. As no continuous broadening of the narrow EPR signals of N@C₆₀ was detected in the temperature range above and below 20 K, this explanation is rather unlikely. The former possibility of a change in the microwave field distribution is able to reduce the effective oscillating field at the site of the observed spin and thus a decrease in the resonant microwave absorption amplitude is expected. Moreover, a change in the spin nutation frequency between $T = 20$ K and 5 K, which is interpreted as an inhomogeneous reduction of the microwave field, has already been reported in section 3.2.3. This supports the assumption of a variation in the microwave field distribution being caused by a transition in the electromagnetic properties of SWNT at these low temperatures. Any change in the static magnetic field distribution, however, cannot be excluded on the basis of the performed experiments.

Summary *N@C₆₀ peapods have been prepared to introduce an inert spin probe into SWNT. They offer the possibility to track down the EPR intensity as a function of the temperature. Whereas at temperatures above 20 K the signal intensity follows a perfect Curie paramagnetism, the EPR intensity shows a strong drop for $T < 20$ K. This drop exactly matches the signal-loss observed in the temperature dependent EPR measurements of pure SWNT. N@C₆₀ is known to follow Curie's law down to the lowest temperature studied. As saturation can be excluded in the present case, the abrupt decrease in the EPR intensity below $T = 20$ K has to be correlated with an onset of a local microwave attenuation or shielding of observed spins. However, a change in the static magnetic field distribution inside the sample cannot be ruled out completely.*

3.4 Non-resonant microwave absorption

3.4.1 High-temperature dissipation ($T > 15$ K)

In the present study, the first occurrence of a non-trivial microwave absorption behavior was encountered during the EPR measurements presented in section 3.1.4. As mentioned before, the SWNT samples couple strongly to the microwave field inside of the resonator, *i. e.*, a process complicating any EPR measurement. The cavity Q factor is dramatically reduced in comparison to the empty cavity or to a cavity loaded with a low-loss sample. In preliminary experiments, the loss in the SWNT sample was reduced at lower temper-

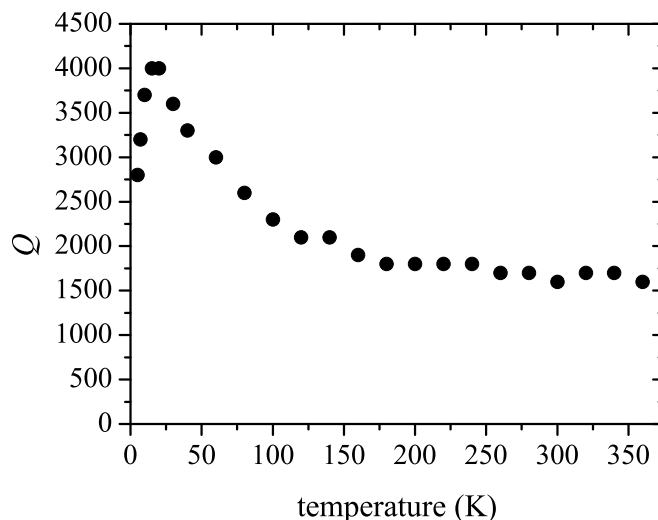


Figure 3.18: Experimental Q factor data of a TE_{102} -cavity as a function of the temperature of SWNT with a mean diameter of 2.5 nm recorded by the automatic Q measurement routine of the ESP 300E EPR spectrometer.

atures. Due to the higher conversion factor, the microwave field in the TE_{102} -resonator was enhanced. However, this sizable temperature dependence of the Q factor caused a possible error in the EPR intensity measurement. To correct for this, the cavity Q factor was also recorded by the automated Q reading of the ESP 300E spectrometer at every temperature step in addition to the EPR spectra (shown in figure 3.6). This preliminary side experiment, however, can be considered as a very important cornerstone of the present work. The Q reading was performed in the presence of the magnetic field but off magnetic resonance. A power level of 100 μ W has been chosen in order to guarantee a reasonable Q reading. The temperature dependence of Q in figure 3.18 is easy to identify. The cavity Q factor is not only a function of the sample loss. It is also influenced by the non-ideality of the cavity and by absorption due to magnetic resonance (see section 1.3.2). In the absence of any resonance condition, absorption due to magnetic resonance can be neglected. The intrinsic resonator dissipation, however, plays an important role. This is particularly valid when using rectangular cavities with relatively low intrinsic Q . As the respective dissipative components behave additively when measuring Q , we get

$$Q^{-1} = Q_0^{-1} + Q_s^{-1}. \quad (3.11)$$

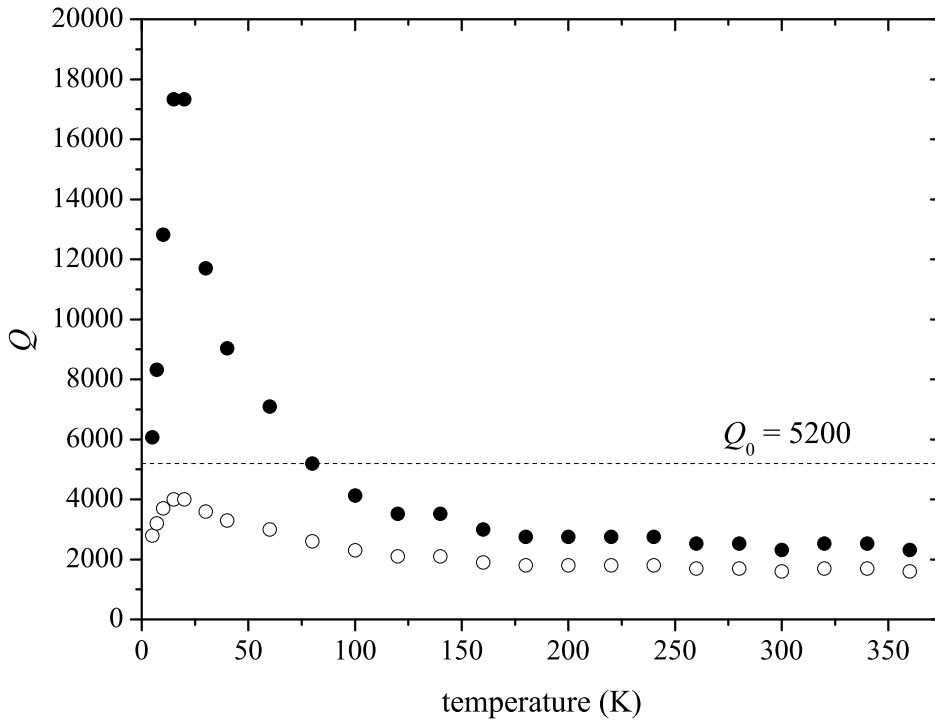


Figure 3.19: Q factor as a function of the temperature of SWNT recorded by the automatic Q measurement routine of the ESP 300E EPR spectrometer. The fictitious sample related Q_s (filled circles) is derived from the overall Q (open circles) and the temperature independent Q_0 of the unloaded TE_{102} -cavity (dashed line) using equation (3.11).

With this equation a virtual “sample derived” Q_s is defined which is inversely proportional to the sample related microwave loss. Together with the data in figure 3.18, the Q factor of the empty cavity was measured as $Q_0 = 5200$. Since the resonator body temperature remains constant during the measurement⁶, this value can be taken as being sample temperature independent. Using equation (3.11) together with the empty cavity Q , the data from figure 3.18 can be corrected to reveal only the sample derived component Q_s , see figure 3.19. Here the temperature dependent changes are much more obvious. The variation in Q_s now spans approximately one order of magnitude. In the high-temperature area ($T > 20$ K), Q_s is monotonously rising with decreasing T , whereas at 15 K the maximum Q_s of more than 17000 is reached. At lower temperature, Q_s is rapidly reduced to a final value of $Q_s \approx 6000$ at $T = 5$ K.

⁶The sample is cooled in a finger Dewar inside the cavity.

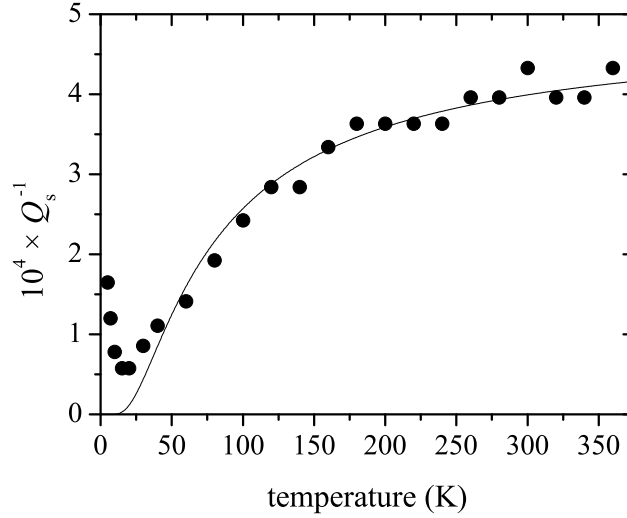


Figure 3.20: Q_s^{-1} as a direct proportional measure for the SWNT sample conductivity σ (filled circles). The solid line represents a fit using equation (3.13) assuming small-band-gap semiconducting SWNT to be the only resistive component in the sample giving rise to a finite Q_s . Only data points with $T \geq 20$ K have been considered for fitting.

As in the case of SWNT and also of SWNT bundles, the conducting channels are small compared to the penetration depth δ . As a matter of fact, Q_s can be taken as being inversely proportional to the electrical sample conductivity σ [54]:

$$Q_s^{-1} \propto \mu \omega \sigma = \frac{2}{\delta^2}, \quad (3.12)$$

where μ denotes the magnetic permeability of the sample and ω represents the angular frequency of the microwave field. On the basis of experimental data, Zhu *et al.* derived a simple model for the conductivity of small-band-gap semiconducting SWNT. In this model the Fermi level is placed in the middle of the energy gap, *i. e.* the SWNT are assumed to be charge neutral. Under the additional assumption of a constant density of states (DOS) in the one-dimensional system,

$$\sigma(T) \propto \ln \left[1 + \exp \left(-\frac{E_g}{k_B T} \right) \right] \quad (3.13)$$

was derived to estimate the temperature dependence of the conductivity σ for SWNT with a gap energy E_g [151]. k_B denotes the Boltzmann constant. An attempt to fit the experimental Q_s^{-1} data with equation (3.13) is shown in figure 3.20. As can be seen,

despite the simplicity of the applied model, the single parameter fit is quite satisfactory and reproduces the experimental data. It has to be mentioned, that the model does only account for one single species of small-band-gap SWNT. It excludes any contribution either from metallic or from wide-band-gap semiconducting tubes. The fit yields a gap energy of $E_g = 7.1(5)$ meV (82(6) K), a value in very good agreement with previous estimates of curvature induced gaps in pseudo-metallic SWNT [35].

Summary *The Q factor of a resonant EPR cavity loaded with SWNT was recorded as a function of the temperature. A sample derived loss factor Q_s^{-1} was introduced, showing a maximum variation of the sample dependent quality factor component of almost one order of magnitude. The significant increase in Q_s when lowering the temperature between 200 and 20 K is explained with the existence of small-band-gap semiconducting tubes. An analytical fit with a simple band gap dependent function yields an energy gap of 7.1 meV, which is in very good agreement with the theory of curvature-induced gaps in pseudo-metallic SWNT.*

3.4.2 Low-temperature dissipation ($T < 15$ K)

At temperatures lower than 15 K an unexpected drop of Q_s occurs, which cannot be rationalized with the above discussed model of semiconducting SWNT. A first intuitive explanation would include a dramatic increase of the sample conductivity when still considering the case of an electromagnetically thin sample.

To check the reproducibility of the observed Q drop, additional experiments have been performed on the ElexSys E680 spectrometer. The setup utilized a dielectric cylindrical TE_{011} -resonator fully enclosed in a flow cryostat. Q was measured by recording the microwave frequency dependence of the reflected power of the critically coupled resonator. For this, the digital display of the detector current was evoked. The difference between frequencies inducing a current equal to $\frac{1}{\sqrt{2}}$ of the maximum value off resonance was taken as the full width at half maximum (FWHM) of the reflected microwave power. The maximum reflected power was determined as the local maximum in the direct vicinity of the cavity resonance dip. Because the display of the detector current was limited to 400 μ A, the measurements have been performed at a microwave power setting of 400 μ W. At this power level the maximum diode current was obtained without exceeding 400 μ A, hence providing maximum accuracy. Measurements have been performed at practically zero field, *i. e.*, the power supply of the EPR magnet was shut down. The remanent field of

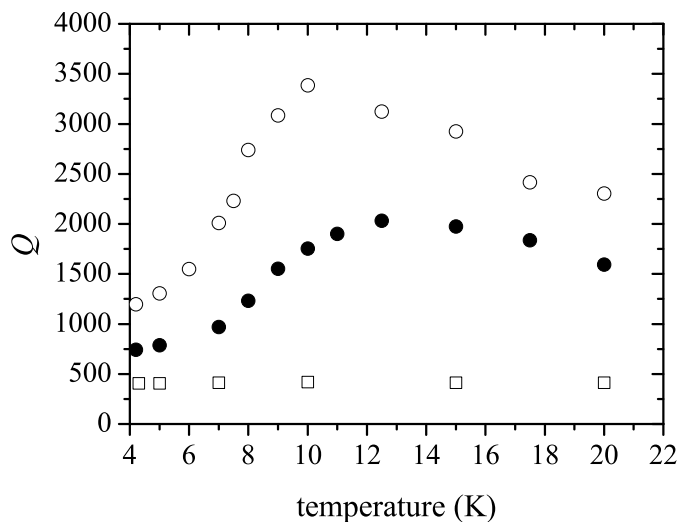


Figure 3.21: Q factor of a dielectric TE_{102} -resonator loaded with CVD SWNT with a mean diameter of 2.5 nm (closed circles) and 3.0 nm (open circles) as well as arc-grown tubes with a mean diameter of 1.4 nm (open squares). Data have been measured on the ElexSys E680 spectrometer (for details see text).

the magnet of approximately 10 mT, however, was still present. The experiment was carried out with three different samples: two CVD grown samples with mean diameters of 2.5 and 3.0 nm as well as one sample of as-produced arc-grown tubes of mean diameter 1.4 nm containing a Ni/Y catalyst. The resulting data are plotted in figure 3.21. Both samples of CVD produced SWNT show the Q drop observed earlier, whereas the quality factor of the cavity loaded with a sample of arc-produced SWNT containing Ni/Y nanoparticles reveal a constant low $Q \approx 400$. These high electromagnetic losses are most likely due to the high content of the metallic catalyst. A correction regarding the intrinsic cavity losses is not necessary. Q_0 was measured as high as 45000 being temperature invariant at these low temperatures. Hence, the cavity losses are very small compared to sample losses and thus can be neglected.

A first very important qualitative observation that helped to understand the Q drop was an unexpected behavior of the spectrometer when trying to tune the cavity at these low temperatures. In a standard EPR experiment the cavity is tuned in a way that no microwave power is reflected at all incident power levels. This is normally achieved by application of a standard protocol. At high microwave attenuation the reference arm bias is set to obtain a detector current of 200 μA . Subsequently the attenuation is lowered and the resonator coupling is adjusted to retain the operating current even at the maximum

microwave power of 200 mW. When the SWNT sample was inserted in the cavity at temperatures above 15 K, the critically coupled resonator showed no power reflection up to a power of at least 10 mW. If the attenuation was further lowered in order to obtain higher microwave fields, the cavity was slightly detuned. This behavior is rationalized by a slight sample heating due to the high power irradiation. At low temperatures ($T < 15$ K), however, the electromagnetic properties of the sample revealed to be dramatically different. With the standard tune protocol it was impossible to obtain a critically coupled resonator throughout the microwave power range. Even at microwave powers as low as 100 μ W, the resonator showed a strong dependence of the reflected power on the incident microwave power.

To further elucidate this observation, quality factor measurements had to be carried out at different microwave power levels. Due to the above mentioned restrictions, however, this was not feasible when using the commercial EPR spectrometers. To overcome this restriction, a home-built microwave bridge as reported in detail in section 2.2.2 was constructed. With this setup, a full control over the incident power as well as over the sweep parameters was achieved. The microwave power could be varied by 50 dB. Measurements have been performed by cooling the sample to 4 K, without applying any microwave power. Subsequently the microwave power was raised in steps of 10 or 5 dB. Care was taken that the resonator was critically coupled during each measurement and that the microwave mode did not change as a function of time due to a temperature shift or other reasons.

The resulting data of a degassed sample of CVD-grown tubes with a mean diameter of 2.5 nm are depicted in figure 3.22. In this graph, the power dependence of the microwave absorption is clearly visible. At higher temperatures, Q does not depend on the microwave power. Only at the highest power settings of more than 10 dBm, a slight deviation can be seen. It gets quite dramatic at the highest incident power. This behavior can be explained by a heating of the sample at these high radiation powers. At 12 K the maximum Q is reached, whereas at an even slightly lower temperature a dramatic change in the microwave absorptive behavior occurs. The quality factor now shows a very strong dependence on the microwave power, with higher absorption at higher power settings. At lowest temperatures a kind of saturation behavior is observable. A lower limit Q of about 600 is reached with microwave powers slightly above 3 dBm. Higher power levels do not reduce the cavity Q any further. At lower power settings the quality factor seems to approach values characteristic for each microwave power.

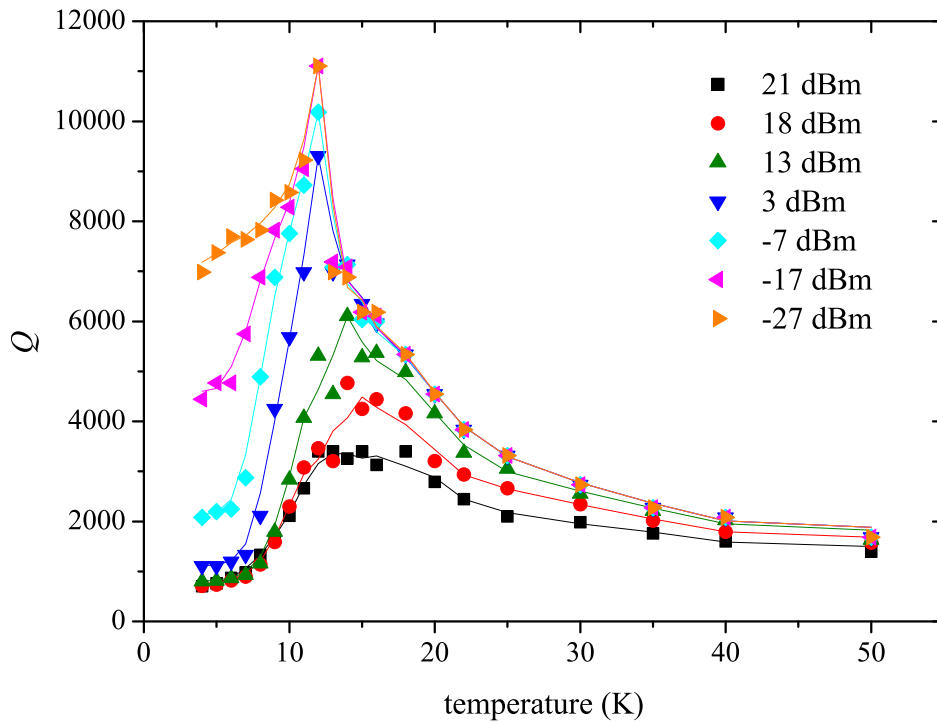


Figure 3.22: Q factor of a dielectric TE_{011} -resonator as a function of the temperature of a degassed CVD SWNT sample with a mean diameter of 2.5 nm. Data were measured on the home-built microwave bridge for different microwave powers. The solid curves were obtained by a partial smoothing of the experimental data and should serve only as guides to the eyes.

Sample heating due to high power microwave irradiation cannot explain this effect. However, radiative heating cannot be totally neglected as SWNT are known to interact strongly with electromagnetic fields. The power dependence at temperatures above 12 K is conveniently explained by sample heating. Up to microwave power levels of 3 dBm there is no dependence of the microwave absorption on the incident power. Only when exceeding this power level, a slightly lower Q at higher incident power is observed. This is caused by a sample temperature slightly higher than the temperature of the surrounding heat sink. When applying a lower irradiation power, the heat transfer between the sample and the surrounding helium atmosphere is sufficient to keep the temperature as low as set. The low-temperature behavior, however, cannot be explained by a trivial heating process. Sample heating cannot lead to the formation of a peak in Q as is observed by experiment. More likely, heating would show a monotonous plateau when reaching a stable sample temperature even if the surrounding bath temperature is lowered.

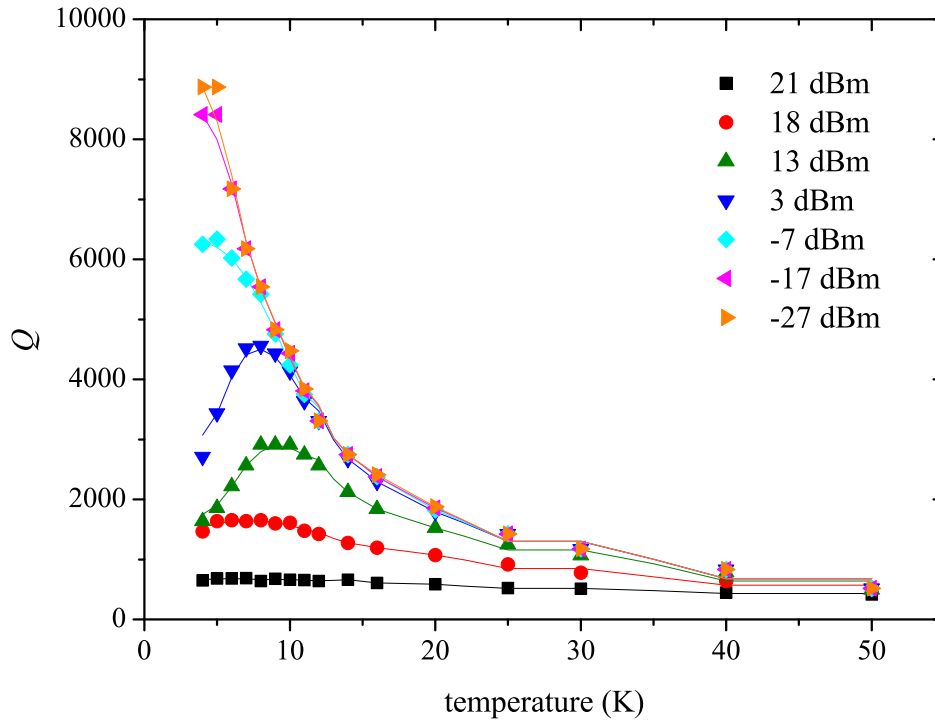


Figure 3.23: Q factor of a dielectric TE_{011} -resonator as a function of the temperature of CVD SWNT in a 200 mbar He atmosphere. Data were measured on the home-built microwave bridge for different microwave powers. The solid curves were obtained by a partial smoothing of the experimental data and should serve only as guides to the eyes.

To further exclude effects of sample heating in the experiment, a sample additionally filled with helium gas at a pressure of 200 mbar was prepared. In the above presented measurements in the evacuated tube only the small sample-glass contacts served as thermal conducting channels. Helium as a highly thermally conducting medium improves the heat transfer. The pressure of 200 mbar was chosen to prevent gas condensation even at the lowest temperature of 4 K. The data of the measurements are shown in figure 3.23. It is obvious that there is no direct influence of Helium gas on this effect.

In another figure (figure 3.24), the power dependence of the microwave absorption is illustrated for different temperatures. The electromagnetic loss, which is inversely proportional to the quality factor, was chosen as ordinate. In order to display only the interesting non-linear absorption component, loss levels at low microwave power levels have been fitted exponentially to approximately determine the virtual zero-power loss

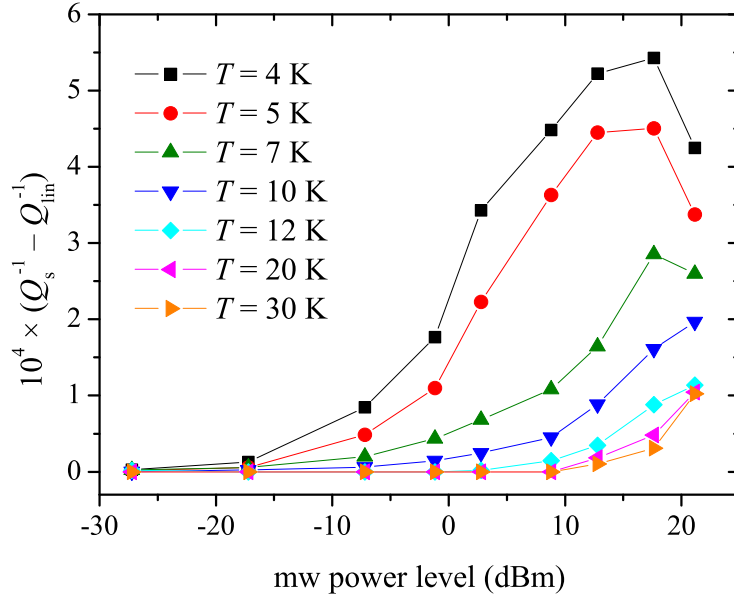


Figure 3.24: Non-linear power loss of SWNT as a function of the incident microwave power for different sample temperatures. The solid lines should serve only as guides to the eyes.

Q_{lin}^{-1} . That linear absorption was subtracted subsequently to yield the non-linear loss:

$$Q_{\text{non-lin}}^{-1} = Q_s^{-1} - Q_{\text{lin}}^{-1} \quad (3.14)$$

For microwave power levels smaller than 10 dBm, non-linear components exist only for temperatures below 15 K. The sample heating at higher power levels has a great impact on the absorption characteristics. Therefore, the highest power levels should not be considered in the present analysis to avoid any misinterpretation.

The experimental data from figure 3.23 can be described qualitatively by a phenomenological function $f(P_{\text{mw}})$. This function describes the power dependence of the non-linear microwave absorption:

$$f(P_{\text{mw}}) \propto 1 - \frac{0.996}{1 + \exp\left(\frac{P_{\text{mw}} - 1.52 \text{ dBm}}{4.5 \text{ dBm}}\right)}. \quad (3.15)$$

P_{mw} is the microwave power level in dBm. The power dependence parameters were derived by fitting the experimental 4 K data both qualitatively and quantitatively (see figure 3.25, left graph). A function $f(T)$ characterizes the corresponding temperature dependence. This function representing a partial phase transition is treated as a relative

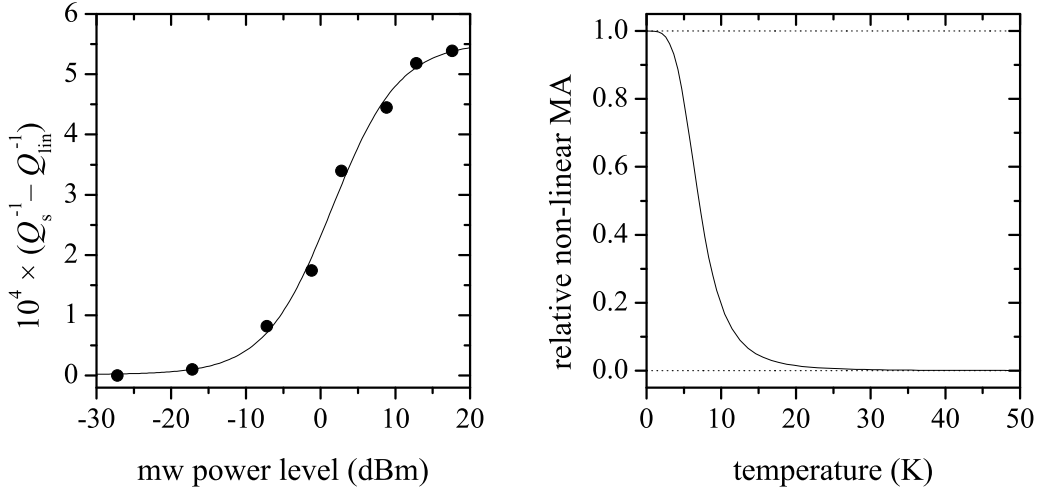


Figure 3.25: Left: experimental values of the non-linear microwave absorption (filled circles) together with a fit using equation (3.15). Right: Temperature dependence of the phase transition between the non-linear dispersive state at low temperatures and the Ohmic state according to equation (3.16). The ordinate denotes the ratio of admixture of the non-linear microwave absorption (MA). For details see text.

admixture of the non-linear dissipative state to a conventional Ohmic loss state:

$$f(T) = \frac{1}{1 + \frac{T^4}{7 \text{ K}}}. \quad (3.16)$$

Equation (3.16) was chosen to represent a smooth transition from the non-linear dispersive state to an Ohmic one (see figure 3.25, right graph). The mean transition temperature of 7 K was obtained by a manual fit of the Q factor runs in figure 3.26 to the experimental curves.

As can be seen in figure 3.26, the qualitative behavior can be well reproduced by this phenomenological approach. It is shown that a transition occurs between a non-linear dissipative state at low temperatures to an Ohmic-loss state at higher temperature. The mean transition temperature of 7 K shows a rather broad distribution. It is an outcome of the inhomogeneity in the sample consisting of nanotubes of varying length, diameter, chirality, chemical purity, and constitutional imperfection. The detailed mechanism of the non-linear power loss in the low-temperature state cannot be identified with this model.

At very low temperatures ($T < 10$ K), a slow change of the resonator mode occurred when raising the microwave power. That “creeping” behavior took place in the time

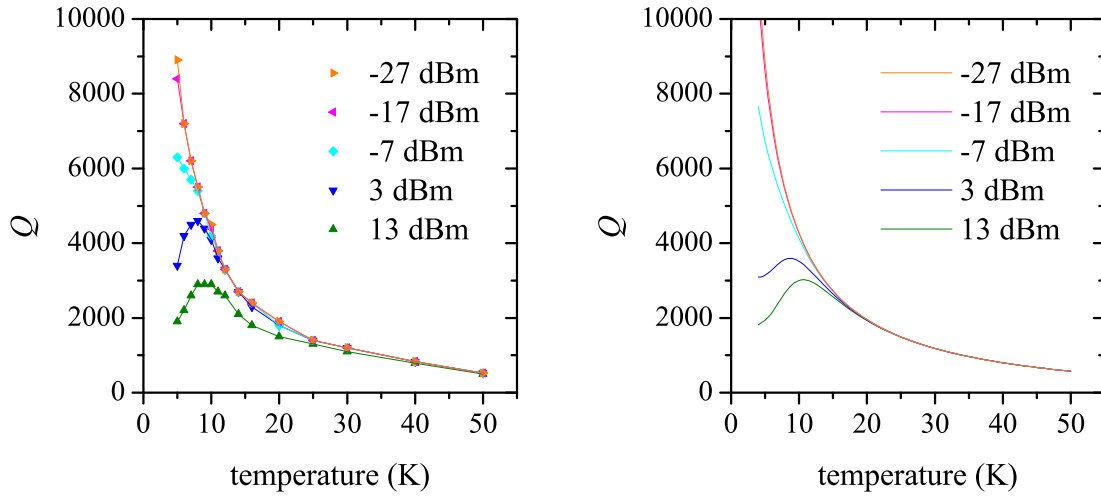


Figure 3.26: Semi-empirical simulation of the temperature dependence of the quality factor of a cylindrical TE_{011} -cavity filled with CVD SWNT with a mean diameter of 2.5 nm for various microwave power levels. In the left graph the experimental data are shown, connected by lines as guides for the eyes, whereas in the right graph the corresponding simulated curves are displayed. All curves were obtained with one single set of parameters. For details see text.

scale of several minutes. It is investigated further in section 3.4.3. Another unusual observation was a thermal bistability of the sample when the temperature of the cryostat was some degrees below the “transition temperature” separating the non-linear dissipative state from the Ohmic state. At this temperature the sample “switched” between both states. This switching became visible as an abrupt change of Q between two distinct values. It seemed that the switching time was infinitesimally small as the new Q value was reached instantaneously. The switching rate had been a function of the incident microwave power. At lowest powers a switching did not occur and a Q factor in the high limit was measured; see figure 3.22 for the lowest power level. When slowly increasing the microwave power, the Q factor dropped due to the non-linear absorption. When exceeding a critical power level, the Q factor switched to a higher value for a short time. After another time interval the back and forth switching started again. This behavior is rationalized as follows: At temperatures slightly below the transition temperature and at low microwave power levels, the sample is in a non-linear dissipative state. As the incident power increases, more and more energy is transferred to the sample, leading to a significant heating until the sample undergoes a transition to an Ohmic state with low and

linear absorption⁷. This leads to a sudden reduction of the energy dissipation. It implies that a concurrent cooling of the sample by surrounding helium causes a back switch to the non-linear dissipative state, after which the process can start again from the beginning.

The switching between both states was also accompanied by a resonance frequency shift of the cavity by up to 5 MHz. The lower frequency was observed in the non-linear dissipative state. Frequency shifts are further investigated in the subsequent section 3.4.2 where a possible explanation is given, too. At lower temperature the bistability could not be observed. Thus we have an indication that energy dissipation cannot lead to a sudden transition to the Ohmic state if the sample temperature – or more precisely – the temperature of the surrounding Helium is below a critical value. It should be noted that all experiments have been repeated at different magnetic fields up to 1 T and also in a setup outside of the magnetic coils, *i. e.*, at earth's magnetic field. A dependence on the magnetic field, however, could not be observed. Additionally an omnidirectional electromagnet was employed which allowed applying a magnetic field up to 30 mT in arbitrary orientation. Experiments with the magnetic field applied in different directions did not lead to a different result. Also magnetic-field modulated microwave absorption experiments have been carried out in a standard EPR spectrometer (ElexSys E680). They did not yield useful results.

Similar results, including loss in EPR intensity accompanied with non-resonant microwave absorption at low temperature, were published by Byszewski *et al.* for alkali metal-doped fullerene superconductors [152]. The characteristics of microwave absorption point to the existence of granular, powder-like superconductors. In [152] temperature dependent EPR intensity data are presented, too, which show a significant intensity loss with the onset of superconductivity. This decrease is very similar to the EPR intensity loss in SWNT at temperatures below 15 K, shown in figures 3.9 and 3.17 in sections 3.1 and 3.3. Unfortunately no explanation was given for the reduction in the EPR intensity in [152]. The intensity loss might be caused by microwave shielding of spins not taking part in Cooper pairing in the superconducting phase. Another cause of the EPR susceptibility decrease might be the formation of singlet Cooper pairs out of spins previously detected *via* EPR. In a recent report Stankowski *et al.* further analyzed the EPR properties of lightly alkali metal-doped C₆₀ [153]. Based on the MRR model of Micnas, Ranninger and Robaszkiewicz [154] a theoretical explanation is postulated in [153]: Spins of the C₆₀⁻ anion ($S = \frac{1}{2}$) form localized Cooper pairs with $S = 0$ at temperature T_p . Here, the su-

⁷The crossing of the transition temperature could also be supported by electromagnetic fluctuations.

perconducting gap of 2Δ opens well above the critical temperature. At T_c , however, these formerly incoherent Cooper pairs can undergo Bose-Einstein condensation (BEC), leading to superconductivity. This two-step model leads to an EPR temperature dependence very similar to the one observed in the present work. For $T > T_p$, an excessive intensity increase is detected when cooling the sample. At lower temperatures ($T < T_p$) the EPR susceptibility is reduced exponentially due to condensation into the singlet Bose-Einstein state.

In the most general case, the non-resonant microwave absorption in superconductors shows a strong power dependence. A minimum threshold power is required to allow for the observation of microwave absorption. This non-linearity arises from microwave-currents, which induce a stepwise breakdown of the superconductivity in Josephson-Junctions [155]. These Josephson-Junctions occur in specific areas of granular superconductors, such as defects, grain boundaries, and crystal twins. At higher microwave powers, overheating of the Josephson-Junction-network again can reduce the microwave absorption, if the dissipated power shifts the Junctions to the normal state [156]. In SWNT such Josephson-Junctions as normal state connections between two superconducting phases could be achieved by two possible configurations: (1) a contact area between two neighboring superconducting nanotubes or (2) a normal conducting or insulating division in one superconducting nanotube. The former is rather unlikely, because the SWNT sample under investigation is formed by a wide variation of tubes of different chiralities and therefore different electronic properties. However, as one nanotube is in contact with six tubes in the hexagonal pattern of a bundle, it might not be impossible. Additionally, the phase coherence between two superconducting tubes could be achieved over a longer distance than direct contact. The latter possibility of normal state sections in one superconducting tube is much more probable, because defects in the tube are anticipated to alter the electronic properties locally. Thus, the Cooper pair condensation might be perturbed in a specific segment of one superconducting SWNT, while the coherence between the two divided superconducting domains is preserved. The missing field dependence (up to 1 T) of the non-linear microwave absorption might be taken as evidence against the proposed superconductivity. However, little is known about superconductivity in 1D-systems, making a decision in favor or against superconductivity very difficult.

Electron interactions could also lead to other phenomena, such as a Coulomb blockade or a Mott-like metal-insulator transition. A Coulomb blockade in SWNT was proposed theoretically in 1997 [38] and has been reported experimentally only one year later by

Cobden *et al.* [157]. In contrast to this well investigated phenomenon, reports about metal-insulator transitions are sparse [158, 159]. Whereas Coulomb blockade, as well as the Fabry-Pérot resonance and the Kondo effect [46], are quantum dot effects, *i. e.*, transport effects in a single tube, a metal-insulator transition can be induced by intertube interaction or by a modulation of the SWNT band structure due to topological defects. The complexity of these effects impedes the theoretical analysis of a possible metal-insulator transition. The experimental analysis is hindered, too, because observations cannot be assigned unambiguously to a certain species in the bulk sample. Possible macroscopic manifestations of these electronic transitions in form of the effects observed in the present work require further regard.

Summary *Low-temperature non-linear microwave dissipation in SWNT was observed using cavity perturbation. Whereas all catalyst-free CVD grown nanotubes show a non-linear absorption at temperatures below 12 K, a control sample of arc-grown tubes using a Ni/Y catalyst shows a temperature invariant rather small Q . For a full control over all measurement parameters, a custom microwave bridge was constructed. By employing this bridge, the power and temperature dependence of the microwave absorption could be elucidated in detail. The results suggest that a minimum threshold power is needed to allow for non-linear microwave absorption. A trivial microwave heating can be neglected as a source for this phenomenon. The data can be reproduced accurately by a semi-empirical model, invoking a phase transition to a non-linear dissipative state at temperatures distributed around 7 K. Several reasons for this low-temperature state have been discussed, including superconductivity, as well as other correlated electronic effects.*

3.4.3 Microwave dispersion

As was already stated in section 3.4.2, energy dissipation, *i. e.*, the absorption of electromagnetic radiation, is always accompanied by dispersion. This follows from the Kramers-Kronig relation [160, 161]. The dispersion can be measured as a shift in the resonance frequency of the loaded cavity. To elucidate the non-linear dissipation properties in SWNT samples, the resonance frequency of the SWNT-loaded microwave cavity was tracked at different temperatures and microwave power levels. Any non-linearity can be identified as a power dependence of the resonance frequency.

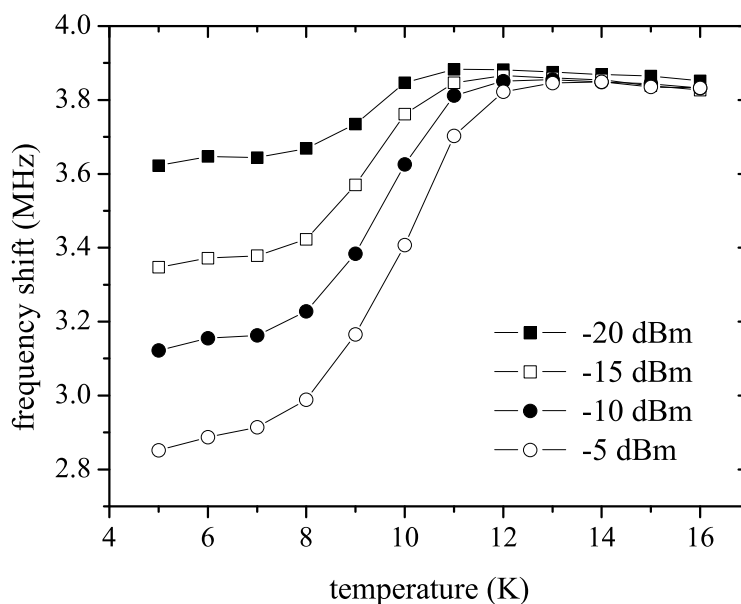


Figure 3.27: Temperature dependence of the frequency shift of the SWNT-loaded microwave cavity relative to the cavity loaded with an empty sample tube for different microwave power levels. The connection lines between data points should serve only as guides to the eyes. For details see text.

Because it was not possible to determine the resonance frequency with the setup used for accurate absorption measurements, a different experimental method had to be applied. The microwave bridge of the commercial ElexSys E680 was used in the “operate” mode. By the automatic frequency control (AFC) unit the microwave source had been locked to the resonance frequency of the cavity. The frequency readout was done by the built-in frequency counter. The resonator was operated totally undercoupled in order to exclude any frequency variation by a changing microwave coupling of the resonator. The helium pressure in the cryostat was kept constant in all experiments to avoid any influence on the resonance frequency. It was mandatory to correct the frequency data as the probehead loaded with an empty sample tube already showed a temperature dependence of the resonance frequency. This was performed by subtracting the resonance frequency of the sample-loaded cavity from one loaded only with an empty evacuated EPR tube. These corrected frequency differences are plotted in figure 3.27 as a function of the temperature for different incident microwave power levels. It should be noted that the frequency in the empty cavity in the observed temperature region varied monotonously by up to 530 kHz without showing any power dependence. As a drawback of the setup used, the frequency-lock is only stable in a rather narrow power range. This boundary limits the measurement

of the resonance frequency to microwave power levels between -20 and -5 dBm. It is noteworthy that the microwave power falls below the optimum AFC working range at the minimum power of -20 dBm. Therefore the frequency at this low power level is slightly shifted by approximately 20 to 30 kHz with respect to the intrinsic resonance frequency of the cavity. In figure 3.27 this can be seen at the high-temperature limit. This effect, however, is small compared to the apparent non-linear frequency shift which sets in at temperatures of 12 K and below. This non-linearity shows the same characteristics as observed for the microwave absorption behavior. The power dependence of the frequency shift is easy to identify with a clear temperature onset. At temperatures below 7 K the change in the frequency shift with varying temperature is minimal. Thus it can be assumed that the low-temperature electromagnetic state is fully reached. Finally it should be noted, that a cross-comparison between the power levels used in the dispersion measurements in this paragraph and the absorption measurements in the preceding section is impossible. This is a result of the completely different experimental situations. For dispersion measurements the microwave frequency was locked statically to the resonance frequency. The microwave frequency in the case of absorption measurements, however, was swept rapidly in order to scan for the absorption mode of the microwave resonator. The microwave coupling of the resonator differs in both techniques, too, *i. e.*, undercoupling in the case of dispersion experiments *vs.* critical coupling in the case of dissipation measurements.

At first sight, the sign of the relative frequency shift at temperatures below 12 K might be counter-intuitive. The expected Meissner phase inside the cavity would expel the microwave field and thus reduce the effective cavity volume. This would result in a higher resonance frequency. However, as already stated earlier, the formation of a perfect Meissner phase is not really compulsory due to the small dimensions of the superconducting domains. Therefore inductive loading with Cooper pairs can account for the observed reduction of the resonance frequency as long as the microwave field can penetrate the formed superconducting domains [162].

Together with these dispersion measurements it was possible to quantitatively track the time-dependence of the non-linear microwave absorption after rapidly changing the incident power. This analysis was not applicable in the case of the experiments to determine the Q factor, because following the change in Q with a time resolution of 10 s was not possible. The time dependence of the resonance frequency in the present experiment, however, could be recorded with sufficient time resolution after stepwise raising

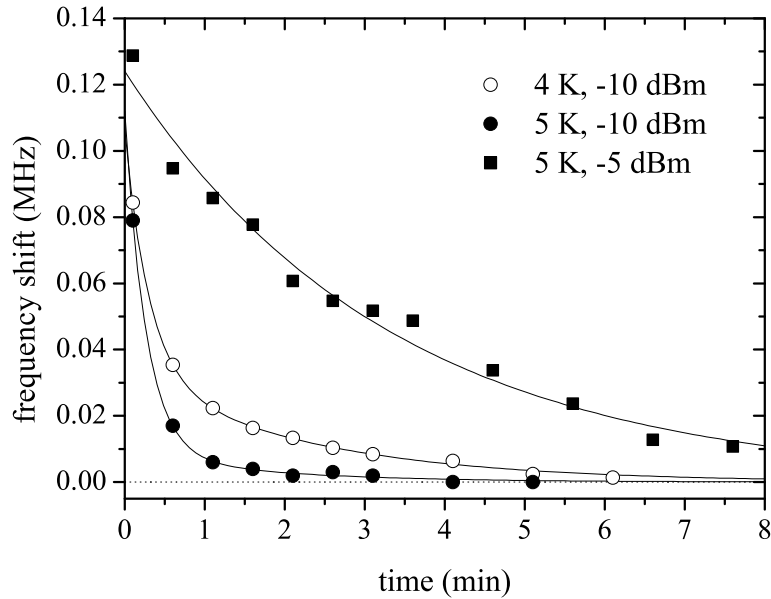


Figure 3.28: Time-dependence of the resonance frequency of the TE_{011} -resonator loaded with SWNT after switching to a higher microwave power. The experimental data were fitted with mono- or biexponential functions to give guides to the eyes.

the microwave power. This choice allows for an indirect measurement of the Q creeping after an abrupt change of the microwave power. All observed frequency variations are fully reversible. At the lowest temperatures of 4 or 5 K this phenomenon takes place in a time-scale of several minutes. At slightly higher temperatures of 7 to 8 K this effect is significantly faster, being in the time scale of a few seconds. At still higher temperatures the final state is reached almost instantaneously. Therefore reliable data could be taken only at temperatures of 4 and 5 K. Care was taken that the system was in thermal as well as in electromagnetic equilibrium before changing the microwave power. Due to the limited operating range of the microwave diode and of the AFC, microwave power levels were restricted to -5 and -10 dBm at 5 K and to -10 dBm at 4 K. The experiment was initiated by increasing the incident microwave power by 5 dB. The frequency recording was started as soon as possible. The record of the first frequency point was chosen as time zero in figure 3.28. In this graph, experimental data points were fitted with mono- or biexponential functions to give guides to the eyes. The absolute resonance frequency was converted into relative frequency shifts by subtracting the final equilibrium value, which was partly extrapolated by the exponential fits.

It can be seen clearly that even after 8 minutes the equilibrium value is yet not reached when choosing $T = 5$ K and a microwave power level of -5 dBm. At a power level of -10 dBm the final frequency is reached in a fraction of this time. At 4 K and -10 dBm the time-scale is significantly slower, but still much faster than at an incident power level that is higher. This confirms the qualitative observation of slower creeping at lower temperature and higher incident microwave power. It should be noted, however, that the relative shifts which could be recorded in this experiment, cover less than 50 % of the total frequency shifts measured in the corresponding equilibrium states, respectively. This indicates that the largest amount of the dissipation change occurs at a very short time-scale of a few seconds, which cannot be resolved with this type of experiment.

According to the Kramers-Kronig relation the recorded resonance frequency shift confirms the earlier detected non-linear absorption. The observed frequency and power dependencies perfectly match the findings of the microwave dissipation experiments. The observed “creeping” behavior of the non-linear microwave absorption upon a fast change in the microwave power had been formerly detected only qualitatively by a Q creep. By exploitation of the recorded time dependence, this behavior could be quantified. In the model of a transition to a superconducting state, the creeping can be explained by a slow flux creep. Whereas at small magnetic fields fluxons can move in a Josephson-Junction network, Abrikosov vortices can form in the Shubnikov phase of a type-II superconductor at higher fields. Both types of fluxon motion can lead to a non-linear dissipation [163]. When rapidly increasing microwave power above the threshold field amplitude, the magnetic flux will slowly creep into the superconducting phase. Final outcome is the observed creeping to an equilibrium state.

Summary *By recording the resonance frequency of a microwave cavity, it was possible to detect the expected frequency shift in the low-temperature dissipative state of SWNT as a function of temperature and microwave power. It could be shown that for $T > 12$ K, i. e., above the transition to the non-linear state, the resonance frequency shows no power dependence and practically no variation with temperature. However, when entering the temperature region at which the non-linear absorption takes place, a shift to a smaller resonance frequency occurs. The magnitude of this shift strongly depends on the incident microwave power. Additionally, a “creeping” behavior of the resonance frequency was observed when abruptly changing the microwave power at low temperatures. This creeping is only detectable at the lowest temperatures considered, i. e., at 4 and 5 K. It is faster at higher temperatures and at lower microwave power. According to the previous*

introduction of a possible superconducting transition as explanation for the non-linear loss behavior, the negative frequency shift in the low-temperature state is explained by an inductive loading of the cavity when forming Cooper pairs. The creeping behavior, on the other hand, indicates a slow flux creep in the Shubnikov phase of a type-II superconductor.

3.5 Magnetization

3.5.1 DC magnetization at high fields

As was shown in the preceding chapters, SWNT undergo certain, not fully characterized electronic or magnetic transitions. Whereas EPR can selectively probe the different magnetic components in the field domain, magnetization measurements reveal the overall magnetic properties of the sample. During a SQUID direct current (DC) magnetization experiment, the sample is moved through a pair of superconducting rings in a static external magnetic field. The magnetic moments of the sample induce electric currents which are sensed by Josephson-Junctions between the superconducting parts of the rings. Therefore the sensitivity of such an experiment depends strongly on the external field strength. Ideally the sample should be point-like, allowing for a good fit of the induced current curve for a determination of the sample magnetization. As the bulk density of the SWNT is very low, a rather extended powder sample of 20 mm height – confined by two swaps of cotton wool in a vacuum sealed EPR sample tube with 4 mm outer diameter – was required in order to obtain a sample mass of 6 mg. This amount of sample was mandatory to obtain a sufficient signal to noise ratio. The large spatial extension of the sample, however, necessitated the development of a special fitting algorithm to derive reliable magnetization data.

The DC magnetization was measured at a rather low field strength of 5 kOe and additionally at a high field strength of 70 kOe. Magnetization data are shown in figure 3.29 as mass magnetization after the subtraction of a constant, temperature independent component. This correction excludes the determination of any diamagnetic or Pauli-paramagnetic contribution. As the data points recorded at 5 kOe external field strength can be described quite well by the Curie law, the magnetization at 70 kOe does not follow that $\frac{1}{T}$ -dependence. That is not surprising, because Curie's law is only valid in the high-temperature–low-field regime. A general description of the magnetization M cov-

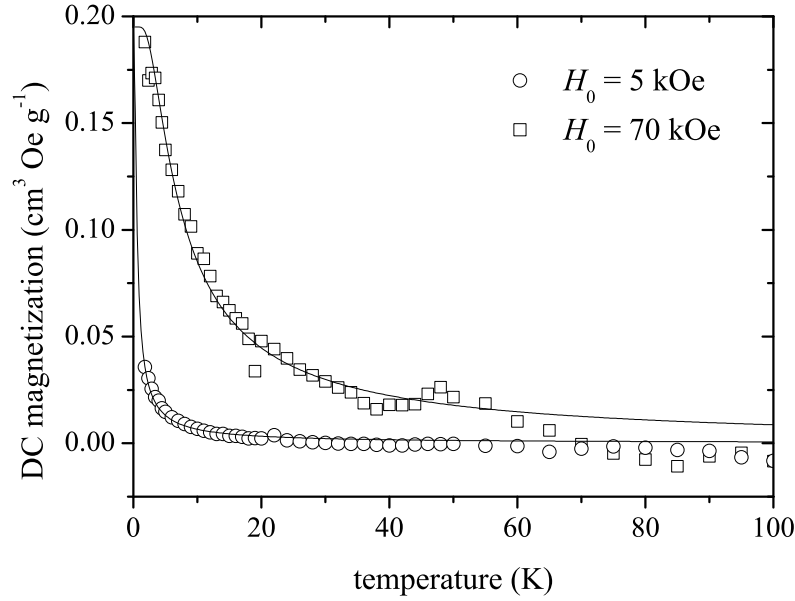


Figure 3.29: Magnetization of a CVD SWNT sample with a mean diameter of 2.5 nm at an external magnetic field strength of 5 kOe (circles) and 70 kOe (squares). Both solid lines represent one single-parameter fit with a Brillouin-function for the respective field strengths according to equation (3.17). For details see text.

ering the high-field or low-temperature range is obtained by incorporating the Brillouin function $B_{\frac{1}{2}}$ for a $J = S = \frac{1}{2}$ system:

$$M = Ng\mu_B \frac{1}{2} B_{\frac{1}{2}}, \quad (3.17a)$$

with

$$B_{\frac{1}{2}} = 2 \coth\left(\frac{g\mu_B H_0}{k_B T}\right) - \coth\left(\frac{g\mu_B H_0}{2k_B T}\right). \quad (3.17b)$$

g represents the Landé g factor; μ_B and k_B have their usual meanings. N denotes the number of paramagnetic centers in the sample. The restriction to a simple $S = \frac{1}{2}$ system is tentative. As can be seen in figure 3.29, when using $S = \frac{1}{2}$ both data sets can be fitted with only one common fitting parameter $N = 2.1 \times 10^{19} \text{ g}^{-1}$ or 4.2×10^{-4} spins per carbon atom. This number can be translated into a low-field Curie susceptibility of $\chi_C T = 1.3 \times 10^{-5} \text{ cm}^3 \text{ K g}^{-1}$. This value can directly be compared with the EPR derived values, obtained either *via* spin counting or *via* spectral analysis (see sections 3.1.4 and 3.2.1).

The corresponding EPR experiments (*i. e.*, spin counting and spectral analysis) yielded values of 1.2×10^{-4} and 3.4×10^{-4} spins per carbon atom. Regarding the relatively high uncertainty of the EPR susceptibility value, an unambiguous decision cannot be made, if the total magnetization has been observed by EPR spectroscopy, or if the larger part of the magnetization was not detected by EPR. However, the non-ideal EPR intensities of various signals in different temperature regimes seem to suggest, that the observed EPR signals are interconverting into each other. Additionally the microwave field at the spins' positions might be reduced locally at low temperatures. The latter explanation is furthermore supported by EPR experiments using transient nutation experiments (see section 3.2.3) and N@C₆₀ as inert spin probe (see section 3.3). The lower number of spins detected by EPR spectroscopy at $T = 20$ K could indicate, that not all spins have been converted into the detected signal before the signal intensity drops due to microwave shielding at even lower temperatures.

Summary *DC magnetization measurements at magnetic field strengths of 5 and 70 kOe revealed a paramagnetic behavior. By using a Brillouin function for a $J = S = \frac{1}{2}$ system, both data sets could be fitted consistently, yielding a number of 4.2×10^{-4} spins per carbon atom. This value is in good agreement with spin concentrations derived by EPR spectroscopy. The variety of different signals detected by EPR together with their non-Curie-like temperature dependence suggest an interconversion between these signals. Furthermore the observation that the magnetization perfectly follows a Brillouin function even at the lowest temperature of 1.8 K, supports the model of a microwave shielding at low temperatures as was deduced by an analysis of c. w. and pulsed EPR and transient nutation experiments.*

3.5.2 AC magnetization at low fields

Alternating current (AC) magnetization measurements have been performed at low fields. In contrast to the DC magnetization measurements, the sample is spatially fixed between the superconducting ring pair while the magnetic field is oscillating. The periodical change of the magnetization with respect to the external field strength is sensed. If the AC field strength amplitude is small, this results in a direct measurement of the sample's susceptibility. As the in-phase as well as the out-of-phase component is detected, the complex susceptibility is obtained.

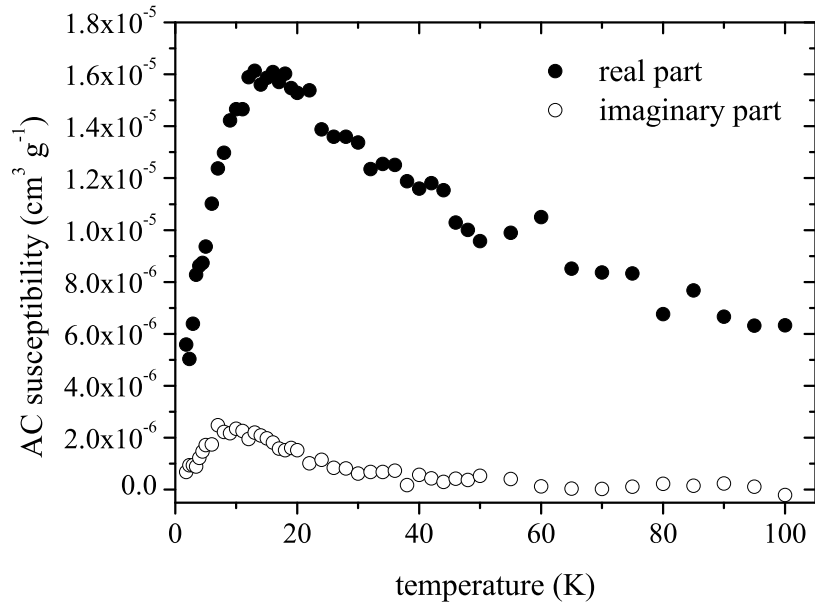


Figure 3.30: Complex AC susceptibility of the SWNT sample at zero external biasing field, recorded with an AC amplitude of 5.5 Oe and a frequency of 100 Hz.

In figure 3.30 the complex susceptibility is plotted at zero offset field. The AC amplitude was 5.5 Oe at a modulation frequency of 100 Hz. To ensure that the relatively high amplitude of 5.5 Oe did not distort the measured susceptibility, experiments were also performed using a lower field modulation. A perfect linear relation was observed up to 5.5 Oe. From 100 down to 20 K the susceptibility increases significantly, but does not follow a Curie law. Even more surprising, below 20 K it shows a sharp drop down to the lowest measured temperature of 1.8 K. Here it is even less than the susceptibility at 100 K. The drop in the sample susceptibility is accompanied by a rather small contribution of the imaginary part of the susceptibility, indicating the occurrence of a magnetic phase transition in the sample.

At first sight the measured AC susceptibility seems to be at variance with the earlier measured DC magnetization, which exhibited a trivial paramagnetic behavior. If one compares both data sets quantitatively, the paramagnetic contribution does not contradict the AC susceptibility data. This can be seen in figure 3.31. Here, both data sets are compared using the same scale. This is accomplished by generating the DC susceptibility from the $H_0 = 5$ kOe magnetization data under the eligible assumption of linear magnetization curves. Only at the lowest measured temperature the trivial paramagnetism is close to the zero-field AC susceptibility. At higher temperatures the paramagnetic susceptibil-

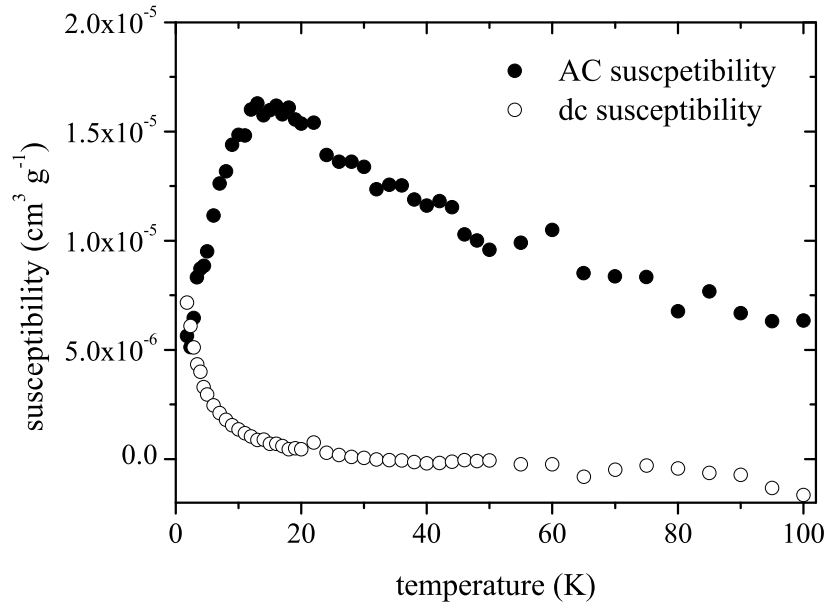


Figure 3.31: Comparison of the AC (absolute value) and DC susceptibility of the SWNT sample at zero external biasing field. The DC susceptibility was obtained from the DC magnetization at $H_0 = 5$ kOe, assuming perfectly linear magnetization curves.

ity is at least one order of magnitude smaller. This issue explains why the previously derived paramagnetism is not detectable directly with zero-field AC susceptibility measurements. It does not explain, however, why the DC magnetization experiments do not show any sign of the susceptibility anomaly observed in the AC experiment.

Although the drop in the AC susceptibility emerges at a comparable temperature at which the phase transition to the non-linear dissipative state occurs (which was detected *via* microwave absorption experiments in section 3.4), a direct connection between the two observations is not compulsory and cannot be confirmed. A rigorous fact that seems to exclude one effect as the reason for both experimental findings is a strong dependence of the AC susceptibility on the external field strength; see figure 3.32. A comparable field dependence was never observed in the case of non-resonant microwave absorption. The AC susceptibility strongly decreases when an external biasing field is present. Additionally, the temperature defining the maximum of the AC susceptibility is shifted to higher temperatures for an increasing external field strength.

As the AC susceptibility is a measure for the change of the magnetization with a variation in the magnetic field strength, mathematical integration of the susceptibility with respect to the external field strength yields the absolute magnetization of the sample. On

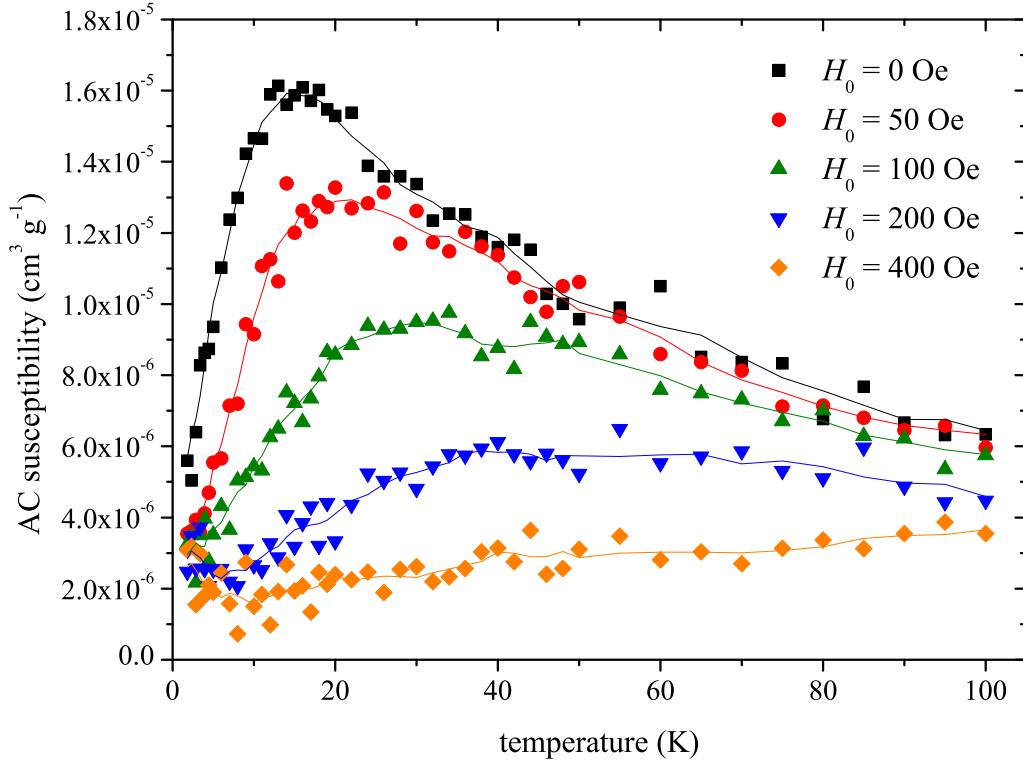


Figure 3.32: AC susceptibility of the SWNT sample at different external biasing field strengths, recorded at an AC amplitude of 5.5 Oe and a frequency of 100 Hz. The solid lines have been obtained by smoothing the experimental data and should serve only as guides to the eyes.

the left side in figure 3.33 the field strength dependence of the AC susceptibility is shown at a temperature of 20 K, at which the AC susceptibility peaks at zero external field strength; on the right side of this figure, the resulting magnetization is plotted. The magnetization curve shows a typical saturation behavior with a strong magnetization buildup at small field strengths and flattening at higher fields. The flattening occurs already at rather small field strengths of a few hundred Oe. Despite a thorough search, no indication of hysteresis or field cooling effect could be detected.

To derive the saturation magnetization, a simple exponential saturation model was evoked. Additionally a paramagnetic component following Curie's law was allowed, resulting in the following fitting equation:

$$M(H_0) = M_{\text{sat}} \left(1 - \exp \left(-\frac{H_0}{b} \right) \right) + \chi_C H_0. \quad (3.18)$$

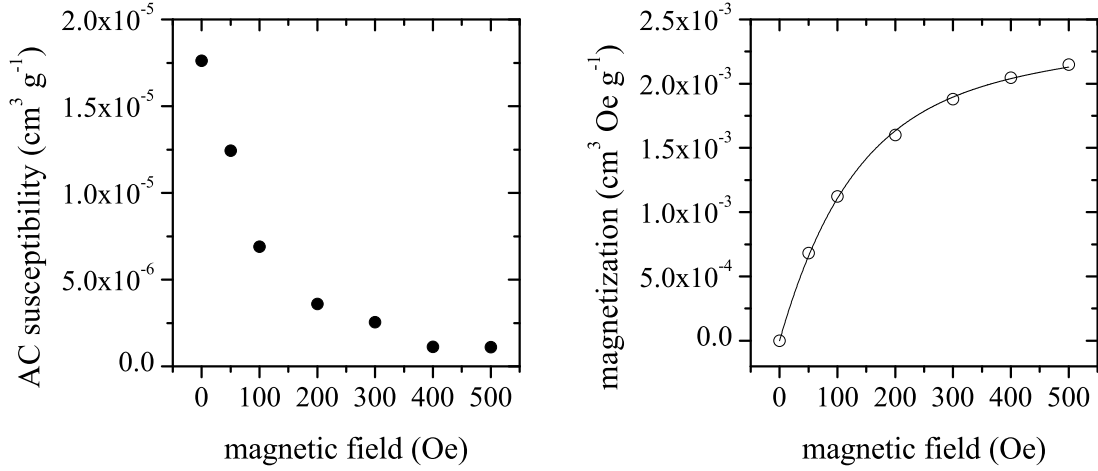


Figure 3.33: Left: AC susceptibility of the SWNT sample as a function of the external biasing field strength. Data were taken at a temperature of 20 K. Right: sample magnetization derived *via* a numerical integration of the AC susceptibility data with respect to the external field strength. The solid line represents a fitting curve using equation (3.18). For details see text.

The fit yields a saturation magnetization of $1.94(2) \times 10^{-3} \text{ cm}^3 \text{ Oe g}^{-1}$, the field strength constant b is determined as 126(4) Oe. In this fitting model, the Curie susceptibility was taken from the DC magnetization measurements at 5 kOe in figure 3.31 as $4.5 \times 10^{-7} \text{ cm}^3 \text{ g}^{-1}$. In a fit conceding all degrees of freedom, the saturation magnetization yields a value of $1.7(1) \times 10^{-3} \text{ cm}^3 \text{ Oe g}^{-1}$, being around 10 % smaller than the above stated one. The fitted Curie susceptibility amounts to $1.0(2) \times 10^{-6} \text{ cm}^3 \text{ g}^{-1}$ and the field strength constant is determined as 106(5) Oe. Considering that no restrictions to fit the parameters were enforced, the uncertainty of experimental data, and the additional data processing, the agreement is quite satisfying. Thus the simple model applied seems to be justified. The magnitude of the saturation magnetization of $1.94(2) \times 10^{-3} \text{ cm}^3 \text{ Oe g}^{-1}$ can be translated into a number of Bohr magnetons in the sample using

$$M_{\text{sat}} = NgJ\mu_{\text{B}}, \quad (3.19)$$

yielding $2.09(2) \times 10^{17} \mu_{\text{B}} \text{ g}^{-1}$ or $4.17(4) \times 10^{-6} \mu_{\text{B}}$ per carbon atom.

The saturation behavior is typical for cooperative magnetism, *i. e.*, ferromagnetism. The rather small saturation field strength of 126 Oe indicates only weak ferromagnetism. The relatively low saturation magnetization of only $4.17(4) \times 10^{-6} \mu_{\text{B}}$ per carbon atom proves that only a very small part of the sample undergoes the transition to an ordered

magnetic state. The number of spin centers depends on the g value and the spin state, which cannot be deduced unambiguously by the performed experiments. It can only be stated that the number is limited to a maximum of $8.34(8) \times 10^{-6}$ spins per carbon atom assuming the unrealistic case of $g = 1$. However, it is more realistic that it is at least two orders of magnitude smaller than the number of Curie-like paramagnetic centers deduced *via* DC magnetization (see section 3.5.1) and EPR spectroscopy (see sections 3.1.4 and 3.2.1). At first sight it might be quite surprising, that no indication of this well pronounced AC anomaly is observed in the DC magnetization experiments. However, due to the low magnitude of the cooperative magnetism, as well as the rather low saturation field strength, the $S = \frac{1}{2}$ paramagnetism overwhelms this small effect at high fields.

The content of the residual Fe catalyst was determined as high as 130 ppm (weight) or 28 ppm (atom) in the very early age of the “Super-Growth” technique [96]. Considering the very low magnitude of cooperative magnetism, the iron catalyst might be one possible source of this phenomenon. Regarding a maximum spin state of $J = S = 2$ and typical g value of 2, the content of the iron catalyst in the present sample would be in the range of 1 to 4 ppm (atom). This seems a reasonable value when considering the progress and the improvement in the production method. However, the very low saturation field strength ($H_{\text{sat}} = 126$ Oe) seems to contradict iron ferromagnetism. As the catalyst consists of nanosized particles, the formation of ferromagnetism is unexpected. Note that the particle size is smaller as the ferromagnetic domain size. Thus, superparamagnetism is more likely in this material, giving rise to a totally different saturation field strength which is a function of the particle size. This saturation field is expected to be in the order of several teslas. On the other hand, the fact, that no sign of an Fe signal was observed in EPR experiments, is a striking argument against a residual catalyst as the source of the observed magnetism.

As was already pointed out in section 1.4, various reports on cooperative magnetism in carbon nanotubes have been published. Most of them are based on theoretical considerations. Rode *et al.* suggest that the observed ferromagnetism in carbon nanofoam is induced by metallic domains separated from each other by non-metallic regions. This might also be the case for a SWNT bulk sample, as metallic tubes exist in an array of semiconducting tubes. After all, the results in sections 3.1 and 3.4 have experimentally confirmed the existence of both types of SWNT in the present sample. Other possible sources of magnetism in SWNT are carrier doping, vacancies, line-defects, or edge

states. However, the true source of the observed ferromagnetism cannot be elucidated on the basis of the current state of research.

The fact that both non-linear microwave absorption and ferromagnetism occur at a similar temperature range does not imply that both effects are coupled with each other. The possible coexistence of superconductivity and ferromagnetism in different tubes seems possible, as the tubes in one bulk sample differ in their electronic configurations. Recent experiments have shown that superconductivity and magnetism can coexist in one crystal of $\text{RuSr}_2\text{GdCu}_2\text{O}_8$ without precluding each other. It is only necessary that the RuO_2 and CuO_2 planes of this material are effectively decoupled [164].

Summary *At low magnetic field strengths, a ferromagnetic behavior is observed in SWNT. The ferromagnetism in this sample differs strongly from the conventional magnetism in iron. It is assumed that the latter is still present as traces in the nanotube samples. The very low saturation field strength of 126 Oe indicates only a very weak magnetism. Only a very small part of the bulk sample participates in the cooperative magnetism, which is derived by the also very low saturation magnetization ($M_{\text{sat}} = 4.17(4) \times 10^{-6} \mu_{\text{B}}$ per carbon atom). In addition to the rather unlikely possibility of residual nano-sized Fe catalyst being responsible for magnetic response, several mechanisms of magnetism in carbon-only materials have been suggested as possible sources of the observed effect.*

4 Summary and conclusion

In this study it was shown that “Super-Growth” CVD grown SWNT offer significantly more insight into the electronic and magnetic properties of SWNT than samples produced by conventional techniques. The latter suffer from a high amount of residual catalyst. This peculiarity of the formerly mentioned class of SWNT is explained by the absence of any signal of the magnetic catalyst both in the EPR and in the magnetization measurements. As a consequence, the intrinsic features could be examined, which – up to now – have been masked by a spurious amount of the ferromagnetic metallic catalyst.

The room-temperature EPR spectra are characterized by a relatively complicated convolution of different signals. However, as these signals differ in their behavior upon temperature variation they can be correlated qualitatively with the different electronic species in the SWNT samples. At least three distinct resonance lines can be observed, whose relative signal intensities vary between different production batches. Two of the signals are located at $g = 2.00$, which refers to the g factor of a free electron. The third line is shifted to a lower resonance field. The effective g value of 2.07 is significantly larger than values realized for the conduction electrons in graphite. This could be explained by a rather strong spin-orbit coupling in SWNT. Whereas the orbital momentum of the electrons in carbon systems is normally quenched, this condition is partially lifted in SWNT due to circular components of the electronic wave functions around the tube circumference. The recorded EPR line can be fitted in a spectral deconvolution by three symmetric Lorentz lines of varying resonance fields and line widths. The convoluted fit shows a very good agreement with the experimental findings. One of the three components shows a temperature-activated behavior with an activation energy of $E_a = 85$ meV. This finding is interpreted either by semiconducting tubes with a band gap in the order of the experimental activation energy, or by the existence of shallow defect states in semiconducting tubes with a larger band gap. At these temperatures, the charge carriers are promoted to the conduction band. The remaining two components do not reveal a significant temperature dependence in the observed temperature range. This is an indication for metallic or at least pseudo-metallic nanotubes. These pseudo-metallic SWNT possess a narrow band gap which is significantly smaller than $k_B T$ at room temperature.

In addition, by using non-resonant microwave absorption, the existence of SWNT with an energy gap of 7 meV was observed. This value is in full agreement with predicted curvature-induced energy gaps in pseudo-metallic SWNT and further supports the above assignment of the EPR spectral components.

At $g = 2.00$ two different signals can be discriminated by line width. The narrow signal is attributed to defects localized on SWNT. It shows an unproportional gain in intensity at lower temperatures. Additionally a small g anisotropy could be revealed ($\Delta g = 1 \times 10^{-3}$) which is explained by a shielding of the magnetic field. The shielding is caused by the tubular structure of SWNT. The broader signal is totally depleted if molecular oxygen is present in the sample tube. This observation is explained by a weak interaction of triplet oxygen with the electron spins. At temperatures between 160 and 20 K, a possible conversion of this broader line to the narrow signal is observed, which could be explained by a delocalization of defect states. The rather constant line width of the narrow signal excludes a continuous broadening mechanism. Our observation is further supported by pulsed EPR experiments. Only the narrow spin component could be refocused to form a spin echo. The constant and rather long spin dephasing time of $T_2 = 32 \mu\text{s}$ is in agreement with the above explanation. Although the signal shows a strong dependence of the EPR intensity upon temperature variation, direct current (DC) magnetization proves a perfect paramagnetic behavior of the sample in medium to high field strengths. Both DC magnetization and EPR spin counting yielded spin concentrations in the order of 10^{-4} spins per carbon.

At very low temperatures – *i. e.*, $T < 15$ K – a dramatic drop in the EPR intensity occurs. Microwave saturation as well as sample heating due to microwave irradiation could be excluded as trivial sources of this effect. Therefore only a change in the electronic properties of the SWNT is an acceptable explanation. Non-resonant microwave absorption revealed a non-linear dissipative state at these low temperatures. This state shows a clear signature of a power dependence of the microwave absorption. Additionally a threshold power which is required to trigger any non-linear absorption was observed. The transition between a non-linear dissipative state at low temperatures and a conventional Ohmic loss state is introduced as a phenomenological model. A rather broad transition with a mean transition temperature $T = 7$ K is used to describe the experimental data. Additionally, frequency dispersion measurements in the low-temperature state revealed a rather slow creeping process in the time-scale of minutes. The nature of the non-linear dissipation is somewhat unclear. The possibility of the transition to a superconducting

state, however, has been discussed already in the literature and has been proven experimentally, too. Although the observed non-linear power loss shows strong similarities to the microwave absorption in granular superconductors, the absence of any magnetic-field dependence seems to contradict this explanation.

Alternating current (AC) magnetization experiments at zero and low magnetic field strength revealed a weak ferromagnetism with a saturation magnetization of $M_{\text{sat}} = 4.2 \times 10^{-6} \mu_{\text{B}}$ per carbon atom. Due to the low magnetization and the very low saturation field strength of only 126 Oe, this magnetic phase does not play a significant role in the high field magnetic properties. Iron was discussed as the source of this effect. However, the observed properties seem to contradict this trivial explanation. As a result, the observed cooperative magnetism is regarded as an intrinsic property of SWNT. This is an important observation, as it is believed that long-range spin ordering is incompatible with a bare carbon compound. However, recent experiments have shown, that magnetic phases in pure carbon systems can exist. Recent theoretical calculations have predicted this behavior also for SWNT.

The present EPR and non-resonant microwave absorption study of an SWNT bulk sample has revealed clear signatures of metallic, pseudo-metallic, and semiconducting nanotubes. In addition, several unexpected characteristics have been observed at low temperature, *i. e.*, the transition to a non-linear dissipative state as well as weak ferromagnetism. These properties cannot be assigned unambiguously to certain electronic types of carbon nanotubes or specific interactions of tubes. Therefore, SWNT samples consisting of only one specific type of nanotubes, *i. e.*, semiconducting or metallic ones, or even of one specific chirality, are highly demanded for further examination using the introduced methods.

Appendix

References

- [1] P. W. Atkins, *Physikalische Chemie* (VCH, Weinheim, 1996), 2nd edn.
- [2] U. Müller, *Anorganische Strukturchemie* (B. G. Teubner Verlag, 1996), 3rd edn.
- [3] K. S. Novoselov, A. K. Geim, S. V. Morozov, D. Jiang, Y. Zhang, S. V. Dubonos, I. V. Grigorieva, A. A. Firsov, *Science* **306**, 666 (2004).
- [4] K. S. Novoselov, A. K. Geim, S. V. Morozov, D. Jiang, M. I. Katsnelson, I. V. Grigorieva, S. V. Dubonos, A. A. Firsov, *Nature* **438**, 197 (2005).
- [5] H. W. Kroto, J. R. Heath, S. C. O'Brien, R. F. Curl, R. E. Smalley, *Nature* **318**, 162 (1985).
- [6] W. Krätschmer, K. Fostiropoulos, D. R. Huffman, *Chem. Phys. Lett.* **170**, 167 (1990).
- [7] W. Krätschmer, L. D. Lamb, K. Fostiropoulos, D. R. Huffman, *Nature* **347**, 354 (1990).
- [8] R. Taylor, J. P. Hare, A. K. Abdul-Sada, H. W. Kroto, *J. Chem. Soc., Chem. Commun.* pp. 1423–1425 (1990).
- [9] K. Hedberg, L. Hedberg, D. S. Bethune, C. A. Brown, H. C. Dorn, R. D. Johnson, M. de Vries, *Science* **254**, 410 (1991).
- [10] J. R. Heath, S. C. O'Brien, Q. Zhang, Y. Liu, R. F. Curl, F. K. Tittel, R. E. Smalley, *J. Am. Chem. Soc.* **107**, 7779 (1985).
- [11] Y. Chai, T. Guo, C. Jin, R. E. Haufler, L. P. F. Chibante, J. Fure, L. Wang, J. M. Alford, R. E. Smalley, *J. Phys. Chem.* **95**, 7564 (1991).
- [12] T. Kato, S. Suzuki, K. Kikuchi, Y. Achiba, *J. Phys Chem.* **97**, 13425 (1993).
- [13] T. Weiske, D. K. Böhme, J. Hrušák, W. Krätschmer, H. Schwarz, *Angew. Chem. Int. Ed. Engl.* **30**, 884 (1991).
- [14] M. Saunders, H. A. Jiménez-Vázquez, R. J. Cross, R. J. Poreda, *Science* **259**, 1428 (1993).
- [15] M. Saunders, H. A. Jiménez-Vázquez, R. J. Cross, S. Mroczkowski, M. L. Gross, D. E. Giblin, R. J. Poreda, *J. Am. Chem. Soc.* **116**, 2193 (1994).

- [16] T. Almeida Murphy, T. Pawlik, A. Weidinger, M. Höhne, R. Alcalá, J.-M. Spaeth, *Phys. Rev. Lett.* **77**, 1075 (1996).
- [17] B. Pietzak, *Fullerenes as Chemical Atom Traps for Nitrogen and Phosphorus*, Ph.D. thesis, Technische Universität Berlin (1998).
- [18] J. C. Greer, *Chem. Phys. Lett.* **326**, 567 (2000).
- [19] S. Iijima, *Nature* **354**, 56 (1991).
- [20] L. V. Radushkevich, V. M. Lukyanovich, *Zurn. Fisic. Chim.* **26**, 88 (1952).
- [21] M. Monthieux, V. L. Kuznetsov, *Carbon* **44**, 1621 (2006).
- [22] M. S. Dresselhaus, G. Dresselhaus, R. Saito, *Phys. Rev. B* **45**, 6234 (1992).
- [23] R. Saito, M. Fujita, G. Dresselhaus, M. S. Dresselhaus, *Phys. Rev. B* **46**, 1804 (1992).
- [24] R. Saito, M. Fujita, G. Dresselhaus, M. S. Dresselhaus, *Appl. Phys. Lett.* **60**, 2204 (1992).
- [25] S. Iijima, T. Ichihashi, *Nature* **363**, 603 (1993).
- [26] D. S. Bethune, C. H. Kiang, M. S. de Vries, G. Gorman, R. Savoy, J. Vazquez, R. Beyers, *Nature* **363**, 605 (1993).
- [27] S. Saito, A. Oshiyama, *Phys. Rev. Lett.* **66**, 2637 (1991).
- [28] T. Guo, P. Nikolaev, A. G. Rinzler, D. Tomanek, D. T. Colbert, R. E. Smalley, *J. Phys. Chem.* **99**, 10694 (1995).
- [29] A. Thess, R. Lee, P. Nikolaev, H. Dai, P. Petit, J. Robert, C. Xu, Y. H. Lee, S. G. Kim, A. G. Rinzler, D. T. Colbert, G. E. Scuseria, D. Tománek, J. E. Fischer, R. E. Smalley, *Science* **273**, 483 (1996).
- [30] W. K. Maser, E. Muñoz, A. M. Benito, M. T. Martínez, G. F. De la Fuente, Y. Maniette, E. Anglaret, J.-L. Sauvajol, *Chem. Phys. Lett.* **292**, 587 (1998).
- [31] H. Dai, A. G. Rinzler, P. Nikolaev, A. Thess, D. T. Colbert, R. E. Smalley, *Chem. Phys. Lett.* **260**, 471 (1996).
- [32] J.-F. Colomer, C. Stephan, Lefrant, G. Van Tendeloo, I. Willems, Z. Kónya, A. Fonseca, C. Laurent, J. B. Nagy, *Chem. Phys. Lett.* **317**, 83 (2000).
- [33] J. T. Frey, D. J. Doren, *Tubegen 3.2*, University of Delaware, Newark (2003).
- [34] N. Hamada, S.-i. Sawada, A. Oshiyama, *Phys. Rev. Lett.* **68**, 1579 (1992).

- [35] C. L. Kane, E. J. Mele, *Phys. Rev. Lett.* **78**, 1932 (1997).
- [36] P. Delaney, H. J. Choi, J. Ihm, S. G. Louie, M. L. Cohen, *Nature* **391**, 466 (1998).
- [37] M. Ouyang, J.-L. Huang, C. L. Cheung, C. M. Lieber, *Science* **292**, 702 (2001).
- [38] C. Kane, L. Balents, M. P. A. Fisher, *Phys. Rev. Lett.* **79**, 5086 (1997).
- [39] M. Bockrath, D. H. Cobden, J. Lu, A. G. Rinzler, R. E. Smalley, L. Balents, P. L. McEuen, *Nature* **397**, 598 (1999).
- [40] A. De Martino, R. Egger, F. Murphy-Armando, K. Hallberg, *J. Phys.: Condens. Matter* **16**, S1437 (2004).
- [41] S. Frank, P. Poncharal, Z. L. Wang, W. A. de Heer, *Science* **280**, 1744 (1998).
- [42] K. Tsukagoshi, B. W. Alphenaar, H. Ago, *Nature* **401**, 572 (1999).
- [43] A. Bachtold, C. Strunk, C. Schönenberger, J.-P. Salvetat, L. Forró, in *Electronic Properties of Novel Materials – Progress in Molecular Nanostructures*, eds. H. Kuzmany, J. Fink, M. Mehring, S. Roth, vol. 442, pp. 65–68 (AIP Conference Proceedings, Woodbury, New York, 1998).
- [44] S. Piscanec, M. Lazzeri, J. Robertson, A. C. Ferrari, F. Mauri, *Phys. Rev. B* **75**, 035427 (2007).
- [45] A. Bachtold, C. Strunk, J.-P. Salvetat, J.-M. Bonard, L. Forró, T. Nussbaumer, C. Schönenberger, *Nature* **397**, 673 (1999).
- [46] K. Grove-Rasmussen, H. I. Jørgensen, P. E. Lindelof, *Physica E* **40**, 92 (2007).
- [47] P. Nikolaev, A. Thess, A. G. Rinzler, D. T. Colbert, R. E. Smalley, *Chem. Phys. Lett.* **266**, 422 (1997).
- [48] B. W. Smith, M. Monthieux, D. E. Luzzi, *Nature* **396**, 323 (1998).
- [49] B. W. Smith, D. E. Luzzi, *Chem. Phys. Lett.* **321**, 169 (2000).
- [50] H. Kataura, Y. Maniwa, M. Abe, A. Fujiwara, T. Kodama, K. Kikuchi, H. Imahori, Y. Misaki, S. Suzuki, Y. Achiba, *Appl. Phys. A* **74**, 349 (2002).
- [51] K. Hirahara, K. Suenaga, S. Bandow, H. Kato, T. Okazaki, H. Shinohara, S. Iijima, *Phys. Rev. Lett.* **85**, 5384 (2000).
- [52] D. J. Hornbaker, S.-J. Kahng, S. Misra, B. W. Smith, A. T. Johnson, E. J. Mele, D. E. Luzzi, A. Yazdani, *Science* **295**, 828 (2002).
- [53] C. P. Poole, jr., *Electron Spin Resonance – A Comprehensive Treatise on Experimental Techniques* (Dover Publications, Mineola, New York, 1996), 2nd edn.

- [54] D.-N. Peligrad, B. Nebendahl, C. Kessler, M. Mehring, A. Dulčić, M. Požek, D. Paar, *Phys. Rev. B* **58**, 11652 (1998).
- [55] H. M. Altschuler, in *Handbook of Microwave Measurements*, eds. M. Sucher, J. Fox, vol. 2, p. 530 (Brooklyn Polytechnic Press, New York, 1963).
- [56] M. Martinelly, P. A. Rolla, E. Tombari, *IEEE T. Microw. Theory* **33**, 779 (1985).
- [57] E. H. Grant, R. J. Sheppard, G. P. South, *Dielectric Behaviour of Biological Molecules in Solution* (Clarendon Press, Oxford, 1978).
- [58] M. Sueki, G. A. Rinard, S. S. Eaton, G. R. Eaton, *J. Magn. Res. Ser. A* **118**, 173 (1996).
- [59] A. B. Pippard, *Proc. R. Soc. A* **191**, 370 (1947).
- [60] A. B. Pippard, *Proc. R. Soc. A* **191**, 385 (1947).
- [61] A. B. Pippard, *Proc. R. Soc. A* **191**, 399 (1947).
- [62] E. Maxwell, P. M. Marcus, J. C. Slater, *Phys. Rev.* **76**, 1332 (1949).
- [63] A. B. Pippard, *Proc. R. Soc. A* **203**, 98 (1950).
- [64] J. I. Gittleman, S. Bozowski, B. Rosenblum, *Phys. Rev.* **161**, 398 (1967).
- [65] J. G. Bednorz, K. A. Müller, *Z. Phys. B – Condensed Matter* **64**, 189 (1986).
- [66] S. V. Bhat, P. Ganguly, C. N. R. Rao, *Pramana – J. Phys.* **28**, L425 (1987).
- [67] R. Durný, J. Hautala, S. Ducharme, B. Lee, O. G. Symko, P. C. Taylor, D. J. Zheng, J. A. Xu, *Phys. Rev. B* **36**, 2361 (1987).
- [68] J. Stankowski, P. K. Kahol, N. S. Dalal, J. S. Moodera, *Phys. Rev. B* **36**, 7126 (1987).
- [69] K. W. Blazey, K. A. Müller, J. G. Bednorz, W. Berlinger, G. Amoretti, E. Buluggiu, A. Vera, F. C. Maticotta, *Phys. Rev. B* **36**, 7241 (1987).
- [70] B. F. Kim, J. Bohandy, K. Moorjani, F. J. Adrian, *J. Appl. Phys.* **63**, 2029 (1988).
- [71] P. Bele, H. Brunner, D. Schweitzer, H. J. Keller, *Solid State Commun.* **92**, 189 (1994).
- [72] Q. Li, K. W. Rigby, M. S. Rzchowski, *Phys. Rev. B* **39**, 6607 (1989).
- [73] E. M. Jackson, S. B. Liao, J. Silvis, A. H. Swihart, S. M. Bhagat, R. Crittenden, R. E. Glover III, M. A. Manheimer, *Physica C* **152**, 125 (1988).

-
- [74] K. Kish, A. Rothwarf, S. Tyagi, S. Revenaz, J. Dumas, K. V. Rao, *IEEE T. Magn.* **26**, 1436 (1990).
- [75] K. W. Blazey, in *Earlier and recent aspects of superconductivity*, eds. J. G. Bednorz, K. A. Müller, pp. 262–277 (Springer Verlag, Berlin, 1990).
- [76] P. J. Petersan, S. M. Anlage, *J. Appl. Phys.* **84**, 3392 (1998).
- [77] E. Zavoisky, *J. Phys. USSR* **9**, 211 (1945).
- [78] E. Zavoisky, *J. Phys. USSR* **10**, 197 (1946).
- [79] A. V. Kessenih, *Phys.-Usp.* **50**, 977 (2007).
- [80] M. Planck, *Ann. Phys.* **306**, 69 (1900).
- [81] M. Planck, *Ann. Phys.* **306**, 719 (1900).
- [82] M. Planck, *Verhandlungen der Deutschen Physikalischen Gesellschaft* **2**, 237 (1900).
- [83] M. Planck, *Ann. Phys.* **309**, 553 (1901).
- [84] P. Zeeman, *Nature* **55**, 347 (1897).
- [85] P. Zeeman, *Phil. Mag.* **43**, 226 (1897).
- [86] O. Stern, W. Gerlach, *Z. Phys.* **8**, 110 (1921).
- [87] O. Stern, W. Gerlach, *Z. Phys.* **9**, 349 (1922).
- [88] I. I. Rabi, V. W. Cohen, *Phys. Rev.* **43**, 582 (1933).
- [89] W. Pauli, *Z. Phys.* **31**, 765 (1925).
- [90] G. E. Uhlenbeck, S. Goudsmit, *Naturwissenschaften* **13**, 953 (1925).
- [91] G. E. Uhlenbeck, S. Goudsmit, *Nature* **117**, 264 (1926).
- [92] A. Einstein, *Phys. Z.* **18**, 121 (1917).
- [93] A. Einstein, P. Ehrenfest, *Z. Phys.* **19**, 301 (1923).
- [94] J. M. B. Kellogg, I. I. Rabi, J. R. Zacharias, *Phys. Rev.* **50**, 472 (1936).
- [95] B. Corzilius, *Präparation und EPR-Untersuchung von endohedral paramagnetisch dotierten Fulleren-Peapods $N@C_{60}@SWNT$ und $N@C_{70}@SWNT$* , Diploma thesis, Technische Universität Darmstadt (2005).

- [96] K. Hata, D. N. Futaba, K. Mizuno, T. Namai, M. Yumura, S. Iijima, *Science* **306**, 1362 (2004).
- [97] A. Y. Kasumov, R. Deblock, M. Kociak, B. Reulet, H. Bouchiat, I. I. Khodos, Y. B. Gorbatov, V. T. Volkov, C. Journet, M. Burghard, *Science* **284**, 1508 (1999).
- [98] Z. K. Tang, L. Zhang, N. Wang, X. X. Zhang, G. H. Wen, G. D. Li, J. N. Wang, C. T. Chan, P. Sheng, *Science* **292**, 2462 (2001).
- [99] M. Kociak, A. Y. Kasumov, S. Guéron, B. Reulet, I. I. Khodos, Y. B. Gorbatov, V. T. Volkov, L. Vaccarini, H. Bouchiat, *Phys. Rev. Lett.* **86**, 2416 (2001).
- [100] I. Takesue, J. Haruyama, N. Kobayashi, S. Chiashi, S. Maruyama, T. Sugai, H. Shinohara, *Phys. Rev. Lett.* **96**, 057001 (2006).
- [101] G. M. Zhao, arXiv:cond-mat/0412382v2.
- [102] P. Byszeski, M. Baran, *Europhys. Lett.* **31**, 363 (1995).
- [103] K. Kusakabe, K. Wakabayashi, M. Igami, K. Nakada, M. Fujita, *Mol. Cryst Liq. Cryst.* **305**, 445 (1997).
- [104] A. V. Rode, E. G. Gamaly, A. G. Christy, J. G. Fitz Gerald, S. T. Hyde, R. G. Elliman, B. Luther-Davies, A. I. Veinger, J. Androulakis, J. Giapintzakis, *Phys. Rev. B* **70**, 054407 (2004).
- [105] Y. Ma, P. O. Lehtinen, A. S. Foster, R. M. Nieminen, *New J. Phys.* **6**, 68 (2004).
- [106] R. Moradian, A. Fathalian, *Nanotechnology* **17**, 1835 (2006).
- [107] R. Blinc, P. Cevc, D. Arčon, B. Zalar, A. Zorko, T. Apih, F. Milia, N. R. Madsen, A. G. Christy, A. V. Rode, *Phys. Status Solidi B* **243**, 3069 (2006).
- [108] W. Orellana, P. Fuentealba, *Surf. Sci.* **600**, 4305 (2006).
- [109] S. Okada, K. Nakada, K. Kuwabara, K. Daigoku, T. Kawai, *Phys. Rev. B* **74**, 121412 (2006).
- [110] T. Enoki, Y. Kobayashi, K.-I. Fukui, *Int. Rev. Phys. Chem.* **26**, 609 (2007).
- [111] V. Likodimos, S. Glenis, N. Guskos, C. L. Lin, *Phys. Rev. B* **76**, 075420 (2007).
- [112] N. Murata, J. Haruyama, Y. Ueda, M. Matsudaira, H. Karino, Y. Yagi, E. Einarsson, S. Chiashi, S. Maruyama, T. Sugai, N. Kishi, H. Shinohara, *Phys. Rev. B* **76**, 245424 (2007).
- [113] R. B. Little, *J. Clust. Sci.* **14**, 135 (2003).
- [114] R. B. Little, R. Goddard, *J. Appl. Phys.* **95**, 2702 (2004).

- [115] R. B. Little, A. R. Biris, D. Lupu, Y. Xu, Z. Li, E. Dervishi, A. S. Biris, *J. Magn. Magn. Mater.* **320**, 540 (2008).
- [116] L. Forró, C. Schönenberger, *Top. Appl. Phys.* **80**, 329 (2001).
- [117] P. Petit, E. Jouguelet, J. E. Fischer, A. G. Rinzler, R. E. Smalley, *Phys. Rev. B* **56**, 9275 (1997).
- [118] S. Bandow, S. Asaka, X. Zhao, Y. Ando, *Appl. Phys. A* **67**, 23 (1998).
- [119] A. S. Claye, N. M. Nemes, A. Jánossy, J. E. Fischer, *Phys. Rev. B* **62**, R4845 (2000).
- [120] K. Shen, D. L. Tierney, T. Pietraß, *Phys. Rev. B* **68**, 165418 (2003).
- [121] G. Feher, A. F. Kip, *Phys. Rev.* **98**, 337 (1955).
- [122] F. J. Dyson, *Phys. Rev.* **98**, 349 (1955).
- [123] J.-C. Charlier, T. W. Ebbesen, P. Lambin, *Phys. Rev. B* **53**, 11108 (1996).
- [124] B. Pietzak, M. Waiblinger, T. Almeida Murphy, A. Weidinger, M. Höhne, E. Di-etel, A. Hirsch, *Chem. Phys. Lett.* **279**, 259 (1997).
- [125] B. Pietzak, A. Weidinger, K.-P. Dinse, A. Hirsch, in *Group V Endohedral Fullerenes: N@C₆₀, N@C₇₀, and P@C₆₀*, eds. T. Akasaka, S. Nagase, pp. 13–66 (Kluwer Academic Publishers, Dordrecht, 2002).
- [126] P. Jakes, K.-P. Dinse, C. Meyer, W. Harneit, A. Weidinger, *Phys. Chem. Chem. Phys.* **5**, 4080 (2003).
- [127] M. Yudasaka, K. Ajima, K. Suenaga, T. Ichihashi, A. Hashimoto, S. Iijima, *Chem. Phys. Lett.* **380**, 42 (2003).
- [128] B. Corzilius, K.-P. Dinse, K. Hata, *Phys. Chem. Chem. Phys.* **9**, 6063 (2007).
- [129] R. J. Elliott, *Phys. Rev.* **96**, 266 (1954).
- [130] P. Byszewski, A. Nabilek, *Europhys. Lett.* **34**, 31 (1996).
- [131] G. Wagoner, *Phys. Rev.* **118**, 647 (1960).
- [132] L. S. Singer, G. Wagoner, *J. Chem. Phys.* **37**, 1812 (1962).
- [133] F. Kuemmeth, S. Ilani, D. C. Ralph, P. L. McEuen, *Nature* **452**, 448 (2008).
- [134] V. M. Bermudez, L. M. Ericson, *Langmuir* **22**, 2258 (2006).
- [135] X.-P. Tang, A. Kleinhammes, H. Shimoda, L. Fleming, K. Y. Bennoune, S. Sinha, C. Bower, O. Zhou, Y. Wu, *Science* **288**, 492 (2000).

- [136] A. Kleinhammes, S.-H. Mao, X.-J. Yang, X.-P. Tang, H. Shimoda, J. P. Lu, O. Zhou, Y. Wu, *Phys. Rev. B* **68**, 075418 (2003).
- [137] S. Dag, O. Gülseren, S. Ciraci, *Chem. Phys. Lett.* **380**, 1 (2003).
- [138] J.-P. Salvetat, T. Fehér, C. L'Huillier, F. Beuneu, L. Forró, *Phys. Rev. B* **72**, 075440 (2005).
- [139] B. Náfrádi, N. M. Nemes, T. Fehér, L. Forró, Y. Kim, J. E. Fischer, D. E. Luzzi, F. Simon, H. Kuzmany, *Phys. Status Solidi B* **243**, 3106 (2006).
- [140] S. Agarwal, *EPR investigation of catalyst free single wall carbon nanotubes and endofullerene based peapods*, Master's thesis, IIT Delhi (2007).
- [141] S. Stoll, A. Schweiger, *J. Magn. Res.* **178**, 42 (2006).
- [142] A. Abragam, *The Principles of Nuclear Magnetism* (Oxford University Press, Oxford, 1961).
- [143] D. N. Futaba, K. Hata, T. Namai, T. Yamada, K. Mizuno, Y. Hayamizu, M. Yumura, S. Iijima, *J. Phys. Chem. B* **110**, 8035 (2006).
- [144] E. J. Reijerse, S. A. Dikanov, *J. Chem. Phys.* **95**, 836 (1991).
- [145] S. Stoll, G. Jeschke, M. Willer, A. Schweiger, *J. Magn. Res.* **130**, 86 (1998).
- [146] B. W. Smith, D. E. Luzzi, Y. Achiba, *Chem. Phys. Lett.* **331**, 137 (2000).
- [147] J. Lee, H. Kim, S.-J. Kahng, G. Kim, Y.-W. Son, J. Ihm, H. Kato, Z. W. Wang, T. Okazaki, H. Shinohara, Y. Kuk, *Nature* **415**, 1005 (2002).
- [148] P. Jakes, A. Gembus, K.-P. Dinse, K. Hata, *J. Chem. Phys.* **128**, 052306 (2008).
- [149] F. Simon, H. Kuzmany, B. Náfrádi, T. Fehér, L. Forró, F. Fülöp, A. Jánossy, L. Kórecz, A. Rockenbauer, F. Hauke, A. Hirsch, *Phys. Rev. Lett.* **97**, 136801 (2006).
- [150] N. Weiden, H. Käss, K.-P. Dinse, *J. Phys. Chem. B* **103**, 9826 (1999).
- [151] H. Zhu, G.-L. Zhao, C. Masarapu, D. P. Young, B. Wei, *Appl. Phys. Lett.* **86**, 203107 (2005).
- [152] P. Byszewski, J. Stankowski, Z. Trybuła, W. Kempniński, T. Żuk, *J. Mol. Struct.* **269**, 175 (1992).
- [153] J. Stankowski, L. Piekra-Sady, W. Kempniński, *J. Phys. Chem. Solids* **65**, 321 (2004).
- [154] R. Micnas, J. Ranninger, S. Robaszkiewicz, *Rev. Mod. Phys.* **62**, 113 (1990).

- [155] L. M. Xie, J. Wosik, J. C. Wolfe, *Phys. Rev. B* **54**, 15494 (1996).
- [156] J. Stankowski, B. Czyrak, J. Martinek, *Phys. Rev. B* **42**, 10245 (1990).
- [157] D. H. Cobden, M. Bockrath, P. L. McEuen, A. G. Rinzler, R. E. Smalley, *Phys. Rev. Lett.* **81**, 681 (1998).
- [158] A. A. Odintsov, Y. Tokura, *J. Low Temp. Phys.* **118**, 509 (2000).
- [159] J. Vavro, J. M. Kikkawa, J. E. Fischer, *Phys. Rev. B* **71**, 155410 (2005).
- [160] H. A. Kramers, *Atti del Congresso Internazionale dei Fisici, Como*, vol. 2, p. 545 (1927).
- [161] R. d. L. Kronig, *J. Opt. Soc. Am.* **12**, 547 (1928).
- [162] K. A. Muller, M. Pomerantz, C. M. Knoedler, D. Abraham, *Phys. Rev. Lett.* **45**, 832 (1980).
- [163] Y. Maniwa, A. Grupp, F. Hentsch, M. Mehring, *Physica C* **156**, 755 (1988).
- [164] M. Požek, A. Dulčić, D. Paar, A. Hamzić, M. Basletić, E. Tafra, G. V. M. Williams, S. Krämer, *Phys. Rev. B* **65**, 174514 (2002).
- [165] E. R. Cohen, B. N. Taylor, *J. Phys. Chem. Ref. Data* **2**, 663 (1973).

List of symbols and abbreviations

Roman symbols

1D	one-dimensional
A	hyperfine tensor
\mathbf{a}_i	hexagonal unit vectors
<i>a</i>	magnitude of \mathbf{a}_i ; hyperfine coupling constant
abs.	absolute
AC	alternating current
AFC	automatic frequency control
AIST	National Institute of Advanced Industrial Science and Technology
B	magnetic field vector
<i>B</i>	magnetic field amplitude
B_0	external magnetic field amplitude in <i>z</i> direction
B_1	oscillating magnetic field amplitude orthogonal to external field
$B_{\frac{1}{2}}$	Brillouin function for $J = \frac{1}{2}$
<i>b</i>	saturation field strength constant
BEC	Bose-Einstein condensation
\mathbf{C}_h	chiral vector
<i>C</i>	capacitance
C	coulomb
c. w.	continuous wave
cm	centimeter
CGPM	Conférence Générale des Poids et Mesures (General Conference on Weights and Measures)
CVD	chemical vapor decomposition
D	fine structure tensor
D_{mn}	largest common divisor between <i>m</i> and <i>n</i>
<i>d</i>	distance; diameter; sample thickness

APPENDIX

dB	decibel
dBm	power ratio in decibels (dB) of the measured power referenced to one milliwatt (mW)
DC	direct current
DOS	density of states
DWNT	double-walled carbon nanotubes
E	electric field vector
<i>E</i>	energy; electric field amplitude
<i>E_a</i>	activation energy
<i>E_g</i>	gap energy, band gap
ENDOR	electron nuclear double resonance
EPR	electron paramagnetic resonance
ESE	electron spin echo
ESEEM	electron spin echo envelope modulation
ESR	electron spin resonance
eV	electronvolt
FID	free induction decay
FT	Fourier transformation
FWHM	full width at half maximum
g	<i>g</i> matrix
<i>g</i>	<i>g</i> factor of an electron, Landé factor
<i>g_e</i>	<i>g</i> value of the free electron
<i>g_N</i>	nuclear <i>g</i> value
g	gram
GHz	gigahertz
H	magnetic field strength vector
<i>H</i>	magnetic field strength amplitude
\mathcal{H}	Hamilton operator
<i>h</i>	Planck constant
\hbar	(reduced) Planck constant or Dirac constant
hfi	hyperfine interaction
HPLC	high performance liquid chromatography
HV	high vacuum
HWHM	half width at half maximum

LIST OF SYMBOLS AND ABBREVIATIONS

HYSCORE	hyperfine sublevel correlation experiment
Hz	hertz
I	nuclear spin vector
<i>I</i>	nuclear spin quantum number; intensity
IF	intermediate frequency
IR	infrared
<i>J</i>	total angular momentum quantum number
J	joule
K	kelvin; point in the first Brillouin zone
k , <i>k</i>	wave vector
k_c , <i>k_c</i>	wave vector along the nanotube circumference
k_t , <i>k_t</i>	wave vector along the nanotube axis
<i>k_B</i>	Boltzmann constant
kHz	kilohertz
kOe	kilooersted
kW	kilowatt
<i>L</i>	inductance
<i>l</i>	length
M	magnetization vector
<i>M</i>	magnetization amplitude
M	point in the first Brillouin zone
<i>m</i>	chiral index component
<i>m_I</i>	magnetic nuclear spin quantum number
<i>m_S</i>	magnetic electron spin quantum number
m	meter
MA	microwave absorption
mbar	millibar
meV	millielectronvolt
mg	milligram
MHz	megahertz
min	minute
mm	millimeter
mT	millitesla
ms	millisecond

APPENDIX

mW	milliwatt
MWNT	multi-walled carbon nanotubes
N	spin concentration
n	chiral index component; spin volume density
nm	nanometer
NMR	nuclear magnetic resonance
ns	nanosecond
Oe	oersted
P	power
p. a.	pro analysi (lat.), analytical grade
PEANUT	phase-inverted echo-amplitude detected nutation
PID	proportional-integral-derivative
pm	picometer
ppm	parts per million
ps	picosecond
Q	nuclear quadrupole interaction tensor
Q	quality factor
q	number of hexagons in SWNT unit cell
R	resistance
rf	radio frequency
S	electron spin vector
S	electron spin quantum number
s	second
SI	Système International d'Unités (International System of Units)
SOMO	singly occupied molecular orbital
SQUID	superconducting quantum interference device
SWNT	single-walled carbon nanotubes
T	translational vector
T	temperature; pulse length
T_1	spin-lattice relaxation time
T_2	spin-spin relaxation time
T_c	critical temperature
T_D	transit time
T_m	phase memory time

LIST OF SYMBOLS AND ABBREVIATIONS

T_p	superconducting gap opening temperature
T	tesla
t	SWNT unit cell length
t_1, t_2	evolution time
TE	transversal electric
TEM	transmission electron microscopy
TLL	Tomonaga-Luttinger-Liquid
TWT	traveling wave tube
V	volume
VSWR	voltage standing wave ratio
x	direction in orthogonal space
y	direction in orthogonal space
z	direction in orthogonal space
Z	impedance
°C	degree Celsius

Greek symbols

β	coupling parameter
Γ	center of the first Brillouin zone
γ	gyromagnetic ratio
Δ	difference; superconducting gap energy
δ	skin depth, penetration depth; difference
ε	dielectric constant
ε_0	electric permittivity of free space
η	filling factor
θ	chiral angle
λ	wavelength
μ	magnetic permeability
μ_B	Bohr magneton
μ_N	nuclear magneton
μA	microampere
μs	microsecond

μW	microwatt
ν	frequency
ν_1	nutation frequency or Rabi frequency
ν_L	Larmor frequency
σ	conductivity
τ	pulse separation time
χ	magnetic susceptibility
Ω	ohm
ω	angular frequency
ω_1	angular nutation frequency or Rabi frequency
ω_L	angular Larmor frequency

Symbol indices

AC	alternating current
C	Curie
c	circumference; cavity
diss	dissipated
E	electric
e	empty
eff	effective
EPR	electron paramagnetic resonance
ez	electron Zeeman interaction
f	filled
fs	fine structure interaction
hf	hyperfine interaction
l	loaded
lin	linear
mw	microwave
non-lin	non-linear
nq	nuclear quadrupole interaction
nz	nuclear Zeeman interaction
p	perturbation

r	radiation
rf	radio frequency
s	sample
sat	saturation
stor	stored
sweep	sweep
t	translational
u	unloaded
⊥	perpendicular
∥	parallel

Physical constants

g_e	g value of the free electron	2.0023193134
h	Planck constant	6.626176×10^{-34} J s
\hbar	(reduced) Planck constant or Dirac constant	$1.0545887 \times 10^{-34}$ J s
k_B	Boltzmann constant	1.380662×10^{-23} J K ⁻¹
ϵ_0	electric permittivity of free space	$8.85418782 \times 10^{-12}$ C ² J ⁻¹ m ⁻¹
μ_B	Bohr magneton	9.274078×10^{-24} J T ⁻¹
μ_N	nuclear magneton	$5.0508248 \times 10^{-27}$ J T ⁻¹

All physical constants taken from [165].

Curriculum vitae

Name: Björn Corzilius
Date of birth: July 30, 1979
Place of birth: Dieburg, Germany
Address: Vor dem Obertor 2, 64291 Darmstadt, Germany
Phone: +49 6151 1521420
Email: corzilius@chemie.tu-darmstadt.de

School and scientific career

8/1986 – 7/1990 Friedensschule, Groß-Zimmern
8/1990 – 6/1992 Albert-Schweitzer-Schule, Groß-Zimmern
8/1992 – 7/1996 Goetheschule, Dieburg
9/1996 – 6/1999 Alfred-Delp-Schule, Dieburg; final exam Abitur
10/1999 – 6/2004 Study of chemistry at the Technische Universität Darmstadt (TUD)
7/2004 – 2/2005 Diploma thesis in physical chemistry, title: “Präparation und EPR-Untersuchung von endohedral paramagnetisch dotierten Fulleren-Peapods $N@C_{60}@SWNT$ und $N@C_{70}@SWNT$ ” at TUD under the supervision of Prof. Dr. K.-P. Dinse
2/2005 Diploma graduation, final grade: very good
3/2005 – 4/2008 Doctoral studies at TUD under the supervision of Prof. Dr. K.-P. Dinse, topic: “Electromagnetic properties of single-walled carbon nanotubes investigated by microwave absorption”

Work experience

2005 – 2008 Research associate and teaching assistant at the Eduard-Zintl-Institut für Anorganische und Physikalische Chemie at TUD in the group of Prof. Dr. K.-P. Dinse

Awards

1999 Buchpreis des Fonds der Chemischen Industrie
2002 Dr.-Anton-Keller-Preis
2006 Alarich-Weiss-Preis

Darmstadt, April 2008

List of publications

Reviewed Publications

- J. Dannhäuser, W. Donaubaue, F. Hampel, M. Reiher, B. Le Guennic, B. Corzilius, K.-P. Dinse, and A. Hirsch: σ -donor and π -acceptor stacking interactions in a trans-2-linked C₆₀-cobalt(II) tetraphenylporphyrin diad, *Angew. Chem. Int. Ed.* **45**, 3368–3372 (2006).
- A. Gembus, B. Corzilius, R.-A. Eichel, K.-P. Dinse, S. Immel, D. Stumm, M. Flauaus, and H. Plenio: Electron paramagnetic resonance structure investigation of copper complexation in a hemicarcerand, *J. Phys. Chem. B* **110**, 15012–15020 (2006).
- B. Corzilius, A. Gembus, N. Weiden, and K.-P. Dinse: EPR characterization of catalyst-free SWNT and N@C₆₀-based peapods, *Phys. Status Solidi B* **243**, 3273–3276 (2006).
- B. Corzilius, E. Ramić, and K.-P. Dinse: HYSCORE analysis of nitrogen hyperfine interactions, *Appl. Magn. Reson.* **30**, 499–512 (2006).
- B. Corzilius, K.-P. Dinse, J. van Slageren, and K. Hata: Low-temperature anomaly of microwave absorption and ac susceptibility of single-wall carbon nanotubes: Bulk superconductivity and weak ferromagnetism, *Phys. Rev. B* **75**, 235416 (2007).
- B. Corzilius, K.-P. Dinse, and K. Hata: Single-wall carbon nanotubes and peapods investigated by EPR, *Phys. Chem. Chem. Phys.* **9**, 6063–6072 (2007).
- B. Corzilius, S. Agarwal, K.-P. Dinse, and K. Hata: Electron paramagnetic resonance and non-resonant microwave absorption of single wall carbon nanotubes, *Phys. Status Solidi B* **244**, 3890–3895 (2007).
- B. Corzilius, P. Jakes, N. Weiden, S. Agarwal, and K.-P. Dinse: EPR investigation of N@C₇₀ in polycrystalline C₇₀ and single wall carbon nanotubes, *Mol. Phys.* **105**, 2161–2168 (2007).
- B. Corzilius, K.-P. Dinse, and K. Hata: Probing the electronic properties of single-walled carbon nanotubes with resonant and non-resonant microwave absorption, *Physica E*, in print, DOI: 10.1016/j.physe.2007.09.017 (2008).

Invited Talks

- B. Corzilius and K.-P. Dinse: N@C₆₀ in carbon nanotubes – One-dimensional spin chain or pseudo-liquid?, *Workshop on N@C₆₀-based quantum computing*, Freie Universität Berlin, Berlin, Germany, 2005.
- B. Corzilius, S. Agarwal, K.-P. Dinse, J. van Slageren, and K. Hata: Microwave absorption and weak magnetic ordering in single wall carbon nanotubes – An indication for superconductivity in bulk SWNT, *XXIst International Winterschool on Electronic Properties of Novel Materials*, Kirchberg, Austria, 2007.
- B. Corzilius, S. Agarwal, K.-P. Dinse, J. van Slageren, and K. Hata: Resonant and non resonant microwave absorption as tools for investigating the electronic properties of SWNT and peapods – EPR investigation of N@C₇₀ peapods, *3rd Workshop on Carbon-based Quantum Computing*, Freie Universität Berlin, Berlin, Germany, 2007.
- B. Corzilius, K.-P. Dinse, and K. Hata: Resonant and non resonant microwave absorption of single wall carbon nanotubes, *4th Workshop on Carbon-based Quantum Computing*, Freie Universität Berlin, Berlin, Germany, 2008.

Oral Conference Contributions

- B. Corzilius, R.-A. Eichel, K.-P. Dinse, J. Dannhäuser, and A. Hirsch: Electronic spin properties of a Co(II)-porphyrin-C₆₀-Dyad, *Tag der Fullerene*, Rathen, Germany, 2005.
- B. Corzilius, S. Agarwal, K.-P. Dinse, J. van Slageren, and K. Hata: Probing the electronic properties of SWNT bulk samples by resonant and non-resonant microwave absorption – Evidence for bulk superconductivity and weak ferromagnetism, *E-MRS Spring Meeting, Symposium L: Electron transport in low-dimensional carbon structures*, Strasbourg, France, 2007.

Poster Presentations

- B. Corzilius, A. Gembus, N. Weiden, and K.-P. Dinse: Preparation and pulsed EPR study of N@C₆₀ peapods, *DFG Abschlusskolloquium SPP 1051 (Highfield EPR)*, Hünfeld, Germany, 2005.
- B. Corzilius, A. Gembus, N. Weiden, and K.-P. Dinse: Preparation and EPR characterisation of N@C₆₀ and N@C₇₀ based peapods, *XIXth International Winterschool on Electronic Properties of Novel Materials*, Kirchberg, Austria, 2005.

- B. Corzilius, A. Gembus, N. Weiden, and K.-P. Dinse: Preparation and EPR characterisation of N@C₆₀ and N@C₇₀ based peapods, *EPR Summerschool*, Naurod, Germany, 2005.
- B. Corzilius, A. Gembus, N. Weiden, K.-P. Dinse, and K. Hata: Preparation and EPR characterization of N@C₆₀-based peapods, *XXth International Winterschool on Electronic Properties of Novel Materials*, Kirchberg, Austria, 2006.
- B. Corzilius, K.-P. Dinse, K. Hata, M. Haluska, V. Skakalova, and S. Roth: SWNT probed by multi-frequency EPR and non-resonant microwave absorption, *XXIInd International Winterschool on Electronic Properties of Novel Materials*, Kirchberg, Austria, 2008.

Conference Proceedings

- B. Corzilius, A. Gembus, K.-P. Dinse, F. Simon, and H. Kuzmany: Carbon nanotubes investigated by N@C₆₀ and N@C₇₀ spin probes, in: *Electronic Properties of Novel Nanostructures*, eds. H. Kuzmany, J. Fink, M. Mehring, and S. Roth, AIP Conference Proceedings **786**, Melville, New York, 2005, pp. 291–295.
- B. Corzilius, A. Gembus, N. Weiden, and K.-P. Dinse: Preparation and EPR characterization of N@C₆₀-based peapods, in: *Electronic Properties of Novel Nanostructures*, eds. H. Kuzmany, J. Fink, M. Mehring, and S. Roth, AIP Conference Proceedings **786**, Melville, New York, 2005, pp. 317–320.

Björn Corzilius
Vor dem Obertor 2
64291 Darmstadt

14. April 2008

Eidesstattliche Erklärung

Hiermit erkläre ich an Eides Statt, dass ich meine Dissertation selbständig und nur mit den angegebenen Hilfsmitteln angefertigt habe.

(Björn Corzilius)

Björn Corzilius
Vor dem Obertor 2
64291 Darmstadt

14. April 2008

Erklärung

Ich erkläre hiermit, noch keinen Promotionsversuch unternommen zu haben.

(Björn Corzilius)